2015

Convective Heat Transfer in Quasi-one-dimensional Magnetic Fluid in Horizontal Field and Temperature Gradients

Jun Huang
University of Central Florida

CONVECTIVE HEAT TRANSFER IN QUASI-ONE-DIMENTIONAL MAGNETIC FLUID IN HORIZONTAL FIELD AND TEMPERATURE GRADIENTS

by

JUN HUANG
B.S. Jilin University, 2001
M.S. University of Central Florida, 2010

A dissertation submitted in partial fulfillment of the requirements
for the degree of Doctor of Philosophy
in the Department of Physics
in the College of Sciences
at the University of Central Florida
Orlando, Florida

Fall Term
2015

Major Professor: Weili Luo

ABSTRACT

In this work we studied the convective heat transfer in a magnetic fluid in both zero and applied magnetic fields. The natural convection is observed in a quasi-one dimensional magnetic fluid in a horizontal temperature gradient. The horizontal non-homogeneous magnetic fields were applied across the sample cell either parallel or anti-parallel to the temperature gradient. The temperature profile was measured by eight thermocouples and temperature sensitive paint. The flow velocity field and streamlines were obtained by optical flow method. Calculated Nusselt numbers, Rayleigh number, and Grashof number show that the convective flow is the main heat transfer mechanism in applied fields in our geometry. It was found that when the field gradient is parallel with temperature gradient, the fields enhance the convective heat transfer while the fields inhibit it in anti-parallel configuration by analyzing the temperature difference across the sample, flow patterns, and perturbation Q field in applied fields. Magnetic Rayleigh number and magnetic Grashof number show that the thermomagnetic convections dominate in high magnetic fields. It is shown that the physical nature of the field effect is corresponding to the magnetic body force which is perpendicular to the gravity in our experiments. When the direction of the magnetic body force is same with temperature gradient in parallel configuration, the body force increases the convective heat transfer; while it has opposite effect in anti-parallel configuration.

Our study will not only shed light on the fundamental mechanisms for

thermomagnetic convection but also help to develop the potential field-controlled heat transfer devices.

ACKNOWLEDGMENTS

Firstly, I would like to express my sincere gratitude to my advisor Dr. Weili Luo for the continuous support through my Ph.D study. Her patience and encouragement helped me overcome many crisis situations and finish this dissertation.

Besides my advisor, I specially thank Dr. Tianshu Liu for helpful discussions and insightful comments on temperature sensitive paint related problems in my dissertation. My sincere thanks also goes to all my colleagues in Dr. Luo's research group. I am grateful to Committee members Dr. Enrique Del Barco, Dr. Alain Kassab, and Dr. Alfons Schulte to evaluate my thesis work.

Last but not the least, I would like to thank my family: my parents, my wife and son for supporting me spiritually throughout writing this thesis and my life in general.

TABLE OF CONTENTS

LIST OF FIGURES

LIST OF TABLES

CHAPTER 1: INTRODUCTION

1.1 Natural Convection

Convection is one of the three fundamental heat transfer mechanisms, which are conduction, convection, and radiation. Convection is generally classified into two configurations: forced convection and natural convection. Forced convection is when the flow is forced by an external source, for instance, a fan, a pump, or the wind. Natural convection is also called free convection. It is when the flow occurs "naturally" from the effect of density difference due to the temperature or concentration difference. Natural convection only can happen in a gravitational field. Therefore, natural convection is the study of motion due wholly to buoyancy forces acting on a fluid [1, 2]. The onset of natural convection is determined by the Rayleigh number. The Rayleigh number is a dimensionless number associated with the buoyancy driven flow in the fluid. When the Rayleigh number is less than the critical value for that fluid, the heat transfer is primarily in the form of conduction; and when it is above the critical value, the convection is the main heat transfer mechanism. Natural convection can be widely observed in nature, for example, air flow and ocean flow. There has been growing interest in natural convection over the past couple of decades. One important type of natural convection is the Rayleigh-Benard convection.

1.2 Natural Convection in Magnetic Fluids

Natural convection in magnetic fluids is a new field after the invention of the magnetic fluid. The interaction between fluids and electromagnetic fields has been drawing promising attention, and is starting to have applications in diverse areas. The unique combination of fluidity and the ability of interacting with the magnetic fields is the motivation for the invention of the magnetic fluid. [3, 4]. A magnetic fluid is a dispersed system in which the finely distributed magnetic particles are suspended in a continuous medium. Three components are required in the system: (1) single domain magnetic particles on the nanoscale (3-15nm), so the thermal agitation can keep magnetic particles suspended with Brownian force; (2) the surfactant coating, consisting of an adsorbed long chain molecular species, which is simultaneously compatible with a carrier liquid to prevent the particles from agglomerating; (3) liquid carrier, usually it is water, organic solvent, or metallic solvent (H_g) which depends on its field application.

Magnetic fluids combine the features of magnetism and fluids to display some novel and intriguing behaviors. The particles are ferro- or ferrimagnetic in magnetic fluids, but the behavior of the magnetic fluids is similar to paramagnetism or super paramagnetism at the room temperature. Because the long range interaction between particles for a diluted sample is negligible, the magnetic fluids can obtain a magnetization which is only one order of magnitude less than that of magnetic solids in the same magnetic field.

In magnetic fluids, the most works investigated the Rayleigh-Benard convection

[5-12], which is a type of natural convection. The Rayleigh-Benard convection occurs when a liquid layer is heated from the bottom. This results in a temperature difference ΔT between the top and bottom. In the absence of a magnetic field, if the temperature difference ΔT is not too large, the fluid remains quiescent. However as the temperature difference ΔT is increased, the buoyancy force becomes larger. The hotter portion of the fluid experiences a smaller body force than the colder fluid. The fluid is subject to a tendency to redistribute itself to offset the imbalance. The quiescent state will change once a dimensionless number, Rayleigh number, exceeds a certain critical value.

In 1970, B. A. Flinlayson explained that when a magnetic fluid is heated from below in a vertical uniform magnetic field, the magnetization of the magnetic fluid strongly depends on temperature. Therefore, a nonuniform magnetic body force will change convection in a magnetic fluid due to the temperature gradient [3, 13-15]. In the beginning of the study of natural convection in magnetic fluids, the research was mainly focused on the basic problems of thermo-convective instabilities under the influence of an external uniform magnetic field (a brief review of the results is given in [16] and [17]). Only few studies are dedicated in the heat transfer in the presence of a non-homogeneous external field. The investigations of convection in magnetic fluids proved the general similarity between the gravity convection and the thermomagnetic convection.

For the natural convection with horizontal temperature different, the experiment with a paramagnetic fluid in a vertical non-uniform magnetic field showed the field effect is

similar to normal buoyancy. [18]. A series of experiments in thin vertical magnetic fluid layers in transverse uniform magnetic field showed the magnetocovection dominated in this geometry, so the convection patterns in fields were different from that in zero field.[19-21]

Studies on magnetic fluids have shown that the strong horizontal magnetic fields can be used to induce magnetic Benard convection in normal paramagnetic fluids. The magnetic field can enhance or suppress buoyancy-driven convection in a solution of gadolinium nitrate, the sign of the effect depending on the relative orientation of magnetic-field and temperature gradients [22].

1.3 Applications of Magnetic Fluids

The properties of magnetic fluids and the possibility of magnetically controlled flow have led to wide applications in various fields, including mechanical engineering, biomedical engineering and other more extensive fields.

For mechanical applications, the most widely used application is the sealing of rotary shafts [4, 23 and 24]. Magnetic fluids can be used as lubricants to be hold constant position in a friction zone by applied magnetic fields. Magnetic fluids are also used in the manufacture of supports, bearings, dampers and shock absorbers. Non-magnetic bodies submerged in a magnetic field experience a different floating force which depends on its density in a non-uniform magnetic field, so magnetic fluids can be used to separate ores [25]. In medical applications, magnetic drug targeting is the use of biocompatible magnetic fluids

as a delivery system in locoregional tumor therapy to enrich magnetic particles in a desired body compartment [26]. Magnetic fluids can also be used as a contrast medium in x-ray examinations [27], blocking the blood flow in macrovessels during operations, and tracing blood flow in non-invasive circulatory measurement.

For applications with thermal convection, the effect of a magnetic field on a magnetic fluid changes the structure of its flow. Magnetic fluid was used to measure bubble velocity [28] and void fraction in gas-liquid two phase flow [29]. Magnetic fluid was used to increase heat pipe efficiency by putting permanent magnets close to the warm end [30 and 31]. Magnetic fluid can be used as coolant in electronic equipment. The major application is cooling of loudspeakers which significantly increase maximum acoustical power without changing any structure of speaker system [32]. The magnetic wheel-type refrigerator is also another application [33].

The effect of magnetic field on natural convection in our experiment suggests potential applications to control the convective heat transfer in fluids. The magnetic field can enhance or suppress the convective heat transfer. The magnetic field has been used to suppress the convection in non-magnetic fluids such as liquid metals [34] and crystal growth [35] to improve the quality of crystal. It requires very high magnetic field (10 Tesla) in these non-magnetic systems. The degree of the magnetization can be achieved in magnetic fluid is many orders of magnitude higher than that in non-magnetic fluids, so we can study much noticeable field effect on convective heat transfer with only hundreds of Gauss. Our study

also can be applied to auto cool high power electric devices such as transformer [36]. The field control flow effect is very useful in low gravity conditions, for example orbital stations, where cooling by natural gravitational convection cannot be realized [37-39]

When the mechanism of the magnetic field effect in convective flow is fully understood, we will be able to non-intrusively increase the cooling or heating efficiency for heated devices with magnetic fields. Many other applications will be explored in the future as well.

CHAPTER 2: SAMPLE CELL DESIGN, EXPERIMENT SETUP, AND MATERIAL PROPERTIES OF SAMPLES

2.1 Design principle

The experiment is designed to study the relative orientation of field gradient to that of temperature gradient on natural convection horizontally. Figure 2.1 shows the principle of experiment. It includes the magnetic field and the sample cells. Parts 1 are the two poles of an electromagnet. The magnetic field between the two poles is non-uniform. The magnetic field is symmetric along the center. The field strength can be adjusted by changing the electric current through electromagnet.

Two identical horizontal quasi-one dimension cells (part 2) filled with the magnetic fluids are placed on the axis of the magnetic field. The horizontal thermal gradient is induced by heating on the left side of a sample cell with electrical heater and cooling on the right side with circling cooling fluid at the same time. The direction of thermal gradient is from right to left. Natural convection happens in the sample cells when the thermal gradient is applied. The only difference between the two sample cells is the relative direction of the magnetic field gradient and thermal gradient when we apply the fields. On the left cell, the magnetic field gradient is parallel with the thermal gradient, and on the right cell, the magnetic field gradient is anti-parallel with the thermal gradient. This allows the parallel and anti-parallel configurations to be observed and measured at the same time. Thermocouples are used to

measure the temperature on the selective positions inside the fluids. Temperature sensitive paint (TSP) is painted on the front surface of the cells to image temperature profile in order to obtain the velocity and flow pattern.

In this work we focus our study on the natural convection in horizontal magnetic fluid cells where the temperature and field gradients and applied field are perpendicular to the gravity, a configuration differ from the ordinary magnetic Rayleigh-Bernard Convection, in which the temperature gradient is vertical [11, 12 and 40]. In this configuration, the convective flow occurs in both zero and applied field due to buoyancy force originates from gravity. However the magnetic force in the fluid from applied field and field gradient will not interact with gravitational force along the vertical direction. The field effect depends on the relative orientation of temperature gradient and field gradient.

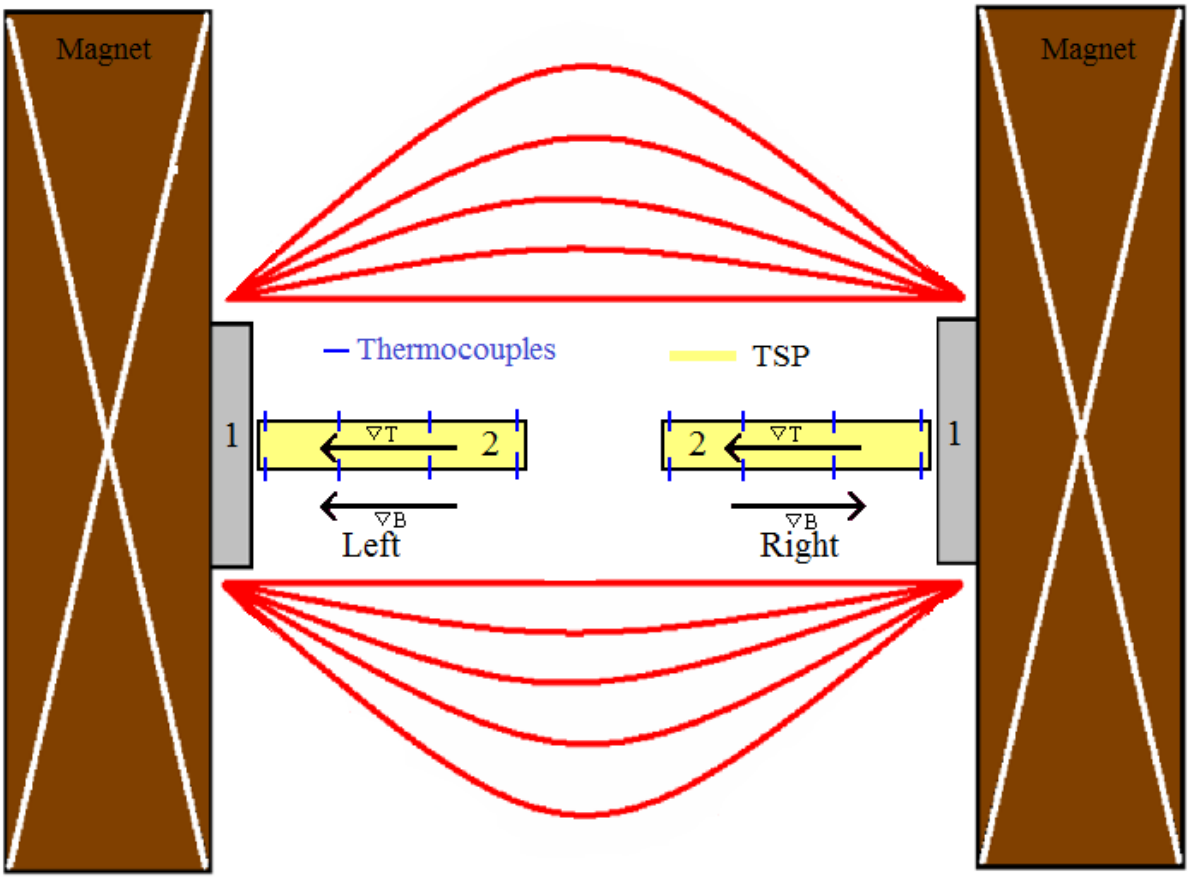

Figure 2.1. Principle of experiment

2.2 Physical system and material properties

Physical system used in our experiments is magnetic fluid. A magnetic fluid is a fluid consisting of magnetic nanoparticles (Fe3O4) suspended in nonmagnetic solvent. The schematic of a magnetic fluid is showed on figure 2.2. Magnetic fluid can interact with a magnetic field.

In the magnetic fluid used in the experiment, the mean diameter of the particles is 10 nm, the magnetic moment of each particle is 21000 Bohr magnetons, and each particle is coated with a 2 nm nonmagnetic surfactant layer (Oleic acid) to prevent agglomeration. The volume fraction is 1%. The Ferrotec magnetic fluid sample we used is EMG905, the properties of EMG 905 are showed in table 2.1.

Table 2.1. Properties of magnetic fluid sample (Ferrotec EMG 905)

Saturation magnetization	Viscosity @27^{o}C	Volatility @50^{o}C	initial susceptibility	Density g/(cm^{3})	Volume % particle Concentration	flash point	pour point
440 G	9 cp	9%1hr	1.9	1.24	7.9	89^{o}C	-94^{o}C

The solvent of the magnetic fluid is kerosene. The thermal properties of kerosene and diluted sample are showed in table 2.2 and 2.3[4].

Table 2.2. Thermal properties of kerosene

T(^{o}C)	Density g/(cm^3)	specific heat kJ/(kg.K)	Viscosity 10^6 Pa.s	thermal conductivity W/(m.K)	thermal expansion K^{-1}	surface tension 10^3 N/m
20	0.77	1.98	8290	0.13	10.65	N/A

Table 2.3. Thermal properties of magnetic fluid (diluted at 1% volume fraction)

T(^{o}C)	Density g/(cm^3)	specific heat kJ/(kg.K)	Viscosity 10^6 Pa.s	thermal conductivity W/(m.K)	thermal expansion K^{-1}	surface tension 10^3 N/m
20	0.87	1.84	8497	0.15	8.6	28

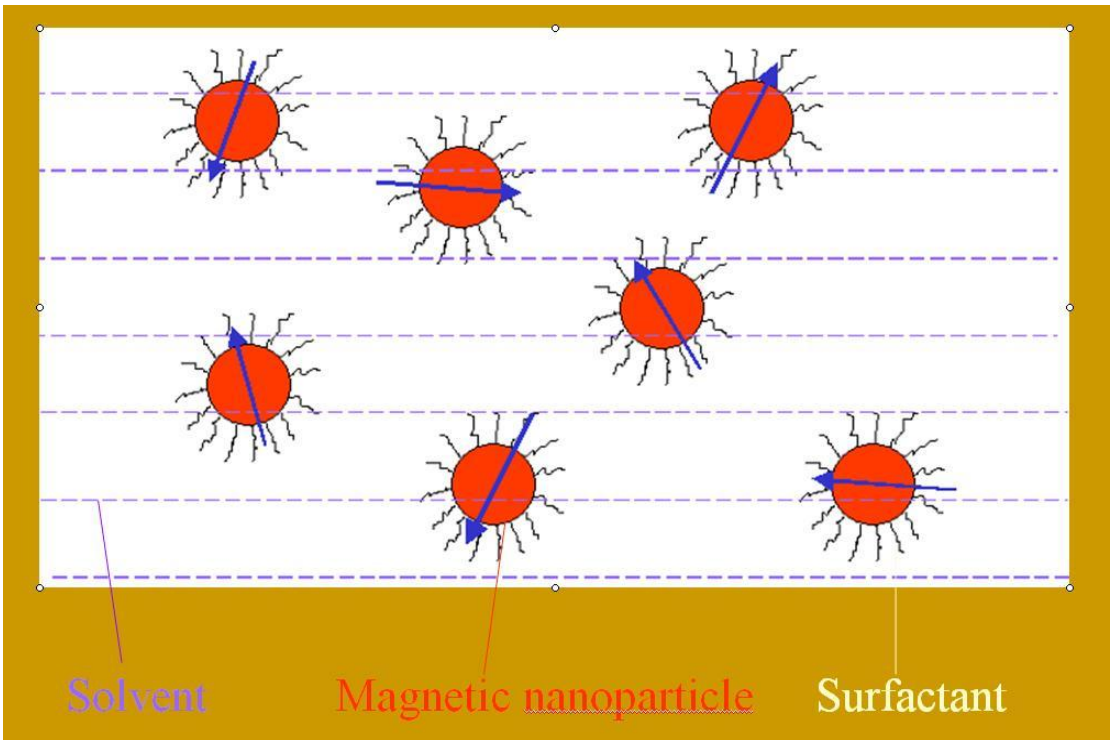

Figure 2.2. Schematic of a magnetic fluid

2.3 Experiment setup and flow chart of procedure

The experiment is designed to study field effect in two configurations. Figure 2.3 shows the experimental setup. The numeric numbers represent:

1) 1a (left cell) and 1b (right cell) are the sample cells filled with kerosene fluid or magnetic fluid. The length of the sample cell is 9.0 cm, the width is 0.6 cm and height is 0.75 cm.

2) There are eight thermocouples (four on the top and four on the bottom) inside each cell to measure temperatures inside fluid without disturbing the flow much. There are also two other thermocouples on magnet and two in the air to measure the background temperature. Thermocouples are OMEGA, K type, precision fine wire thermocouples. The wire diameter is 0.25mm [41].

3) A multimeter (Keithley 2701) was used to gather the data from the thermocouples. The temperature was read by a computer every two second [42].

4) The electric heater heats the sample on the left side. The heating power 0.545 W is controlled by the current of a power supply. The heater is a Minco HK5572 [43]. This heater is a polyimide heater with a dimension of 12.7 mm by 12.7 mm. The resistance of heater is 26.5 ohms. Effective area is 1.23 $cm^{2.}$ The power supply for the heater is HP6267B.

5) The cooling pump is connected to the cell on the right side to cool the sample with circulating cooling fluid by Polyscience digital controller (model number 9102) [44]. Cooling Power is 0.408 W. The temperature in the tank is set at -17 ℃. The cooling rate can be

controlled by adjusting the pump speed. The flow rate of cooling fluid is measured to be 13.8 ml/s.

6) The magnetic fields are controlled by a separate power supply, and field gradient is applied horizontally across the sample cells. In our experiments, only the magnetic field and field gradient are changed. The heating and cooling rate are fixed.

Figure 2.4 shows the external magnetic field distribution on the axis. A gauss meter was used to measure the magnetic field. The x axis shows the distance to the left pole. The distance between the two poles is 34.8 cm. The magnetic field is symmetric along the center. On the left side(x from 0-17.4 cm), the magnetic gradient is from right to left, while on right side (x from 17.4-34.8 cm), the magnetic gradient is from left to right. In the experiments, the sample cells are placed on the axis of the magnetic field. The area of the cross section of the sample cells is 0.45 cm^2, which is much smaller than the area of the magnet poles (78.5 cm^2).

The difference between the two sample cells (1a and 1b) is the relative orientation of the magnetic field gradient and temperature gradient when the fields are applied. On the left cell (1a), the magnetic field gradient is parallel with the thermal gradient, and on the right cell (1b), the magnetic field gradient is anti-parallel with the thermal gradient.

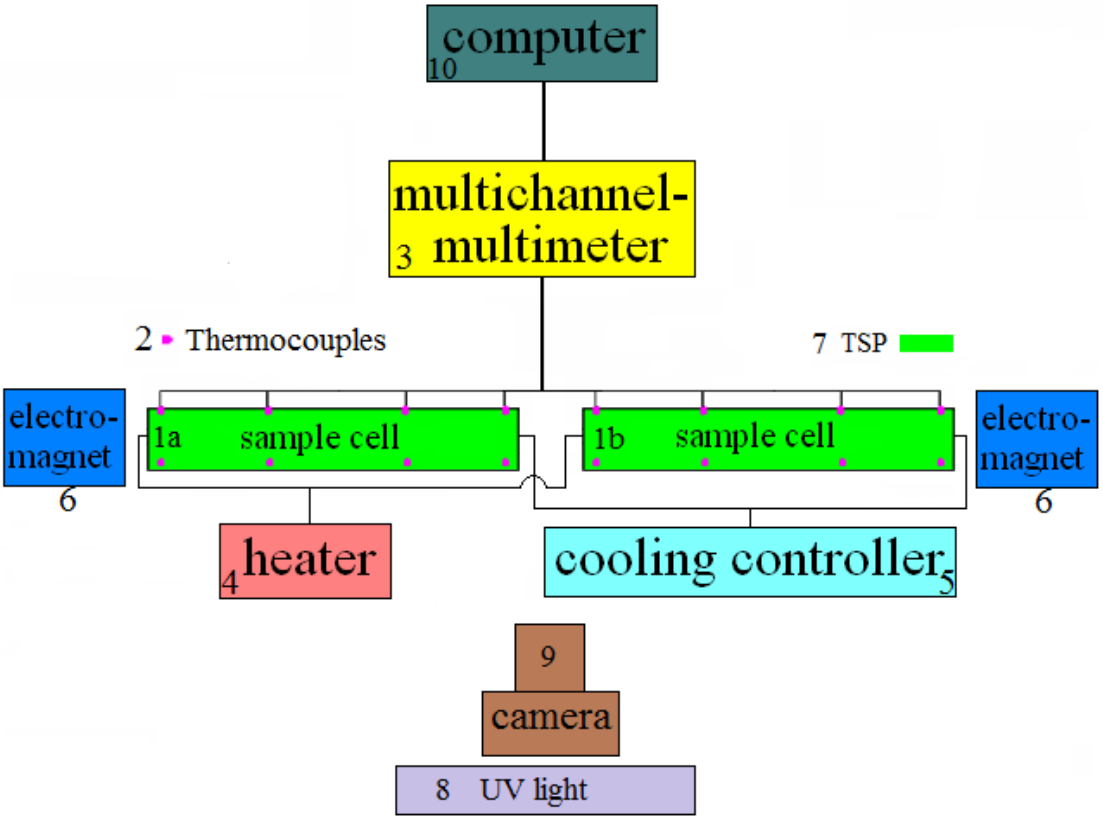

Figure 2.3. Experimental setup

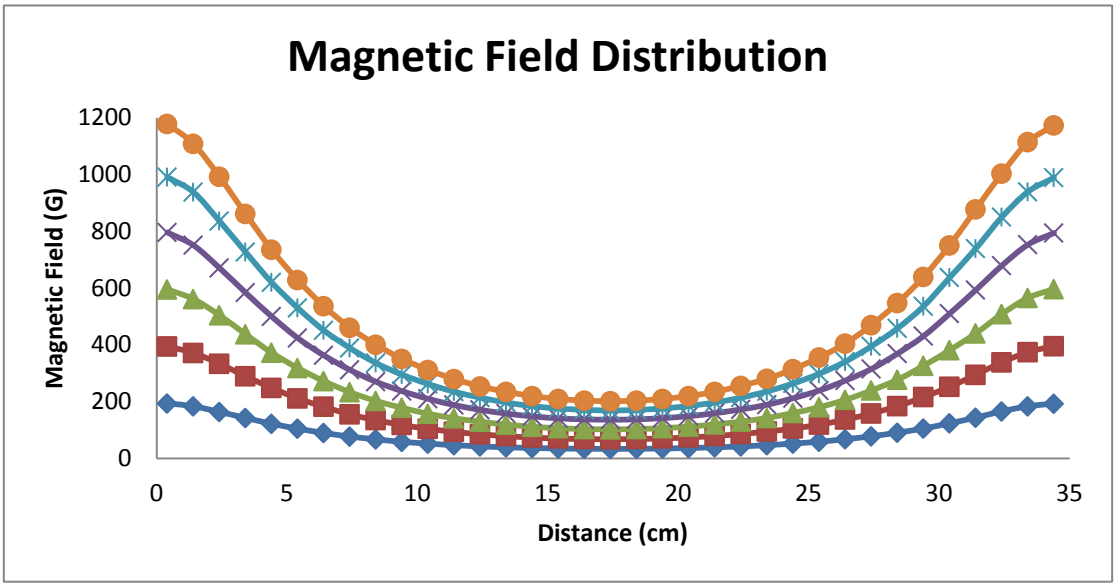

Figure 2.4. External magnetic field distributions

7) Temperature sensitive paint (TSP) is painted on the front surface of the sample cells to image the temperature profile on the surface in order to extract flow velocity and flow pattern. The details of the principle and set up of TSP are in chapter 2.6. Thermocouple measures the temperature inside the fluid directly. But the number of thermocouples is limited to avoid disturb the flow, here only eighty point temperatures can be recorded with the thermocouples. TSP can measure the local surface temperature in detail without flow intrusion.

Table 2.4. Temperature sensitive paint properties

Luminophore	Binder	Excitation wavelength(nm)	Emission wavelength(nm)	Useful temperature range (^{o}C)	Max. log slope (%/^{o}C)	Lifetime at room temp. (μs)
EuTTA	Dope	350	612	-20-80	-3.9	500

The recipe of the TSP formulation in our experiment is EuTTA in Dope [45]. EuTTA is luminophore powder. It is Europium (III) thenoyltrifluoroacetonate, trihydrate, 35% from Acros Organics. The dope is clear supercoat butyrate dope with dope thinner from Sig Mfg. The properties of the TSP are shown in table 2.4. The procedure to prepare TSP is mixing 6 mg EuTTA with 10 ml of the dope thinner in a sealable container, shaking it well and then sonicating for 5 minutes. Then 10 ml of dope is added, shake and sonicate for another 5 minutes. Using a commercial paint brush brush a thin layer of TSP to the clean surface.

Multiple TSP layers can be applied to optimal emission light intensity. The paint is allowed to cure until the thinner completely evaporated. Acetone is used as a solvent to clean up the paint if necessary.

8) The Ultra-Violet light is used as excitation light source of TSP. The model of UV light is GE black light F20T12. The power of light is 25w. The spectrum of UV light is shown in figure 2.5. The peak wavelength is 375nm. The light intensity stability is 1% after 5 minutes warm up.

9) To ensure the low noise-to-signal ratio and high sensitivity to emission light from paint, a CCD (Charge-Coupled Device) camera is used for TSP measurement. The excited fluorescent light is filtered by a long-pass optical filter to eliminate the illuminating light before it projects onto the CCD camera. The optical filter is Edmund 550nm long-pass filter. The filter only transmits the light with wavelength $\lambda \geq 550$ nm. The camera is Prosilica GC1020. It has a high intensity resolution (12 bits) and high spatial resolution (1024 × 768 pixels). The maximum frame rate is 33 frames per second. The frame rate in our experiments is 10 fps. The captured images are transferred via Ethernet cable to a computer for image processing. The image acquisition process is controlled by a Labview program.

Figure 2.6 shows the experimental procedure in step fields. The horizontal heating and cooling are switched on at beginning. The temperature of the magnetic fluid inside sample cells starts to change. After 2000 seconds, when the temperature distribution in fluid reaches steady state. The first step magnetic field B_{max}=100G is induced. B_{max} is the field at

the pole of the magnet. The field is increased by 100G in step at the interval of 200s up to B_{max}=1000G. At t=4000s, all field, heating and cooling are turned off. The temperature of system is allowed to relax back to room temperature after that.

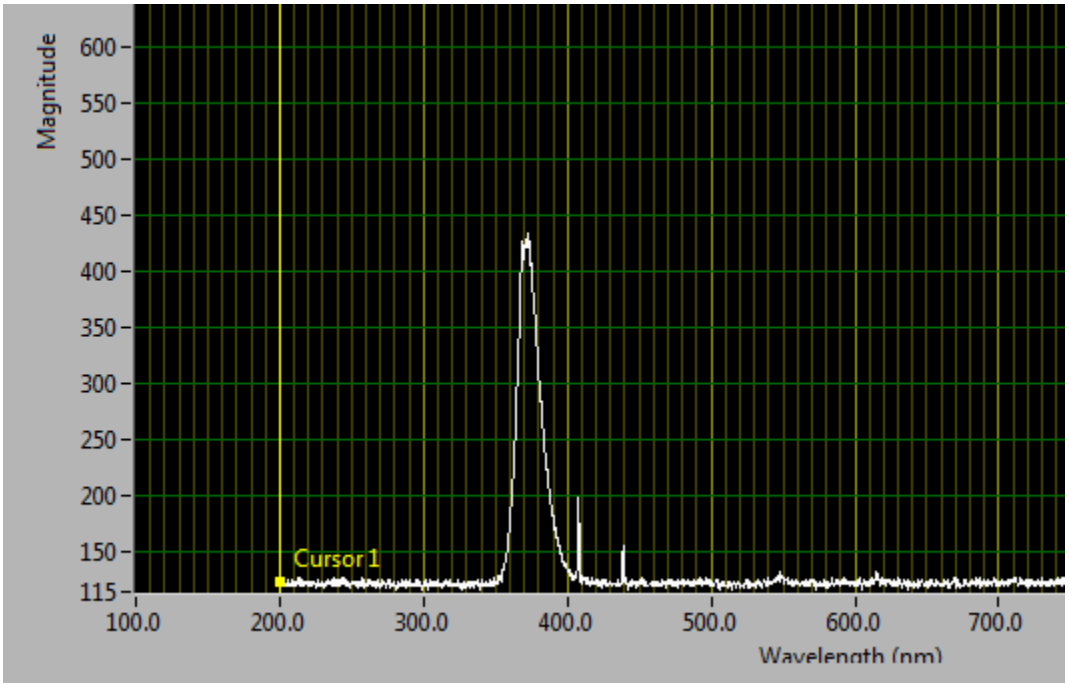

Figure 2.5. The spectrum of UV light

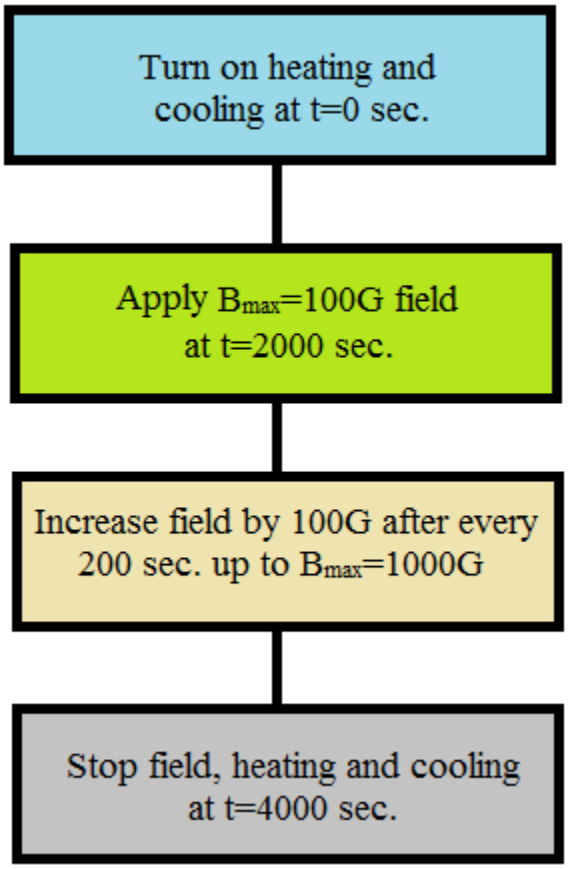

Figure 2.6. Flow chart of experimental procedure in step fields

2.4 Sample cell design

The sample cell is designed for quasi-one dimensional horizontal heat transfer. The parts of a sample cell are depicted in Figure 2.7. Part (a) is the body of the cell made of Lexan, which has a chamber to hold the magnetic fluid. Lexan was chosen as container because 1) Lexan has a small thermal conductivity (0.2 w/m*C); 2) Lexan is transparent, allowing for easy observation of the magnetic fluid inside. The top of the cell is sealed with another piece of Lexan plate. Four thermocouples are coming out from top and bottom plate respectively. On the two ends, there are aluminum blocks (part b) that act as uniform heating and cooling sources due to aluminum's high thermal conductivity (237 w/m*C). The aluminum blocks have small tongues inserted into the Lexan chamber to make contact with the magnetic fluid. The left block is heated by an electric heater, and the circulating cooling fluid goes through right block to cool it. The length of the cell is 9 cm, width is 0.6 cm and height is 0.75 cm. The ratio of length over width is 16.7, so they can be treated as quasi-one dimensional sample cells.

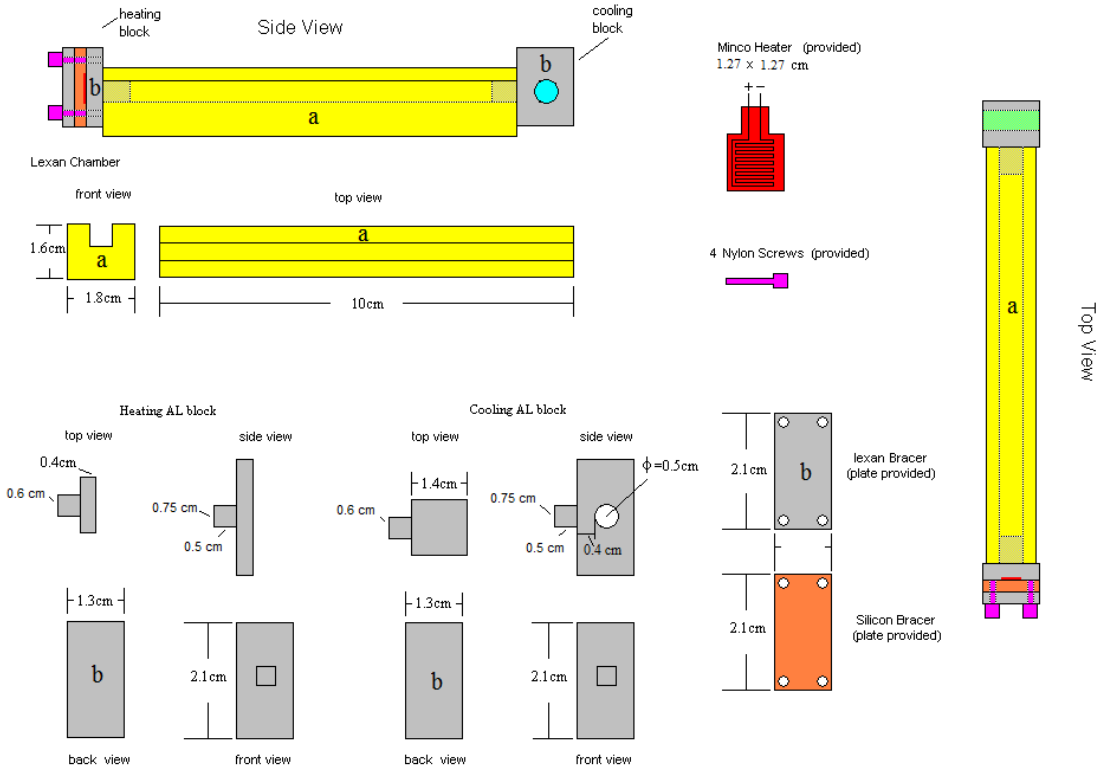

Figure 2.7. The design of sample cell

2.5 Particle tracking velocimetry and optical flow method

The microspheres in base fluid (kerosene) are used to get the flow velocity and pattern in zero field with same volume fraction as the magnetic fluid to establish the base velocity and pattern. This method is called particle tracking velocimetry (PTV). PTV is a widely used technique based on local spacial correlation between two consecutive tracking particle pictures for global measuration of the velocity fields to identify the correspondence between individual particles at successive instants when the particle volume fraction is sufficiently low (Maas, Dracos & Gruen 1998; Gruen & Papantoniou 1993). Microspheres are the tracking particles used in our experiment. Microspheres are small spherical particles, with diameters in the micrometer range. To visualize the flow in kerosene, the microspheres need to suspend in kerosene. The density of microspheres needs to match the density of the kerosene (0.7-0.8g/cc). When the heating and cooling is applied, the convective flow starts due to the buoyancy. The microspheres move with the fluid. The high resolution CCD camera is used to capture the movement of the particles. From the movement of the particles we can get the flow velocity and flow pattern in kerosene by using optical flow method. The microsphere (Cenosphere grade 500) used in our experiment is from Diversified Cementing Products. The density distribution of the microspheres is from 0.78 to 0.95 g/cc. The average size is 180 microns. To density match with kerosene, we put microspheres into the kerosene first. All the microspheres that suspend in kerosene have the same density as the kerosene. The suspended microspheres are selected for flow visualization in kerosene. Figure 2.8 shows

the microspheres suspended in kerosene in an experiment.

The optical flow method is used to analyze the fluids motion from the microspheres and TSP images. The optical flow is defined as the velocity field in the image plane that transforms one image into the next image in a time sequence. The optical flow methods are the analysis of sequence of images to approximate motion. It is to compute an approximation 2-D motion from a projection of 2-D or 3-D velocities of the object. It is the spatiotemporal patterns of image intensity (Horn 1986, Verri and Poggio 1987). This approximation is called the optical flow field (see figure 2.9). It corresponds to the actual object movement and the movement of pixels in the picture.

As long as the optical flow field provides a reasonable approximation though, the measurements of image velocity can be used in a wide variety of tasks, including time-to-collision calculations, structure of the objects, movement parameters, and segmentation, among many others.

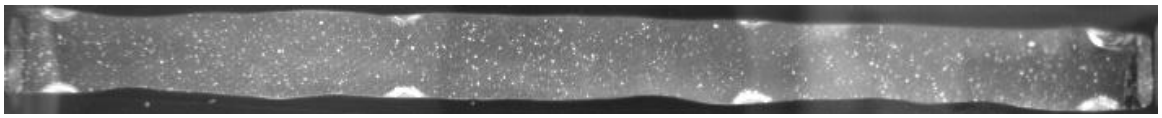

Figure 2.8. Microspheres in kerosene

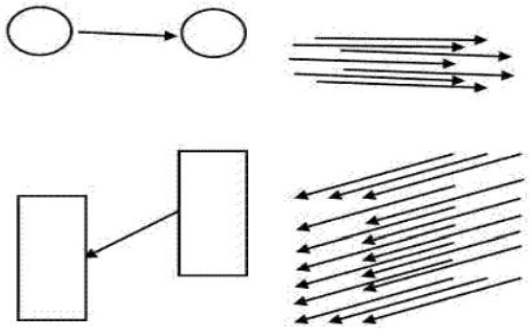

Figure 2.9. The movement of two objects over two frames on the left, the corresponding optical flow vectors on the right.

2.6 Temperature sensitive paint (TSP)

Temperature sensitive paint is a new optical technique developed since 1980s. It is based on the mechanism of luminescent thermal quenching that the luminescent intensity decreases as temperature increases [45]. A relationship between luminescent intensity and the absolute temperature can be described through Arrhenius form.

$$\ln \frac{I(T)}{I(\mathrm{Tr})} = \frac{Er}{R}\left(\frac{1}{T} - \frac{1}{Tr}\right) \tag{2.1}$$

Where E_r is the activation energy, R is the universal gas constant. T is a measuring temperature in Kelvin and T_r is a reference temperature, usually referring to room temperature.

Temperature sensitive paint (TSP) is a non-intrusive method and full-field measurement of surface temperature with high resolution and low cost. TSP is a polymer-based paint composed of temperature sensitive luminescent molecules that act as probes and polymer binder. The polymer binder and luminophore can be dissolved in a solvent like paint thinner. The resultant paint can be applied to a surface by using a brush or sprayer. The solvent will evaporate and the luminescent molecules are immobilized in a solid polymer coating on the surface. When a light source with corresponding wavelength of luminophore illuminates the TSP, the molecules are excited and emit a longer wavelength fluorescent light. Figure 2.10 shows a schematic of a TSP emitting luminescent light under an ultraviolet light excitation. The emitting light is captured by a high resolution CCD camera through an optical filter. After an appropriate calibration, temperature can be remotely

measured by detecting the emitting fluorescent light.

Compared to conventional temperature sensors like thermocouples, TSP has many advantages, such as a non-intrusive technique, a global distribution of the surface temperature measurement and high spatial resolution with reasonable accuracy. So far a family of TSPs can cover a temperature range of –196 ^{o}C to 200 ^{o}C. The accuracy of a TSP is typically from 0.2 ^{o}C to 0.8 ^{o}C. TSP has been used in various experiments to measure the temperature and heat transfer distributions, flow separation and boundary layer transition.

In order to quantitatively measure the temperature with TSP, the relationship between the luminescent intensity and temperature should be experimentally determined by calibration based on the temperature range in our experiments. A TSP coating is applied to the top surface of an aluminum block. The temperature of the aluminum block is controlled by adjusting the temperature in circulating fluid tank over a range of -13℃ to 80℃. Five fine gauge K-type thermocouples are embedded in the aluminum block. A uniform temperature distribution in aluminum block was created due to the high thermal conductivity of the aluminum. The temperature difference between the thermocouples is less than 0.05 ℃. The calibration setup is showed in figure 2.11.

EuTTA-dope TSP is used in the calibration and experiment. The calibration result of the typical temperature dependencies of the paint are shown in figure 2.12. Normalized temperature is defined as temperature ratio T/Tr and is plot against intensity ratio I/Ir. T is the measuring temperature and Tr is the reference temperature. I is the intensity corresponding to

the measuring temperature and Ir is the intensity at reference temperature. The calibrations have been performed between -13 ℃ and 80 ^{o}C. The reference temperature of 21.9 ℃ is selected for all the calibrations that have been carried out. The standard error of fit *S* is found to be 0.006 from the equation 2.2 [46]

$$s = \sqrt{\left(\frac{\sum\left(y_{data}-y_{fit}\right)^{2}}{N-m}\right)} \tag{2.2}$$

Precision interval = $\pm t_{v,p}S$. N=20 is the number of measurements, m=3 is the number of fitted coefficients. *v*=N-1=19, *p*=95% is level of confidence. From Table 4.4 of the reference [46] $t_{19,95}$ is 2.093. So that the precision interval is found to be ±1.2 ℃ with 95% level of confidence.

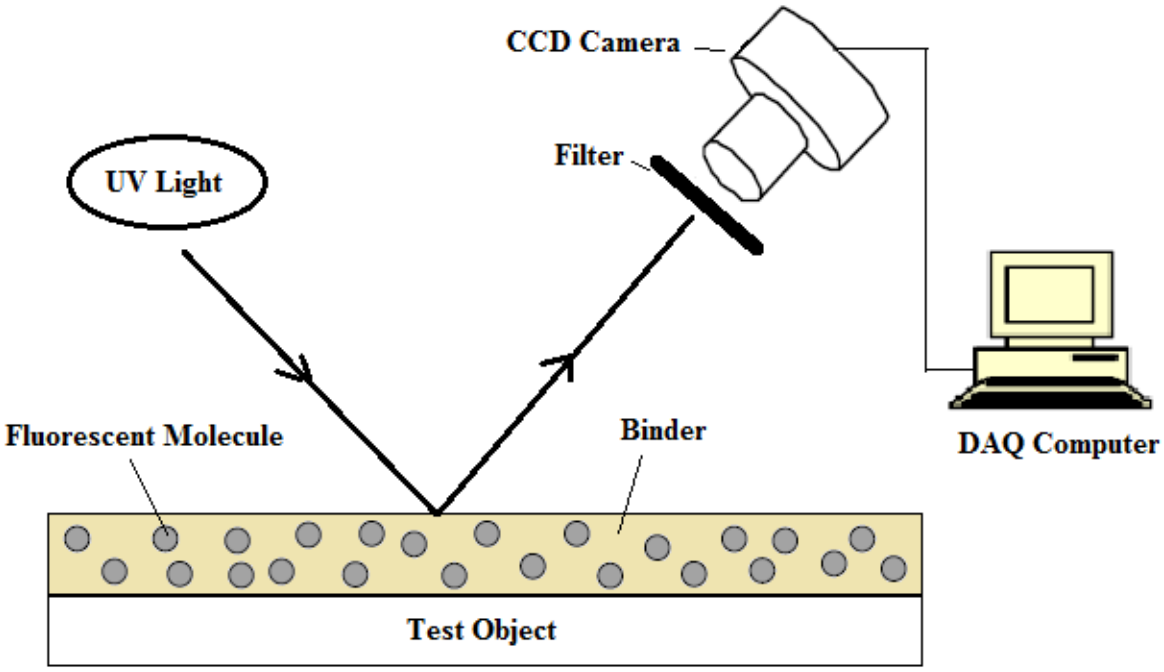

Figure 2.10. Schematic of a temperature sensitive paint on a surface

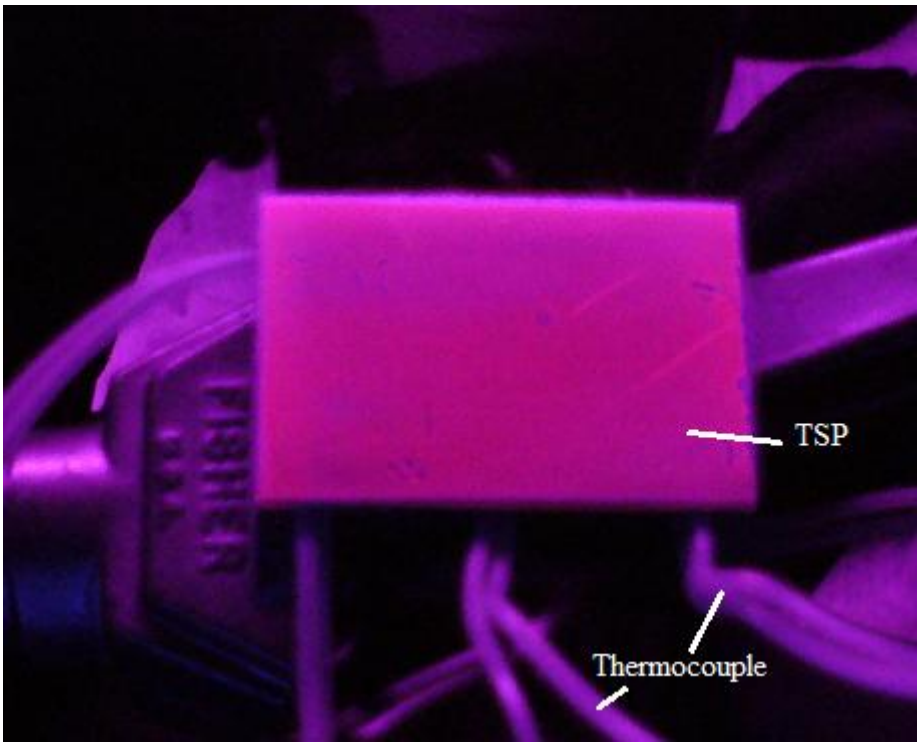

Figure 2.11. Experimental setup for calibration of TSP

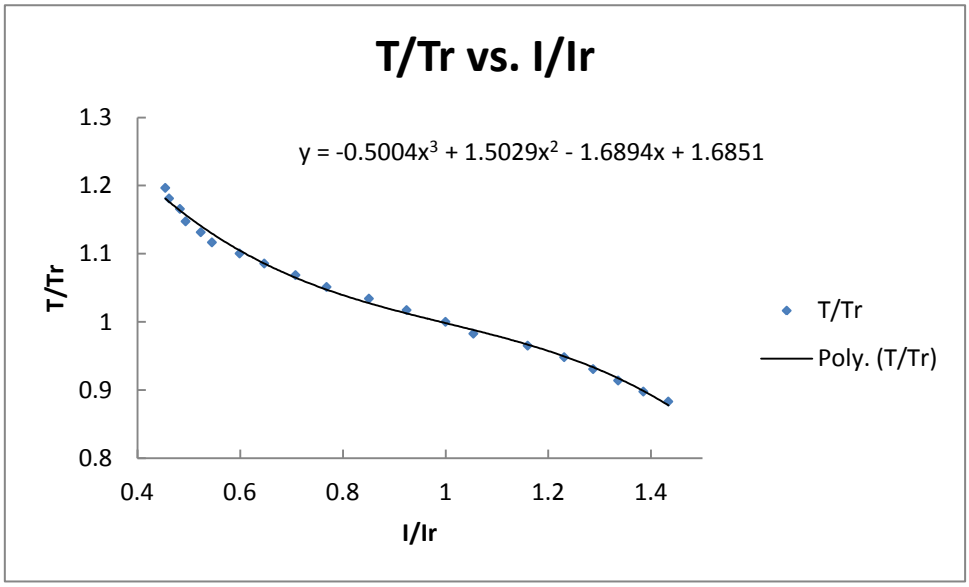

Figure 2.12. Normalized temperature vs. intensity calibration curve

2.7 Vacuum chamber design

The vacuum chamber is designed to minimize the heat dissipation during the experiment, also it offers the better signal to noise ratio from temperature sensitive paint. The sample cell is placed in vacuum chamber during the experiment. Figure 2.13 shows the design of vacuum chamber. Figure 2.14 is the vacuum chamber setup with a sample cell inside.

The vacuum chamber is made with UV transmitting Acrylic to allow UV light to go through chamber walls to excite the TSP. The thickness of the Acrylic is 1 cm. The medium vacuum ($3x10^{3}$ to $1x10^{-1}$ Pa) can be maintained in the chamber. The front wall can be detached and resealed by silicone. A long-pass optical filter is on the front to filter the short wavelength emitting light from TSP and light source. The cooling fluid inlet is at the right side wall and outlet is on the back. All heating wires and thermocouples are through the back wall to connect to the corresponding instruments. The vacuum pump connects chamber at top outlet. The vacuum pump is Trivac D4B. After 10 minutes pumping, the pressure in chamber reaches and holds 0.9 inches of mercury, which is $3.0*10^{3}$ Pa.

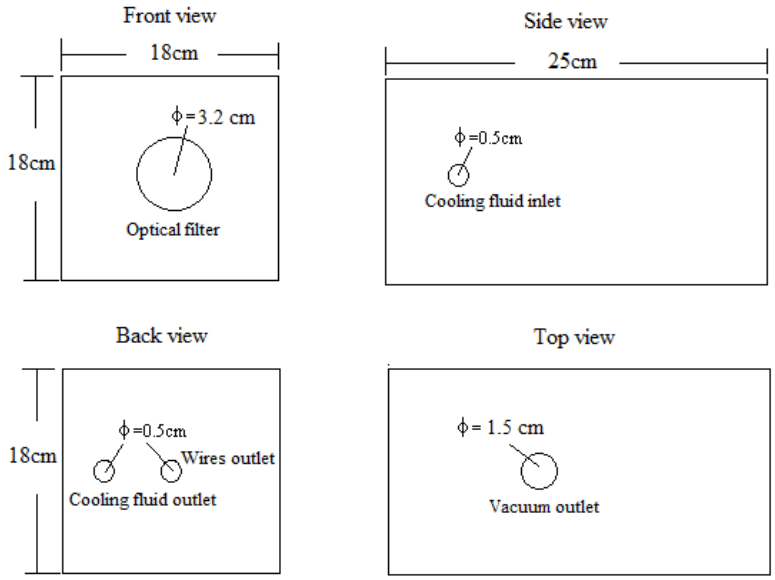

Figure 2.13. The design of vacuum chamber

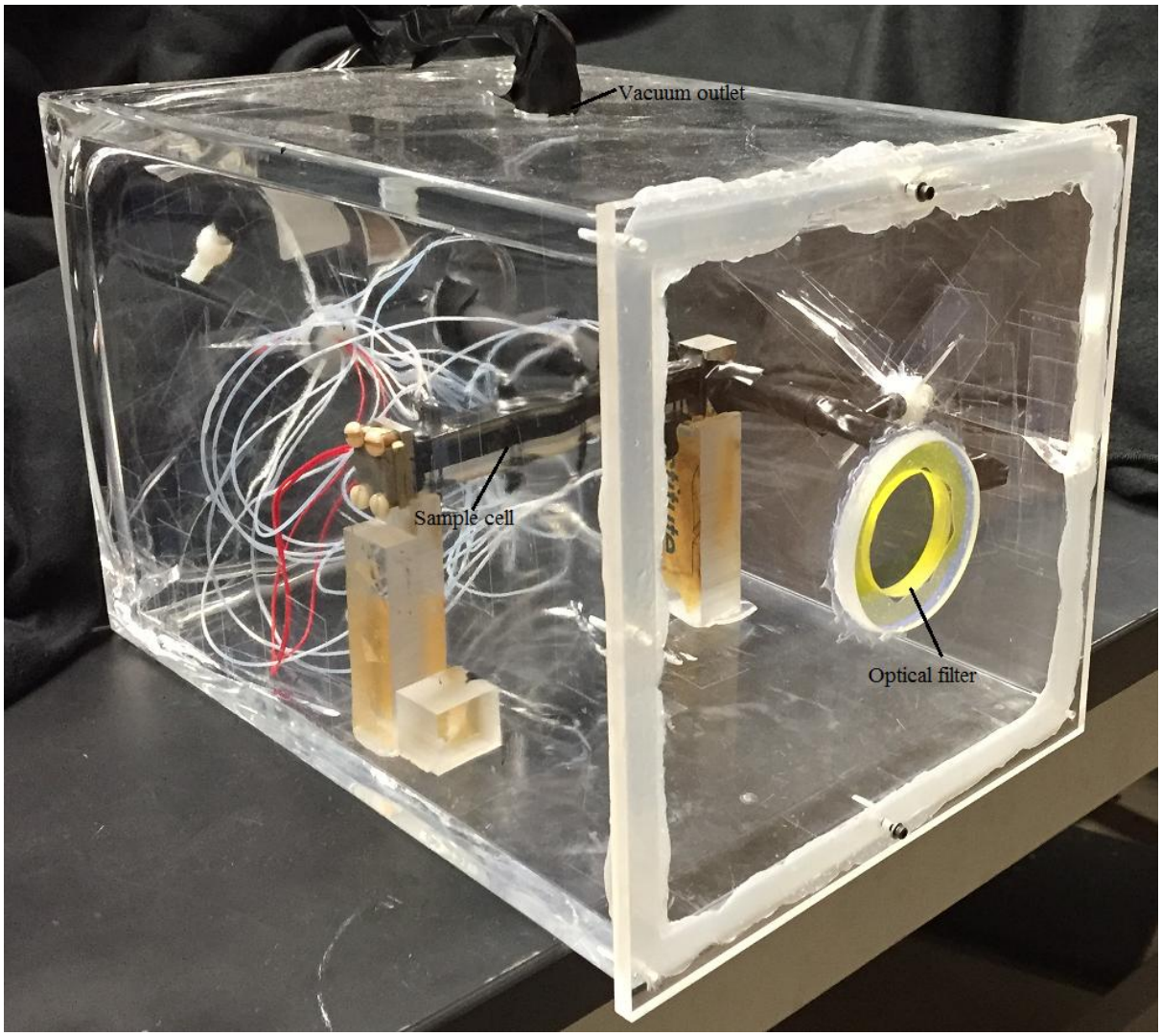

Figure 2.14. Vacuum chamber with a sample cell inside

CHAPTER 3: EXPERIMENT RESULTS

Part I Thermocouple results

3.1 Thermocouple results in kerosene in zero field

We want to study the field effect on convective flow. The result in zero field is measured as baseline calibration for two sample cells. The thermocouples results give eight temperatures at different positions in the fluid in each sample cell. First, all positions of thermocouples are labeled in figure 3.1.

Three letters are assigned for the thermocouples at two ends. For example, LLT means the thermocouple on the left top side of the left sample cell for parallel configuration, while RLT is the thermocouple on the left top side of the right sample cell with anti-parallel configuration. The middle thermocouples are labeled by 3 letters plus 1 number. LM1B is the first middle thermocouple on the bottom of the left sample cell, and LM2T means the second middle top thermocouple of the left sample etc.

In the experiments, kerosene is the solvent of the magnetic fluid. Since kerosene is non magnetic, the result in two configurations are the same. Figure 3.2a and 3.2b are the temperature profiles from thermocouples in kerosene without magnetic field; and Figure 3.2c and 3.2d are the temperature profiles in kerosene with microspheres without magnetic field. The error bar in temperature profile is $\pm 0.5^{o}C$ as it shows in figure 3.2a.

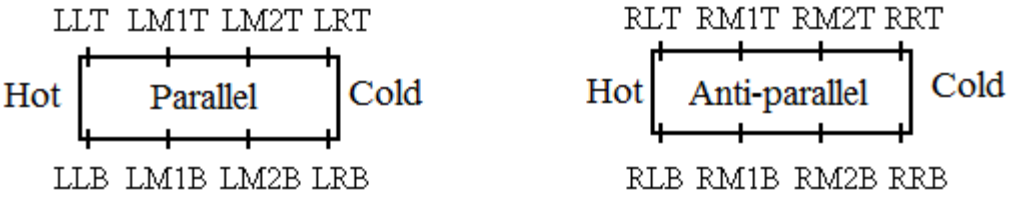

Figure 3.1. Thermocouples' positions in two sample cells.

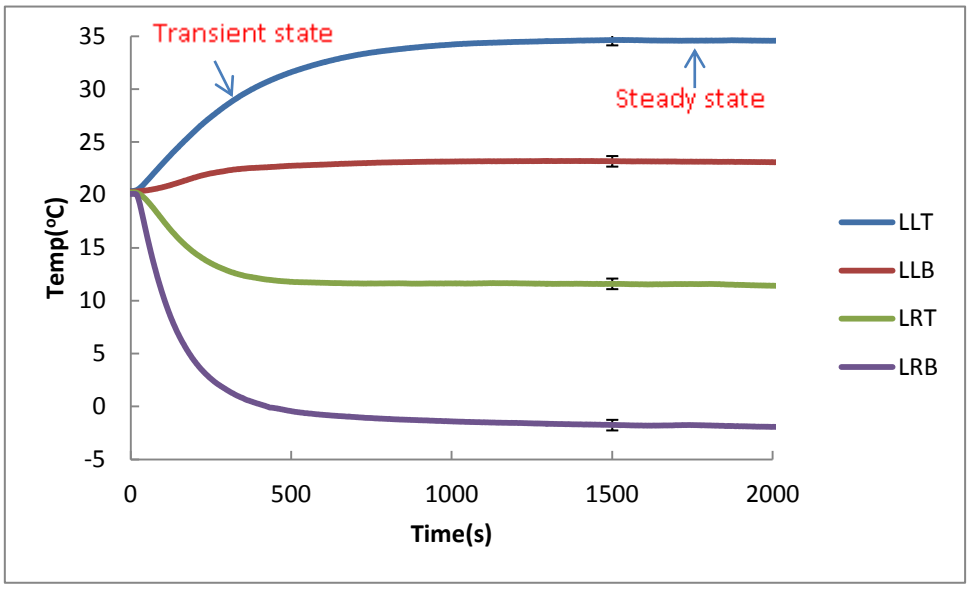
Transient state
Steady state
35
30
25
20
15
10
5
0
-5
Temp(°C)
0
500
1000
1500
2000
Time(s)
LLT
LLB
LRT
LRB

(a)

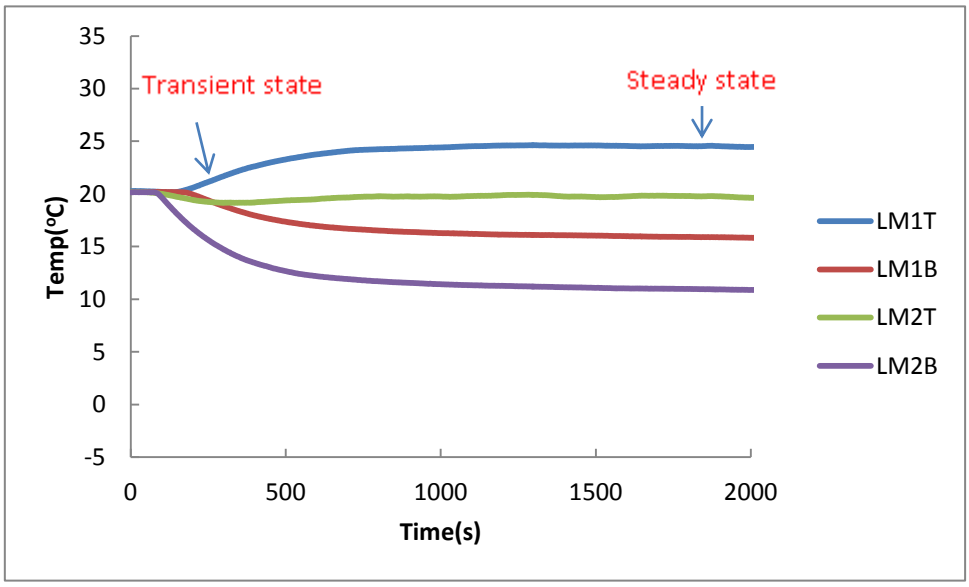
Transient state
Steady state
35
30
25
20
15
10
5
0
-5
Temp(°C)
0
500
1000
1500
2000
Time(s)
LM1T
LM1B
LM2T
LM2B

(b)

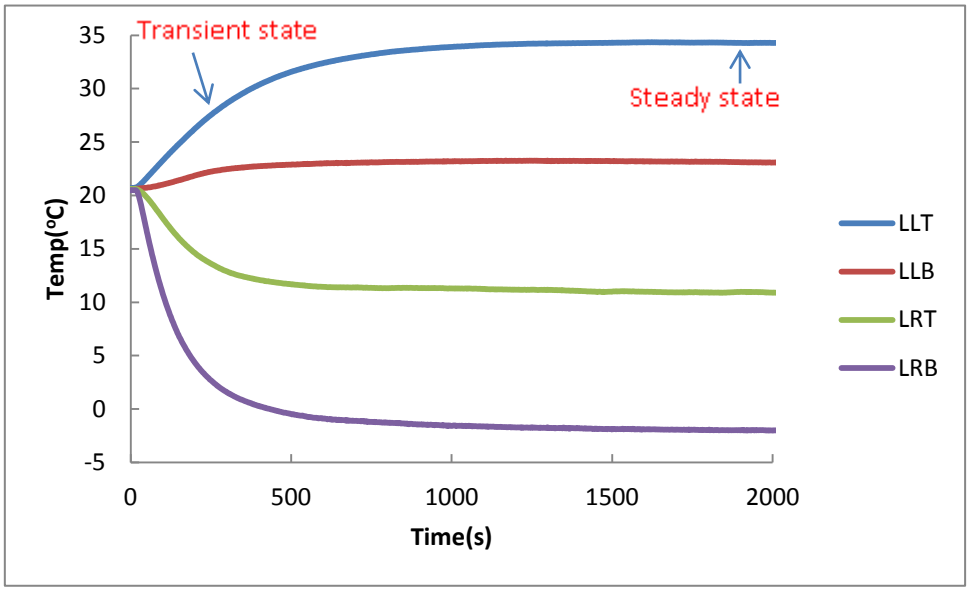
Transient state
Steady state
35
30
25
20
15
10
5
0
-5
Temp(°C)
0
500
1000
1500
2000
Time(s)
LLT
LLB
LRT
LRB

(c)

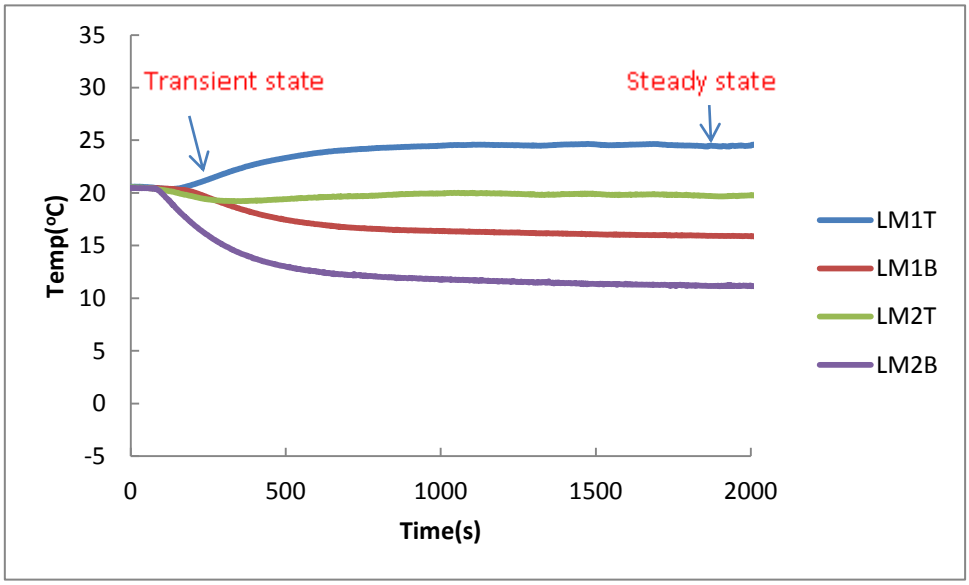
Transient state
Steady state
35
30
25
20
15
10
5
0
-5
Temp(°C)
0
500
1000
1500
2000
Time(s)
LM1T
LM1B
LM2T
LM2B

(d)

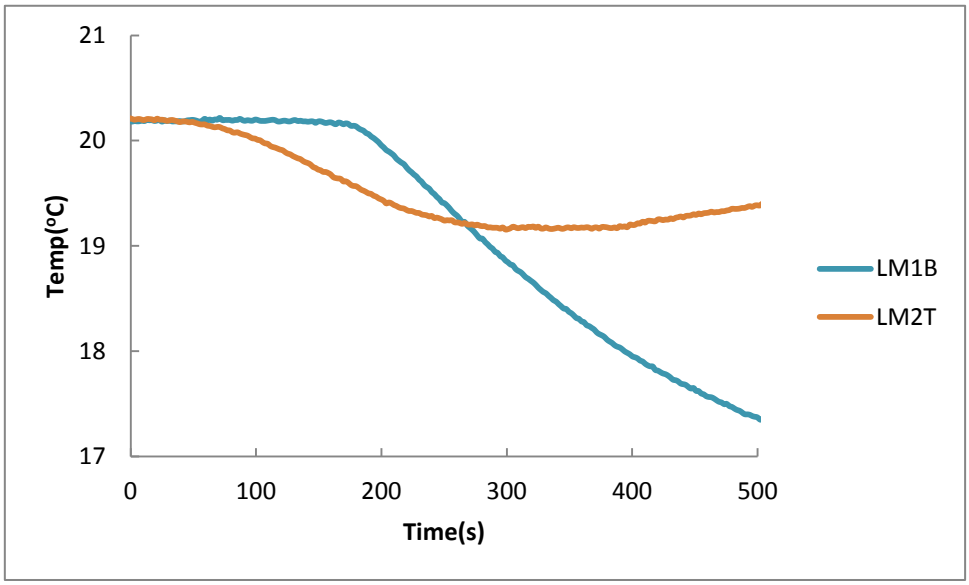

(e)

Figure 3.2. Time dependent temperature in kerosene at (a) 4 corner thermocouples, (b) 4 middle thermocouples, (c) 4 corner thermocouples for PTV method with microspheres, (d) 4 middle thermocouples for PTV method with microsphere, and (e) LM1B and LM2T in kerosene in short time.

The transient state and steady state are indicated in Figure 3.2. The temperature is increasing from heating side and decreasing from cooling side. The temperature profile reaches steady state after 2000 seconds. From the figure 3.2a-3.2d, the temperature distributions in kerosene with or without microspheres are basically the same because of low volume concentration (1%).

In the figure 3.2, if there is only conduction in the fluid after applying heating and cooling, the temperatures of the thermocouples which have same distance to the heating and cooling aluminum block, for example, LLT and LLB, should be same. It is clear that LLT and LLB have different temperature change right after heating and cooling applied due to convection. Figure 3.2e shows the temperature at LM2T and LM1B in kerosene before 500s, it is found that temperature at LM1B is higher than LM2T before 260s because LM1B is close to hot side. After 260s, the temperatures at LM1B and LM2T exchange values, this suggests convection has occurs before 200s.

3.2 Thermocouple results in a magnetic fluid

The temperature distribution in the magnetic fluid in zero field is basically same as in kerosene as show in figure 3.3 because of the low volume fraction of the magnetic fluid (1%).

The thermocouple results for the magnetic fluid with 1% concentration in step fields (chapter 2.3) are presented in figures 3.4 and 3.5. For the left sample cell (figure 3.4), where the magnetic field gradient and thermal gradient are parallel, when the magnetic field is applied, the temperatures of thermocouples close to the heating side (LLT LLB) were reduced and the temperatures of thermocouples close to the cooling side (LRT LRB) were increased. The temperatures at hot side decrease with increasing field, and the temperature at cold side increases with increasing field. The field dependence saturates at $B_{max} \geq 800G$. Temperature difference across sample decreasing means the magnetic fields enhance the thermal transfer in the magnetic fluid in parallel configuration.

While in the right sample cell (figure 3.5), where the magnetic field gradient and the thermal gradient are anti-parallel, when the magnetic field is applied, the temperatures of thermocouples close to the heating side (RLT RLB) were increased and the temperature of thermocouples close to the cooling side(RRT RRB) were decreased, the field effect increases with increasing field. The temperatures at cold side reach saturation at $B_{max} \geq 800G$, and the temperatures at hot side keep increasing all the time. In this configuration, the temperature difference across sample increases with fields, which means the magnetic fields suppress the thermal transfer in the magnetic fluid. For the results from thermocouples in the middle as

shown in figure 3.10b and 3.11b, the temperature change is more complicated, we will discuss it in detail in chapter 4.

Figure 3.6 shows the temperature differences across the sample cells vs. magnetic fields in step fields on the bottom and top. Parallel top $\Delta T = T_{LLT} - T_{LRT}$, Parallel bottom $\Delta T = T_{LLB} - T_{LRB}$, anti-parallel top $\Delta T = T_{RLT} - T_{RRT}$, anti-parallel bottom $\Delta T = T_{RLB} - T_{RRB}$. In left cell, where the magnetic field gradient and thermal gradient are parallel, when we increase the magnetic field, the temperature differences across the sample cell decrease; and for right cell, where the magnetic field gradient and thermal gradient are anti-parallel, when we increase the magnetic field, the temperature differences also increases; the higher the field the higher temperature difference.

Figure 3.7 and 3.8 show the temperature profile at four corner thermocouples in non-step field. In non-step field, only one field, for example $B_{max} = 200G$, is applied at steady state of zero field measure t = 2000s then the field is turn off at t = 3000s. The same trend in non-step fields can be observed as in step field that temperatures at hot side decrease in parallel configuration and increase in anti-parallel configuration, temperatures at cold side have move in opposite directions compared with its at hot side.

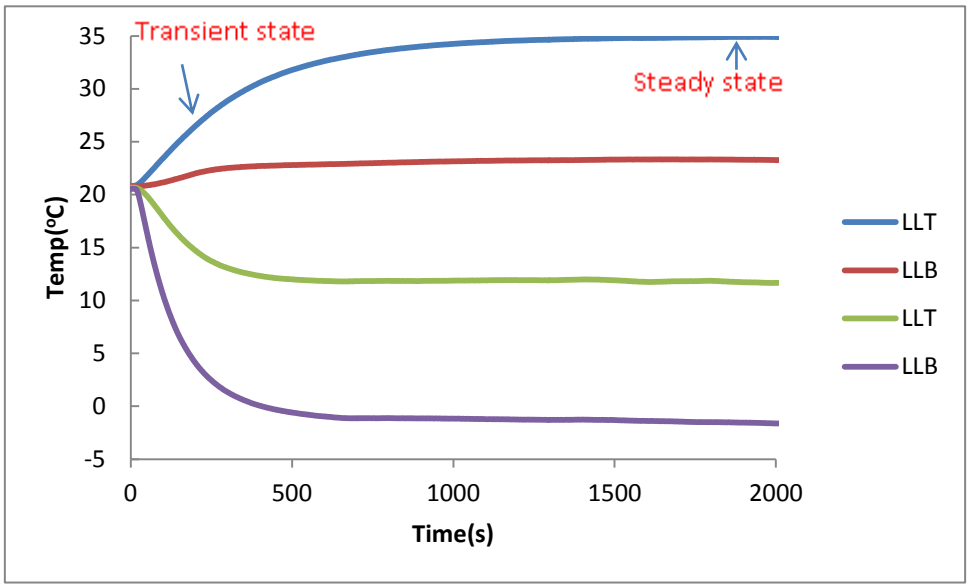

(a)

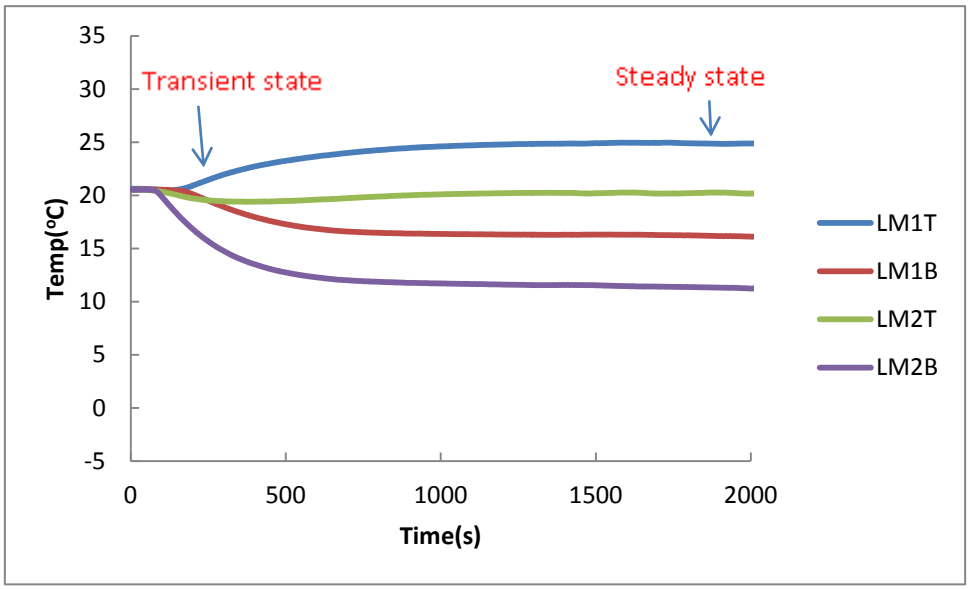

(b)

Figure 3.3. Time dependent temperature at (a) 4 corner thermocouples, and (b) 4 middle thermocouples in a magnetic fluid in zero field.

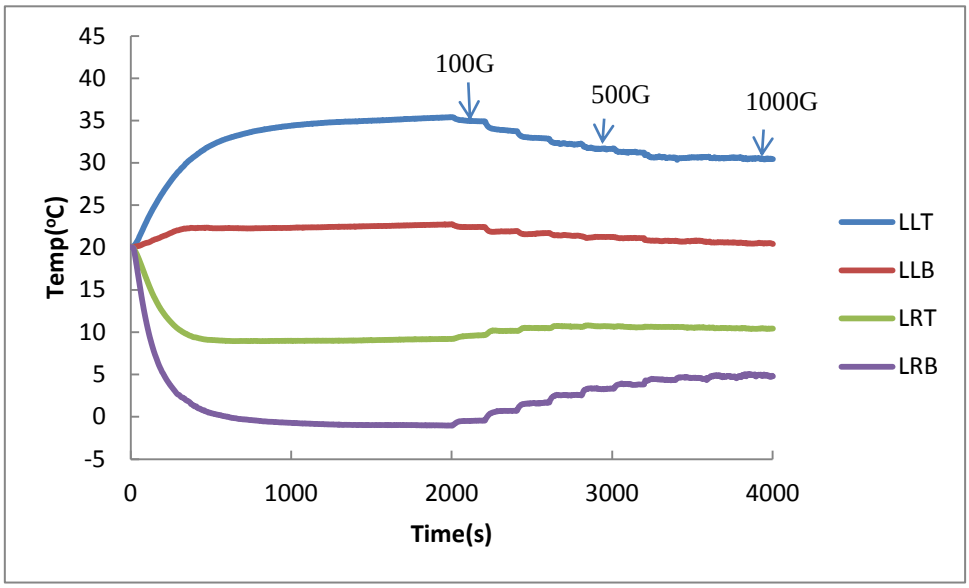

(a)

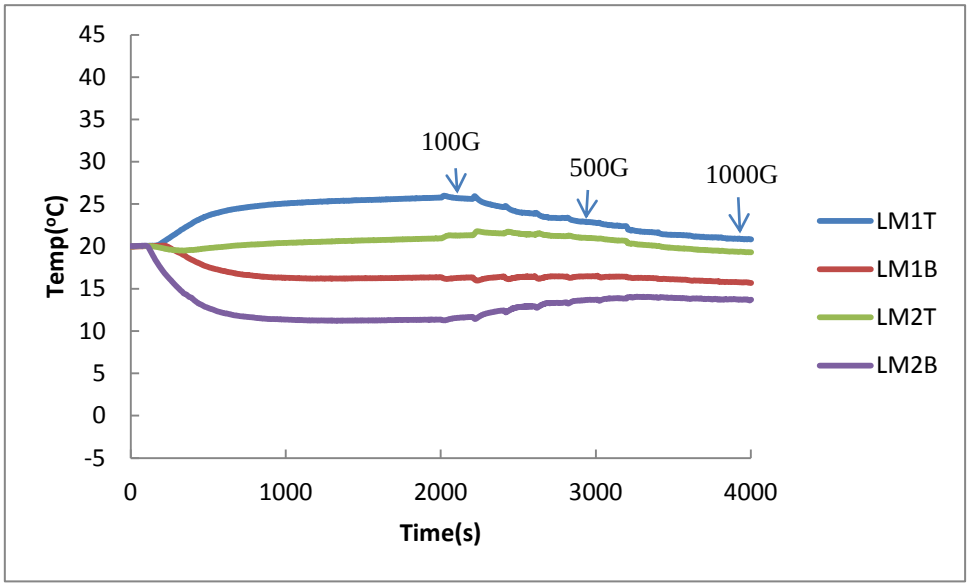

(b)

Figure 3.4. Temperature Vs. time at (a) 4 corner, and (b) 4 middle thermocouples of the magnetic fluid in parallel configuration in step fields.

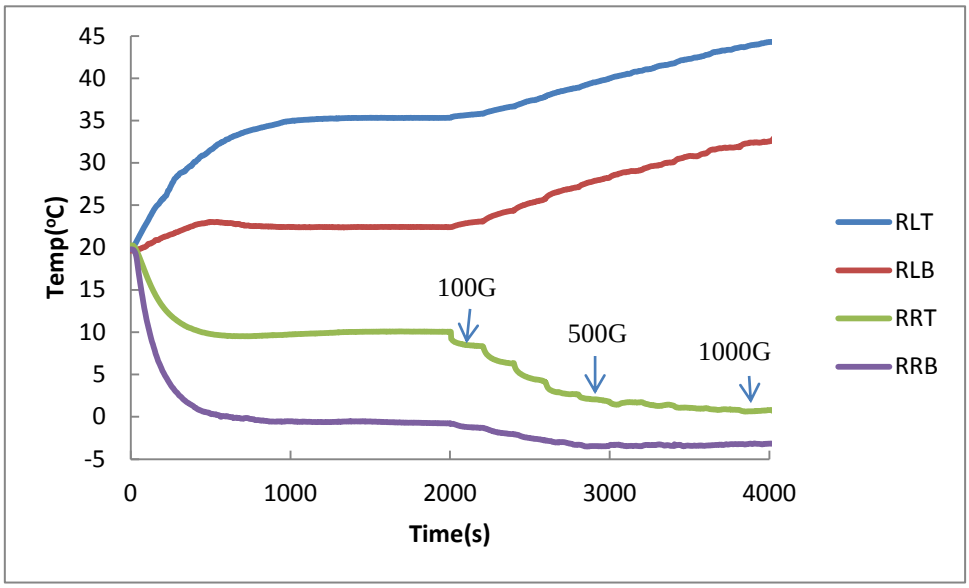

(a)

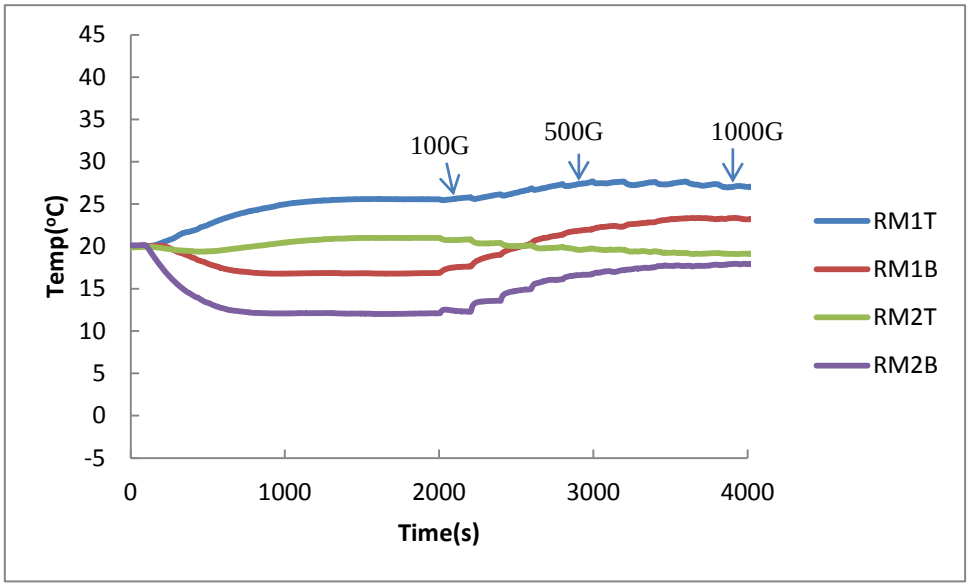

(b)

Figure 3.5. Temperature Vs. time at (a) 4 corner and, (b) 4 middle thermocouples of the magnetic fluid in anti-parallel configuration in step fields.

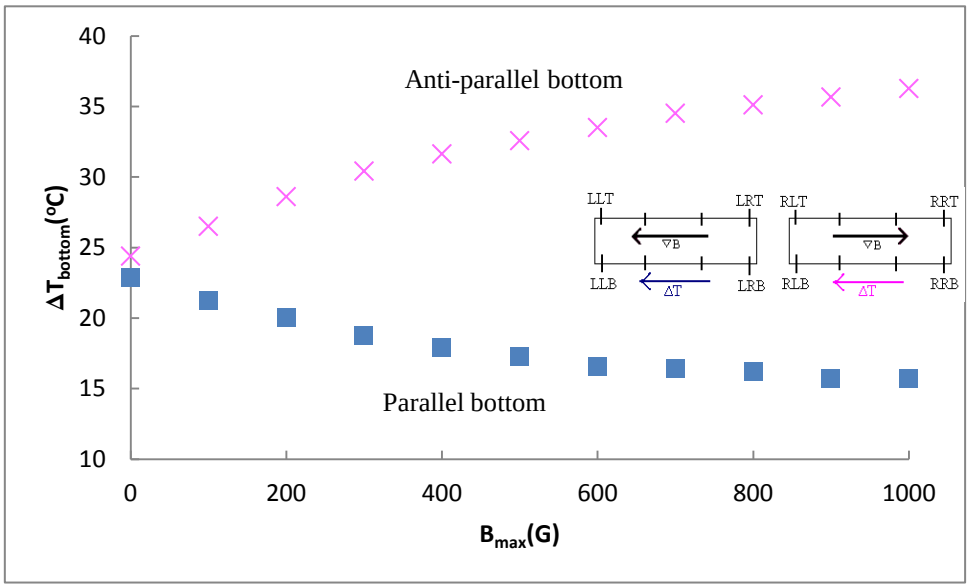

(a)

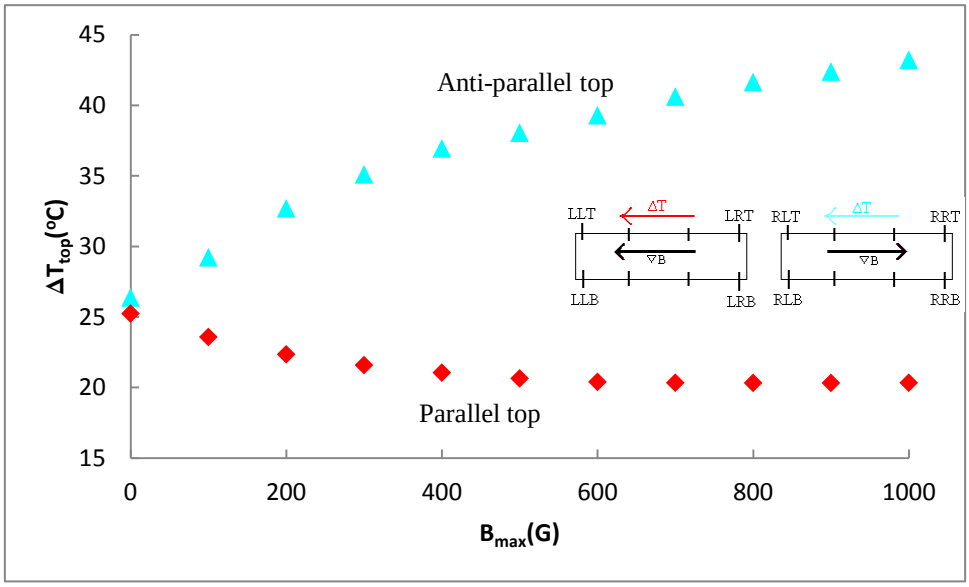

(b)

Figure 3.6. Temperature differences across the cells on the (a) bottom, and (b) top in a magnetic fluid in step fields.

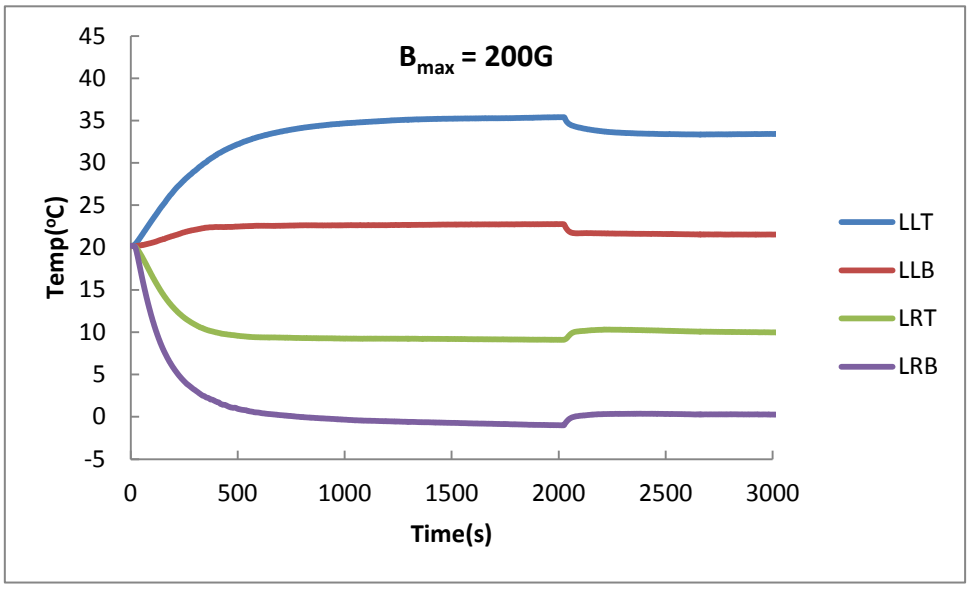
B_{max} = 200G
Temp(°C)
45
40
35
30
25
20
15
10
5
0
-5
0
500
1000
1500
2000
2500
3000
Time(s)
LLT
LLB
LRT
LRB

(a)

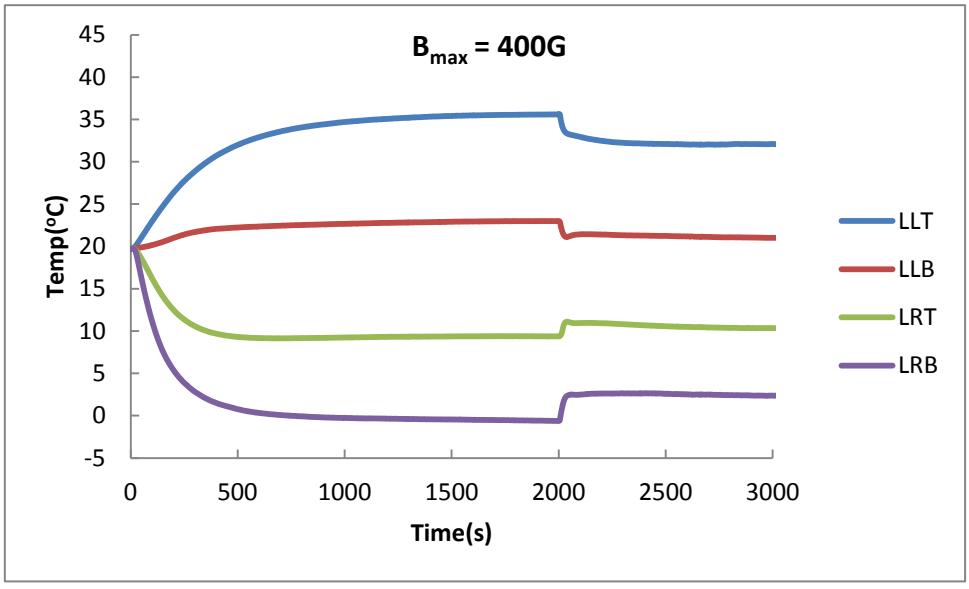
B_{max} = 400G
Temp(°C)
45
40
35
30
25
20
15
10
5
0
-5
0
500
1000
1500
2000
2500
3000
Time(s)
LLT
LLB
LRT
LRB

(b)

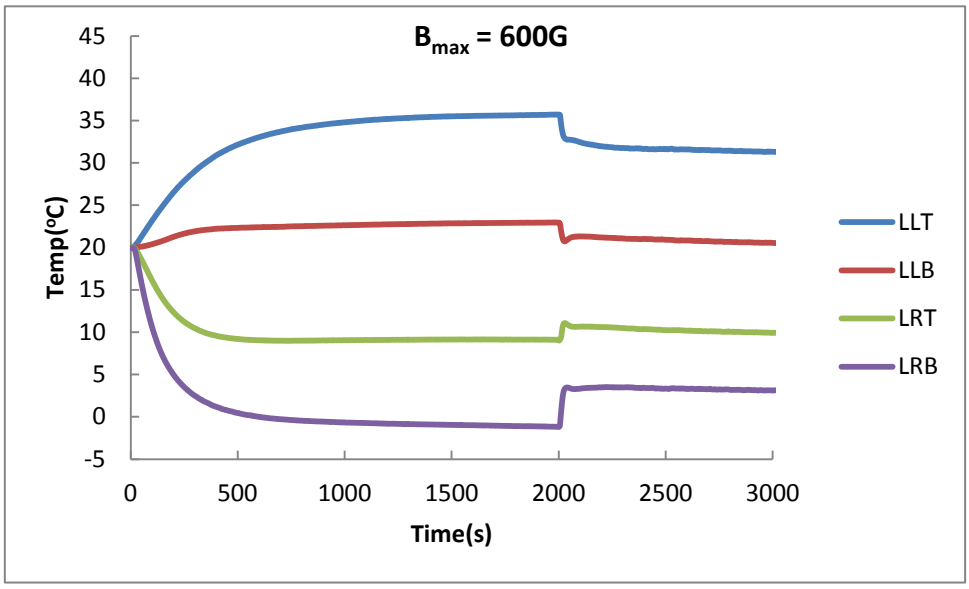
B_{max} = 600G
Temp(°C)
45
40
35
30
25
20
15
10
5
0
-5
0
500
1000
1500
2000
2500
3000
Time(s)
LLT
LLB
LRT
LRB

(c)

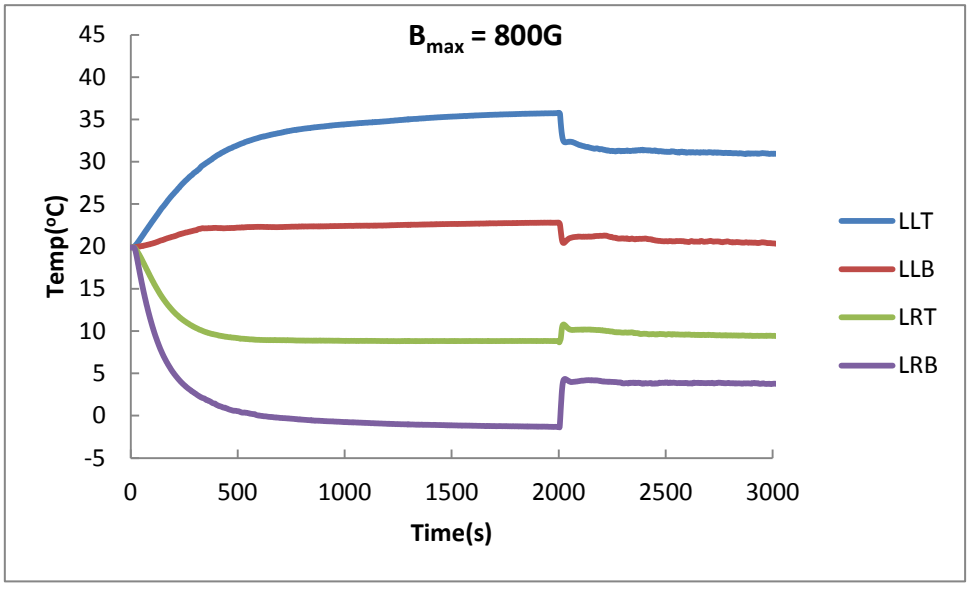
B_{max} = 800G
Temp(°C)
45
40
35
30
25
20
15
10
5
0
-5
0
500
1000
1500
2000
2500
3000
Time(s)
LLT
LLB
LRT
LRB

(d)

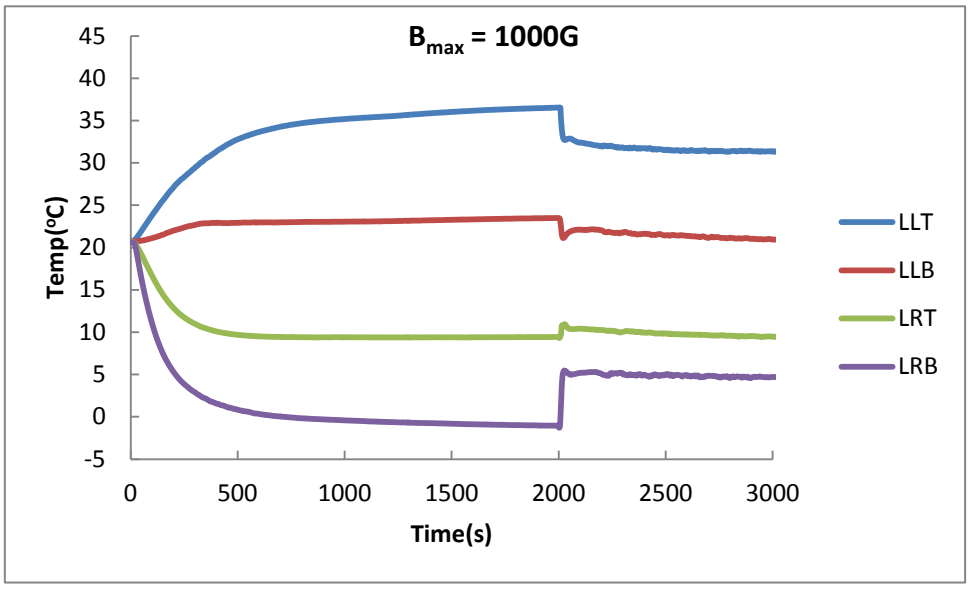

(e)

Figure 3.7. Temperature *vs.* time at four corner thermocouples in a magnetic fluid in parallel configuration in B_{max}= (a)200G, (b) 400G, (c)600G, (d) 800G, and (e) 1000G.

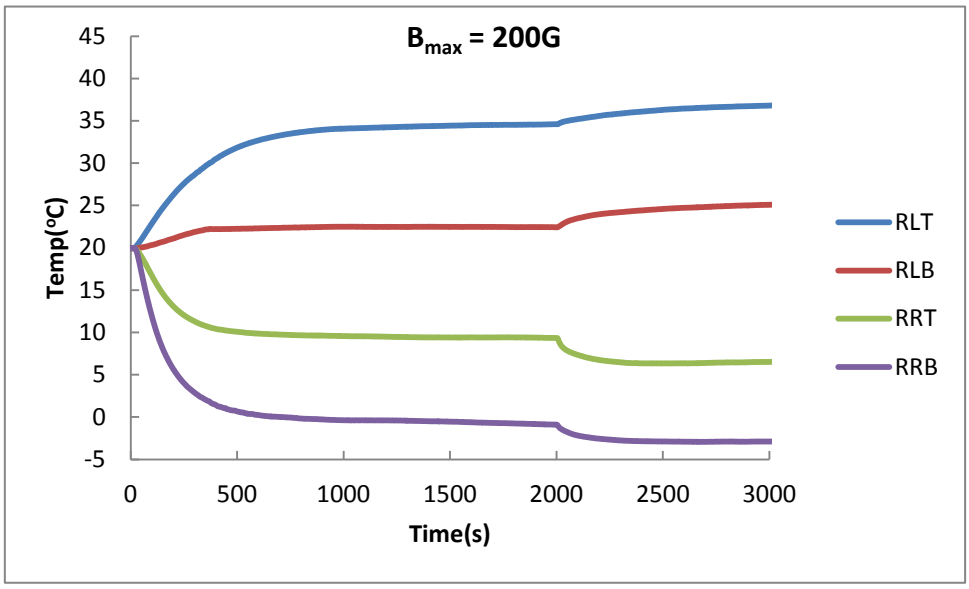
B_{max} = 200G
Temp(°C)
45
40
35
30
25
20
15
10
5
0
-5
0
500
1000
1500
2000
2500
3000
Time(s)
RLT
RLB
RRT
RRB

(a)

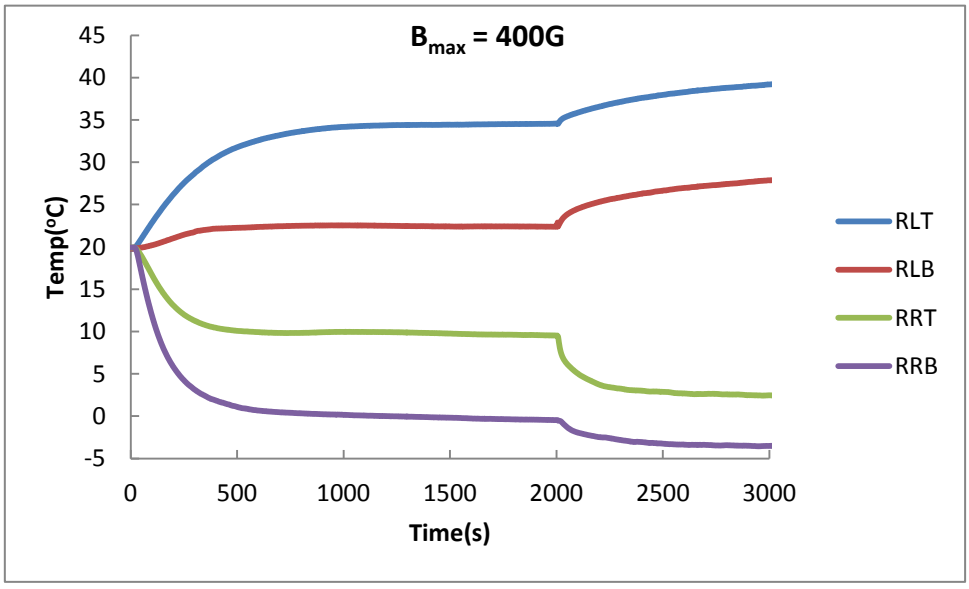
B_{max} = 400G
Temp(°C)
45
40
35
30
25
20
15
10
5
0
-5
0
500
1000
1500
2000
2500
3000
Time(s)
RLT
RLB
RRT
RRB

(b)

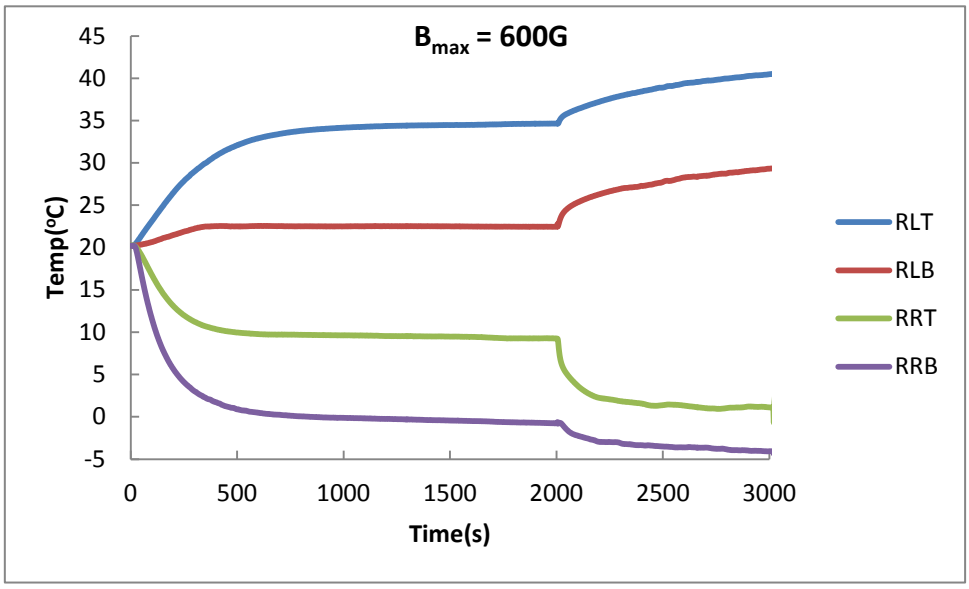
B_{max} = 600G
Temp(°C)
45
40
35
30
25
20
15
10
5
0
-5
0
500
1000
1500
2000
2500
3000
Time(s)
RLT
RLB
RRT
RRB

(c)

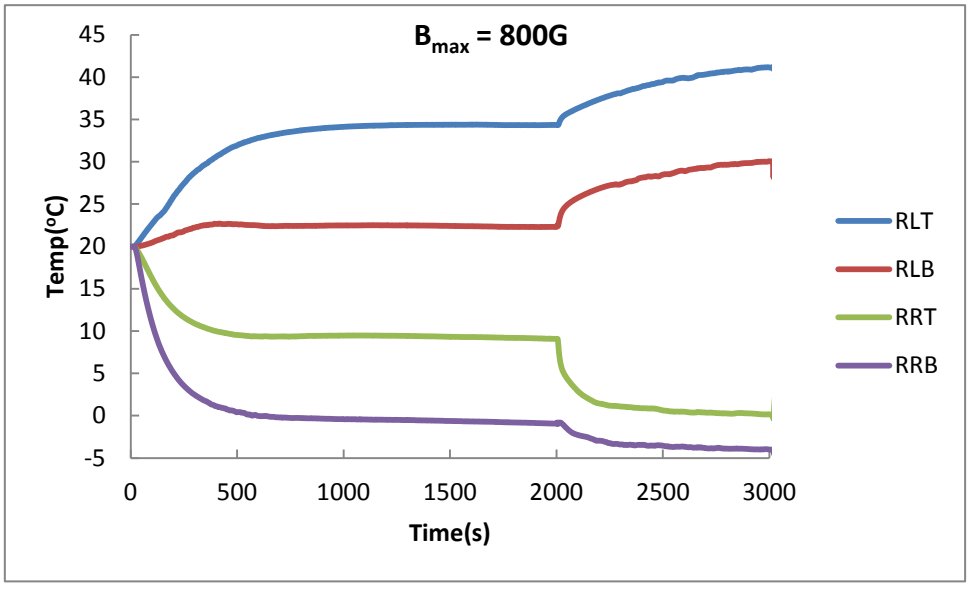
B_{max} = 800G
Temp(°C)
45
40
35
30
25
20
15
10
5
0
-5
0
500
1000
1500
2000
2500
3000
Time(s)
RLT
RLB
RRT
RRB

(d)

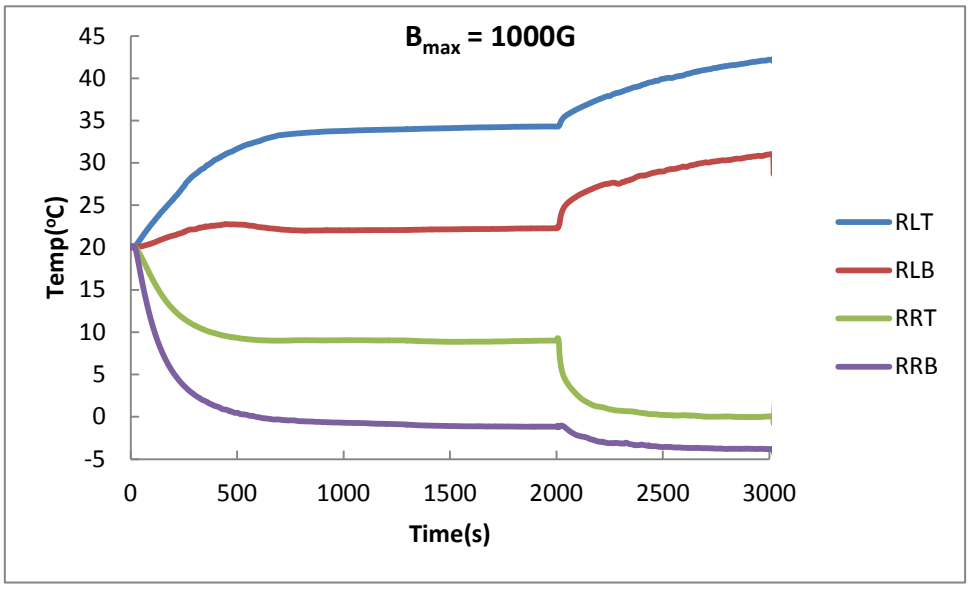

(e)

Figure 3.8. Temperature *vs.* time at four corner thermocouples in a magnetic fluid in anti-parallel configuration in B_{max}= (a)200G, (b) 400G, (c)600G, (d) 800G, and (e) 1000G.

Part II PTV and TSP Results

3.3 Flow pattern by using PTV and optical flow method in zero field in kerosene

The thermocouples only can measure temperature at eight locations. PTV and TSP can be used to obtained velocity and streamline pattern. The microspheres are added into the kerosene for flow visualization in zero field to establish the base velocity and pattern. We have five different runs for the kerosene with the microspheres in zero field in the same experiment configuration. High-resolution velocity fields are extracted from images of microspheres by using the optical flow method. The outline of the procedure to process the pictures is following:

(1) To select a region of interest and save a sequence of images for processing

(2) Run flow velocity program to generate a sequence of extracted velocity fields from the pictures obtained from step1 by optical flow method.

(3) To plot the velocity and streamline of the microspheres

Figure 3.9 and 3.10 show the selected velocity fields and streamlines at 20s, 50s, 100s, 2000s and 2015s in the same run. Velocity field is the velocity vector distribution at each point in a subset of space [47], It is represented by a collection of arrows to indicate the velocity magnitude and direction at each point. Streamline is the field line from velocity vector tangent to show the massless direction of fluid [48]. In the transient state in t = 0-100s, as shown in Figs. 3.9a-3.9c [or 3.10a-3.10c], the local circulating flows start at the heating and cooling ends of the cell (the left and right ends) and expand toward the middle of the cell.

The velocity and the size of the circulating flow near the cooling end are much larger than those at the heating end. After t = 2000s, as shown in Figs. 3.9d and 3.9e [or 3.10d-3.10e], the single overall circulating roll is formed, where the flow moves from the right to left in the lower half of the cell and from the left to right in the upper half of the cell. There is a shear layer between the two opposite flows. The shear layer is a region of flow with significant velocity gradient. The vortical structures are clearly observed around shear layer. Figure 3.11 shows the time-averaged velocity vectors and streamlines after t = 2000s.

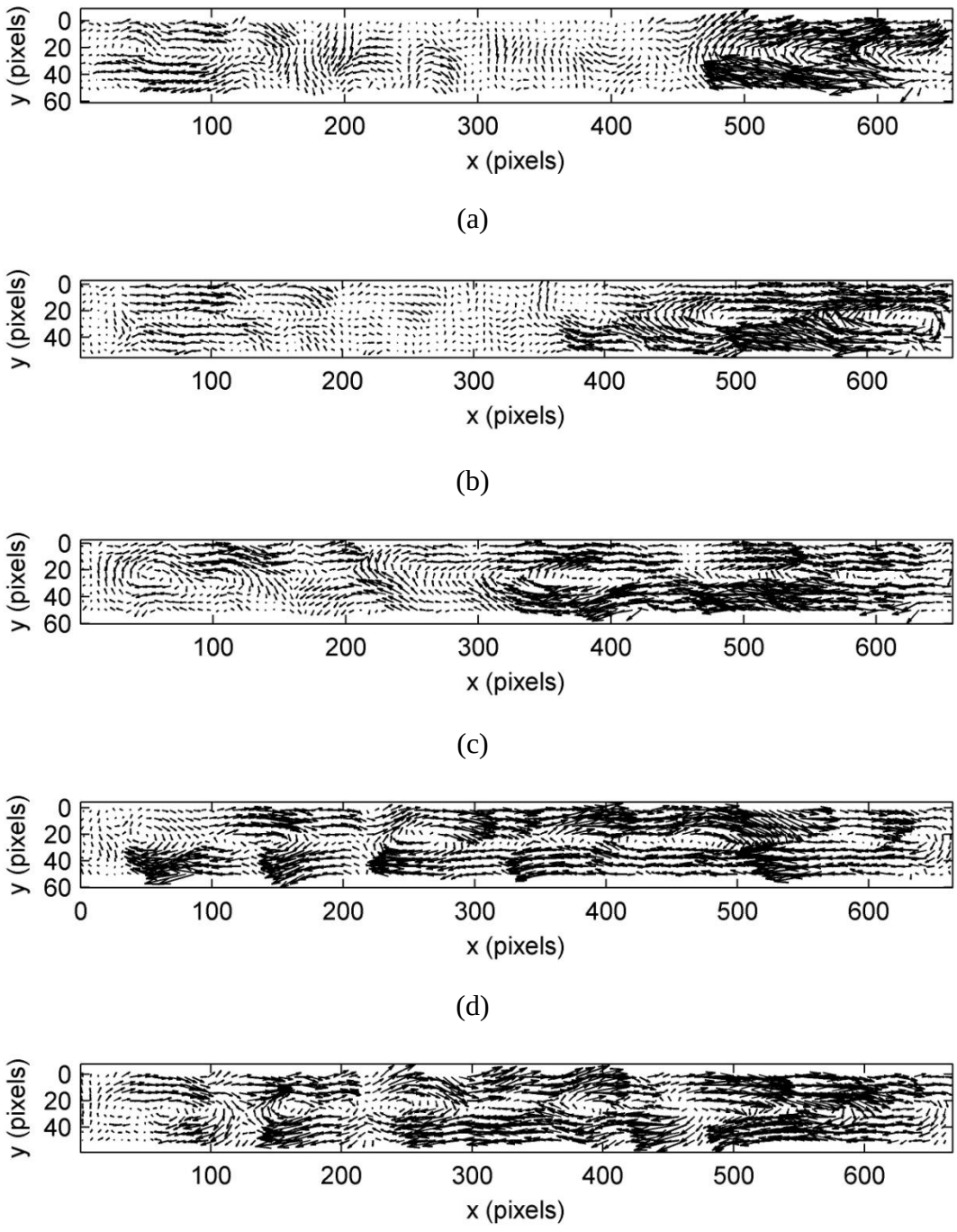

Figure 3.9. Velocity fields at (a) 20s, (b) 50s, (c)100s, (d)2000s, and (e) 2015s for kerosene in zero field.

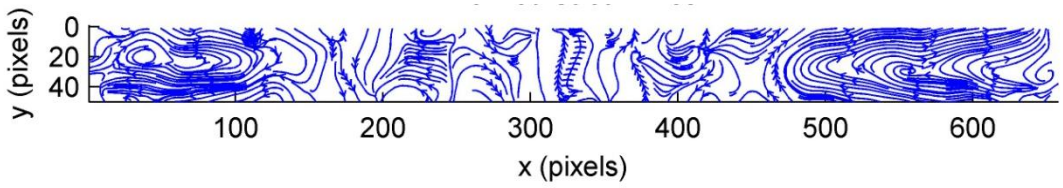

(a)

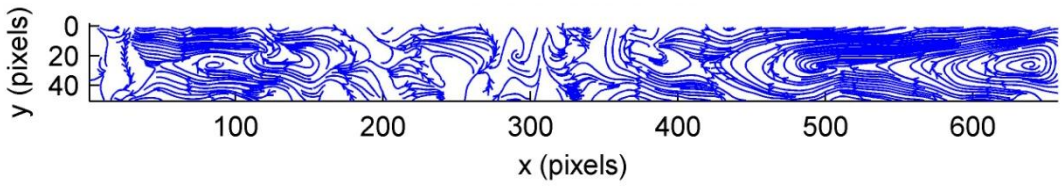

(b)

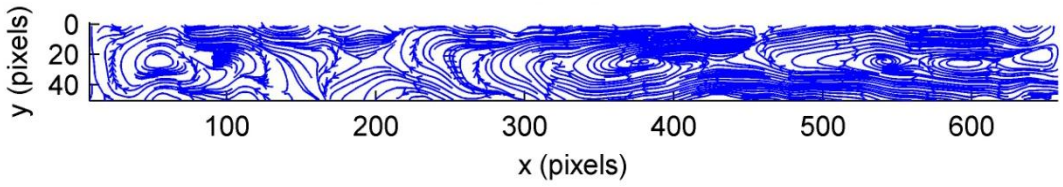

(c)

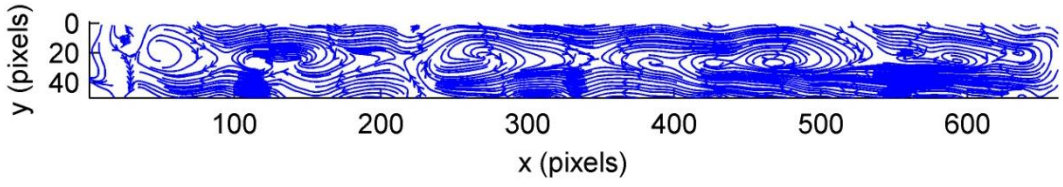

(d)

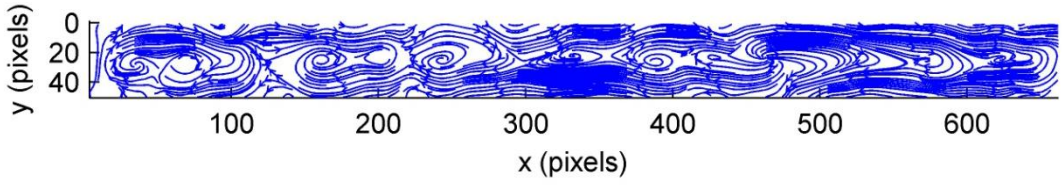

(e)

Figure 3.10. Streamlines at (a) 20s, (b) 50s, (c) 100s, (d)2000s, and (e) 2015s for kerosene in zero field.

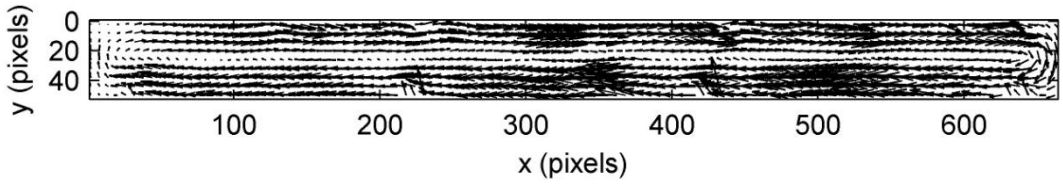

(a)

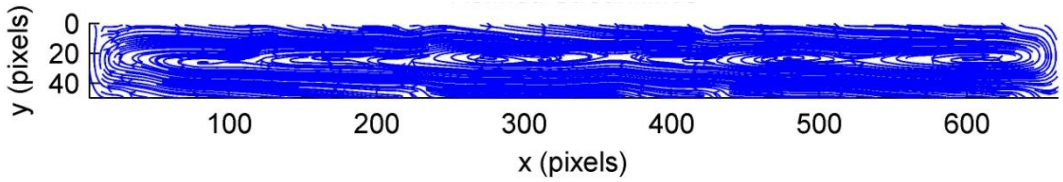

(b)

Figure 3.11. (a) Time-averaged velocity field, and (b) time-averaged streamlines at t=2000s for kerosene in zero field.

Because the fluid movement is dynamic, the flow velocity and pattern is calculated at steady state with a ten seconds average. At transient state the velocity and pattern between different runs is also slightly different possibly due to chaotic nature at short time. When we use the result from kerosene as baseline for the magnetic fluid in applied fields, the velocities and patterns from five runs are averaged at steady state.

To average all five different runs, first we need to scale all the images to the same dimension. Here we select 700 by 50 pixels as standard dimension. All five runs are scaled up or down to this size. Then we average all scaled data. At the steady state, the average flow velocity is 0.2 ±0.05 cm/s. Figure 3.6 are the averaged velocity field and streamlines from 5 different runs. There is one main convection roll across the sample cell, the fluid goes up at left (hot) side and moves from left to right on the top, then it goes down when cooled at right (cold) side and moves back to left on the bottom. The average velocity and streamline are used as baseline for further analysis when the fields are applied.

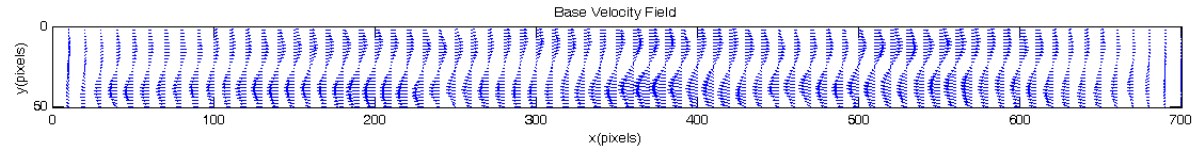

(a)

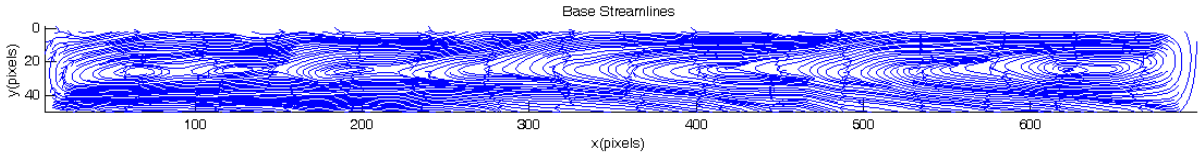

(b)

Figure 3.12. Averaged (a) velocity field, and (b) streamline at steady state in kerosene in zero field.

3.4 TSP imaging results in a magnetic fluid in zero field

Because the magnetic fluid is opaque, the flow velocity and flow pattern cannot be obtained by using microspheres with PTV method directly as in kerosene. For this reason, the temperature sensitive paint is used to image the detailed temperature distribution in the magnetic fluid and then the flow patterns are obtained. The TSP image processing procedure is flowing:

Step 1. Image averaging: To reduce the noise-to-signal ratio of the experiment, 20 images were averaged for every specific point in time during the experiment, for example, for steady state at t=2000s, 20 images taken from range 1999s to 2001s are averaged (10 frames /s).

Step 2. Alignment and dark image correction: Each image has to be aligned horizontally first. Dark image is acquired when the illuminating light is off. The dark image intensity is from the dark current noise of the CCD camera and the ambient light. It has to be subtracted from data images to eliminate this noise.

Step 3. Intensity normalization: The normalized intensity is defined by the relative ratio between the intensity of real image to that of the reference image to eliminate the effects of non-homogenous illumination intensity, non-uniform luminophore concentration and uneven paint thickness (equation 2.1).

Step 4. Conversion to temperature: The conversion of the normalized intensity to temperature was accomplished by using fitted coefficients obtained from experimental calibration relation in chapter 2.6.

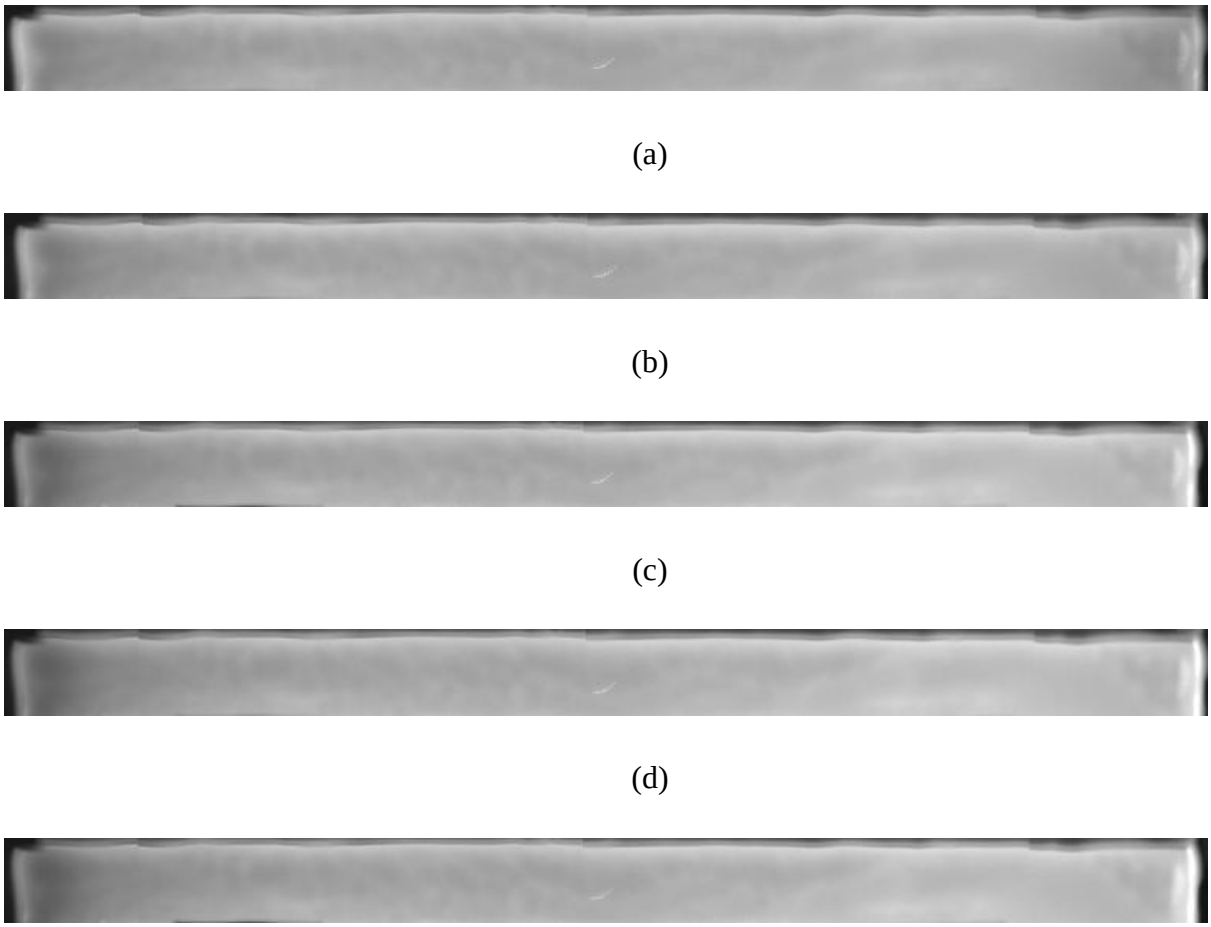

(a)

(b)

(c)

(d)

(e)

Figure 3.13. Original TSP intensity image at (a) t = 0s, (b) t = 100s, (c) t = 500s, (d) t = 1000s ,and (e) t = 2000s in a magnetic fluid in zero field.

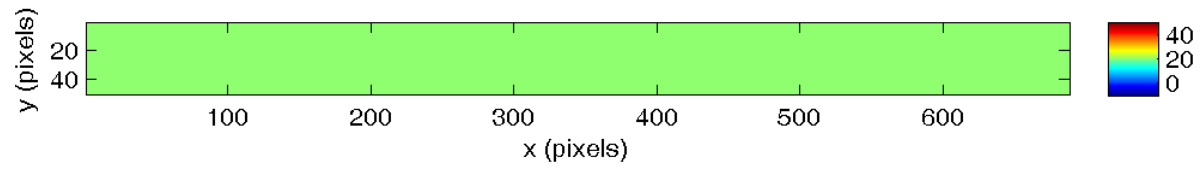

(a)

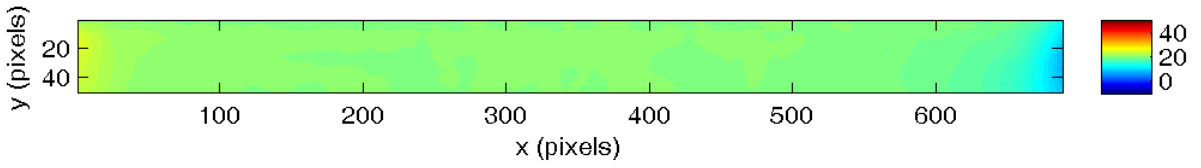

(b)

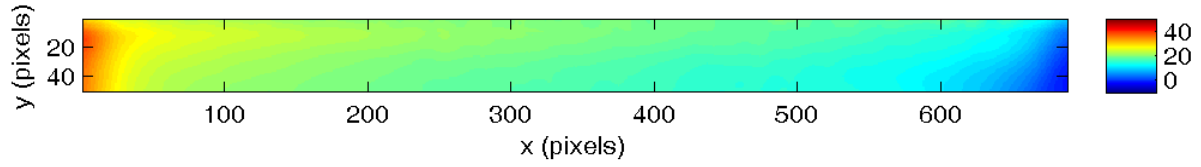

(c)

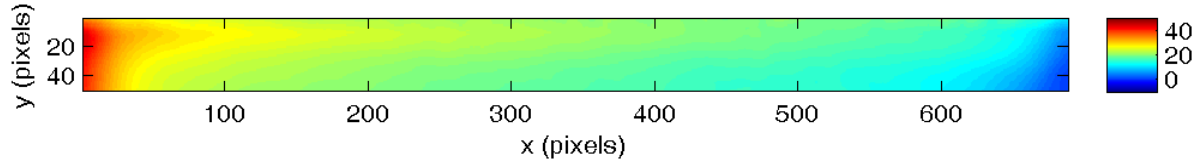

(d)

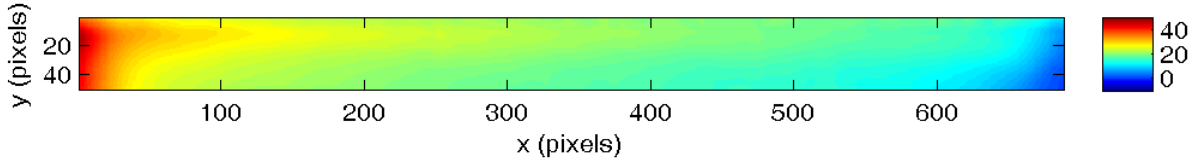

(e)

Figure 3.14. Temperature profiles converted from figure 3.8 at (a) t=0s, (b) t=100s, (c) t=500s, (d) t=1000s, and (e) t=2000s in a magnetic fluid in zero field.

Figure 3.13 shows the original TSP intensity image in the magnetic fluid in zero field at 0s, 100s, 500s, 1000s and 2000s from step 1. Figure 3.14 is the converted temperature image at 0s, 100s, 500s, 1000s and 2000s from TSP image from step 4.

The intensity of TSP image corresponds to the local temperature. The higher the temperature the lower the intensity, the lower the intensity the darker the image, and vice versa. From figure 3.13, when heating and cooling applied, at hot side, because fluorescent intensity decreases with increasing temperature, this part of image gets darker in high temperature; while at cold side, because the intensity increases with reduced temperature, it becomes brighter in low temperature. These intensity images in figure 3.13 are converted to temperature profile in figure 3.14, which shows how the temperatures change with time through the intensity change after heating and cooling are applied. At t = 0, the figure 3.14a shows the uniform room temperature in the sample, figure 3.14b-e show the temperatures change after heating and cooling are applied, the temperature increase at left end (heating side) and decrease at right end (cooling side). The hot and cold temperature fronts propagate with time when the convection develops. Then the temperature profile reaches steady state when the convection is stable.

The results from TSP are consistent with the results from thermocouples at their locations. Our purpose is to use TSP images to find the flow patterns. The TSP result for magnetic fluid in zero field is to establish baseline for flow patterns in fields.

3.5 TSP results in a magnetic fluid in step fields

The thermocouples method cannot provide information for study of fluid motion. TSP is used to measure more complete temperature profile for further flow velocity and flow pattern analysis.

Figure 3.15a and 3.15b show the surface temperature fields from 0 to B_{max}= 1000G in two configurations with figure 3.15a for parallel configuration and figure 3.15b for anti-parallel configuration. The image for B = 0 is the steady-state temperature image at t = 2000s in zero field which is same for two configurations. The other images were taken at 200s after fields are applied (refer to the experiment procedure in step fields in chapter 2.3), First, the same trend in temperature change in TSP is similar to what is found in thermocouple. After the fields are applied, temperatures decrease at hot side and increase at cold side in parallel configuration, while the opposite effect is observed in anti-parallel situation. The higher the fields the larger the field effects.

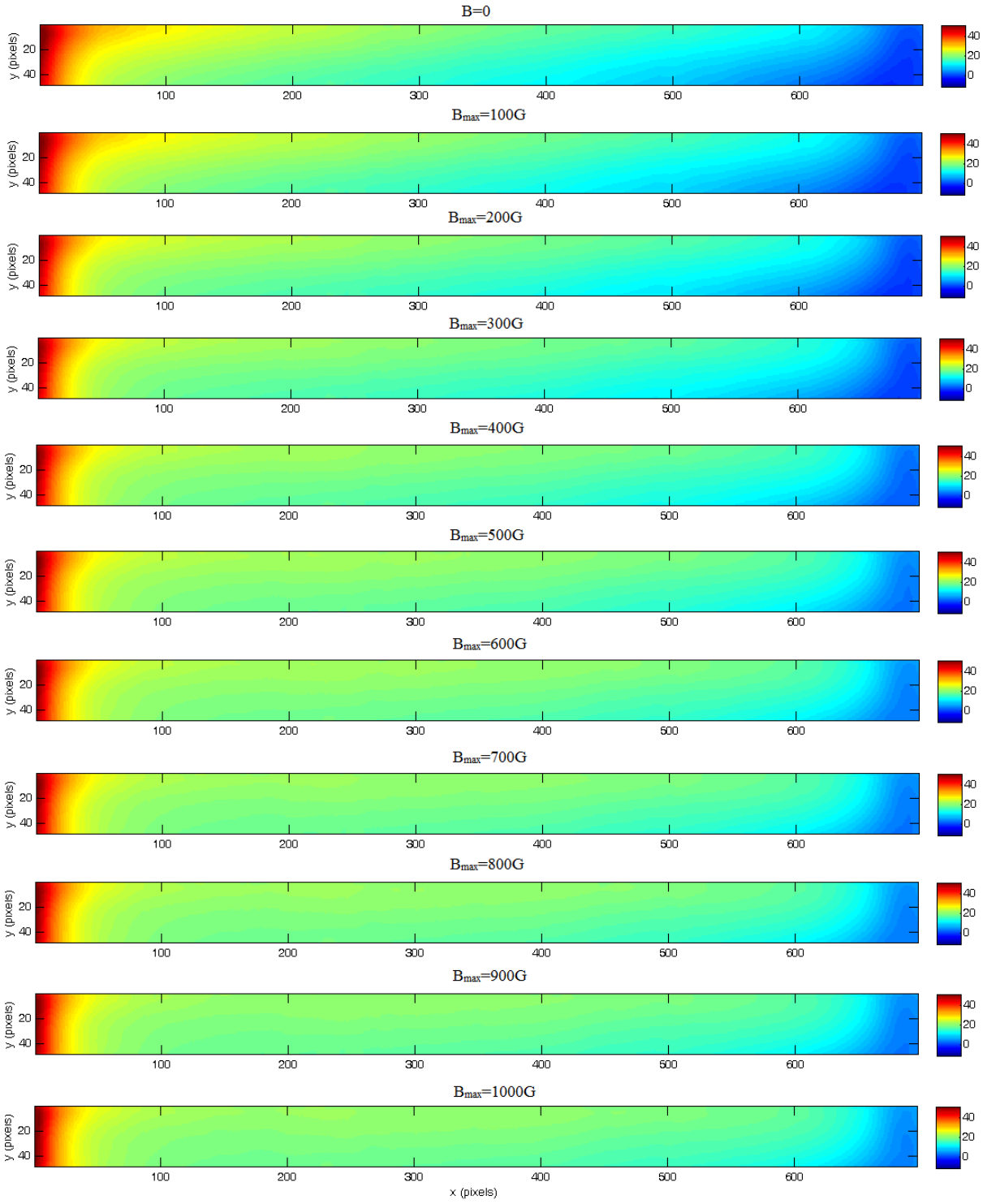
B=0
Bmax=100G
Bmax=200G
Bmax=300G
Bmax=400G
Bmax=500G
Bmax=600G
Bmax=700G
Bmax=800G
Bmax=900G
Bmax=1000G
y (pixels)
x (pixels)
20
40
100
200
300
400
500
600
0

(a)

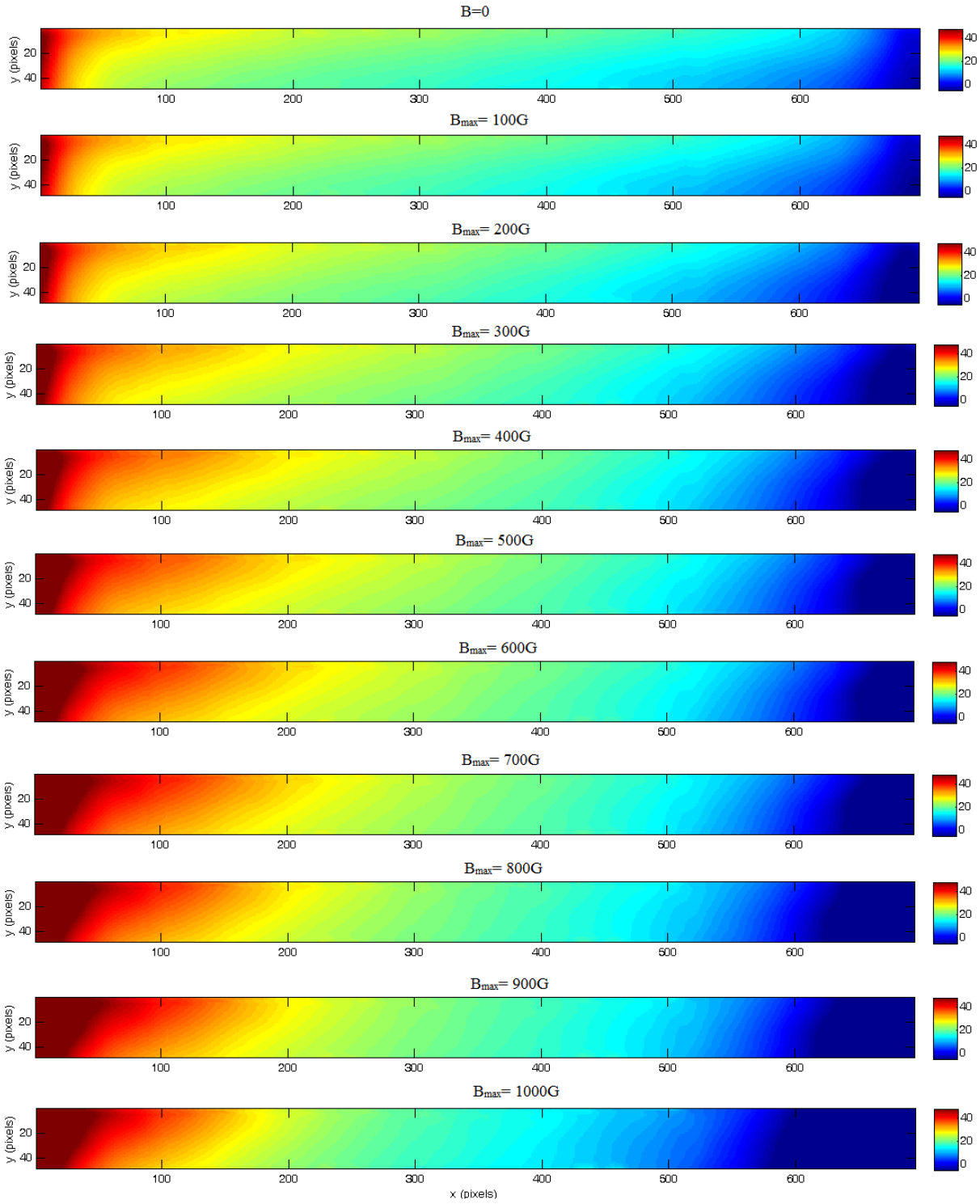

(b)

Figure 3.15. Temperature profile in step-fields in (a) parallel, and (b) anti- parallel configuration in a magnetic fluid.

3.6 Method to extract flow velocity field and streamlines plots from TSP results

The optical flow method is used to get the perturbation velocity and streamline in fields from TSP [49]. In order to extract the velocity fields in the magnetic fluid, a two-step approach is proposed. In the first step, the high-resolution velocity fields are extracted from a sequence of images of the microspheres in carrier fluid in the cell by using the optical flow method (for details refer to chapter 3.2). The time-averaged velocity field is obtained as a base velocity field when a steady state of the flow is achieved at $t \geq 2000s$. Figures 3.12a and 3.12b show the base velocity field and streamlines in kerosene. We assume that the base velocity field of the magnetic fluid is the same as that of the kerosene fluid in steady state in zero field due to low volume concentration of the magnetic nano particles. The second step is to extract the perturbation velocity field of the magnetic fluid from temperature-sensitive paint (TSP) images when a magnetic field is applied at steady state. At this state, when the fields just applied, in a short time, the temperature change in the magnetic fluid is mainly due to the change of the fluid movement. From the temperature change at TSP, the velocity change can be extracted by using optical flow method. Combined with the base velocity field and streamlines in kerosene, we can get the velocity and streamline patterns for the magnetic fluid in applied magnetic fields. Then, the final velocity field is constructed by superposing the base velocity field and the perturbation velocity field. The physical meaning of the optical flow extracted from temperature images is described as follows. The energy equation for a 2D incompressible flow is [49, 50]

$$\partial T/\partial t+\nabla\bullet\left(\boldsymbol{u}T\right)=a\nabla^2T+Q \tag{3.1}$$

In two dimension coordinates (x,y), where T is the temperature in fluid, u_j $(j=1,2)$ are the velocity components, Q is a consistent heating power, $a=k/\rho c_p$ is the thermal diffusivity, and ρ is density, c_p is specific heat and k is thermal conductivity. We consider the decompositions $T=\langle T\rangle_t+T'$ and $\boldsymbol{u}=\langle\boldsymbol{u}\rangle_t+\boldsymbol{u}'$, where $\langle\bullet\rangle_t$ is the time averaging operator, T' and $\boldsymbol{u}'$ are the time dependent perturbation temperature and velocity, $\langle\boldsymbol{u}\rangle_t$ is the base velocity field, and $\langle T\rangle_t$ is the time averaged temperature field in zero field. The time averaged quantities satisfy the steady state transmit equation $\nabla\bullet\left(\langle\boldsymbol{u}\rangle_t\langle T\rangle_t\right)=a\nabla^2\langle T\rangle_t+Q$. In our experiment, $\langle\boldsymbol{u}\rangle_t$ is obtained by PTV method from microsphere images. Substitution of the decompositions into Eq. (3.1) yields

$$\partial T'/\partial t+\nabla\bullet\left(\boldsymbol{u}'\langle T\rangle_t\right)=f \tag{3.2}$$

Where $f=a\nabla^2T'-\nabla\bullet\left(T'\langle\boldsymbol{u}\rangle_t\right)-\nabla\bullet\left(T'\boldsymbol{u}'\right)$. In optical flow calculation, it is assumed that $f=0$ in the first-order approximation. By solving the optical flow Eq. (3.2), the perturbation velocity $\boldsymbol{u}'$ can be obtained. In our experiment, $\boldsymbol{u}'$ is defined as the velocity change induced by the applied magnetic fields. It is assumed that base velocity field $\langle\boldsymbol{u}\rangle_t$ remains the same in kerosene and the magnetic fluid. The velocity in the field is the base velocity superposed with perturbation velocity.

$$\boldsymbol{u}=\langle\boldsymbol{u}\rangle_t+\boldsymbol{u}' \tag{3.3}$$

3.7 Perturbation velocities and perturbation streamlines in a magnetic fluid

The perturbation velocity $\boldsymbol{u}'$ is the velocity change after the field is applied. The perturbation streamline is the streamline from perturbation velocity field. Figure 3.16 (parallel) and 3.17 (anti-parallel) show the TSP temperature fields with B_{max} = 0, 100G, 300G, 500G, 700G and 900G at 5s after the magnetic field is applied in two configurations. Figure 3.18 and 3.19 shows the perturbation velocity field extracted from figure 3.16 and 3.17 by using the optical flow method.

In parallel configuration, figure 3.18 shows that large perturbation velocity at left hot side corresponding to the large local field and field gradient. The direction of perturbation velocity is to up left, which can be observed both in velocity fields and streamlines. The main perturbation velocity direction is the same with the field gradient direction and temperature gradient (right to left). Its direction is also the same with the magnetic body force. While in anti-parallel configuration (figure 3.19), the direction of field gradient and magnetic body force is from left to right, but the perturbation field velocities show large magnitudes at both hot and cold sides depends on different fields. The directions of perturbation velocity also change with fields, which are different from parallel configuration. The magnetic body force in anti-parallel configuration is same with field gradient but opposite with temperature. We will discuss the magnetic body force in detail in chapter 4.5. The change of directions indicates the flow structure change due to the field effect. The detailed flow patterns will be presented with streamlines in chapter 3.8. Figure 3.20 and 3.21 are perturbation streamlines

obtained from figure 3.18 and 3.19, which show the same trend in perturbation velocity field.

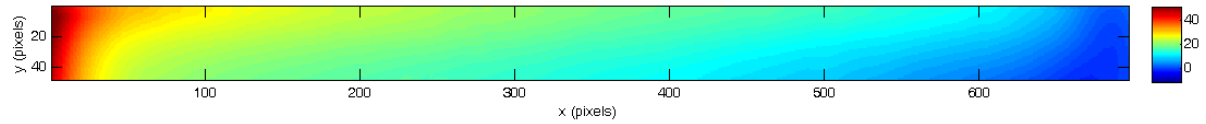

(a)

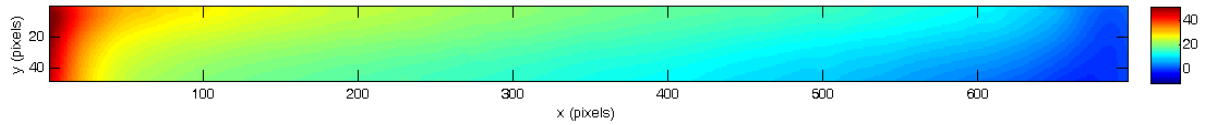

(b)

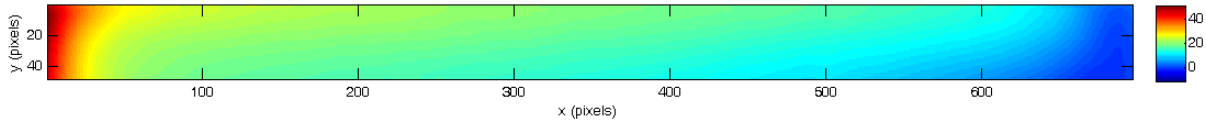

(c)

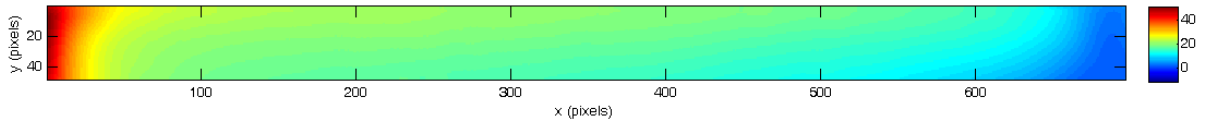

(d)

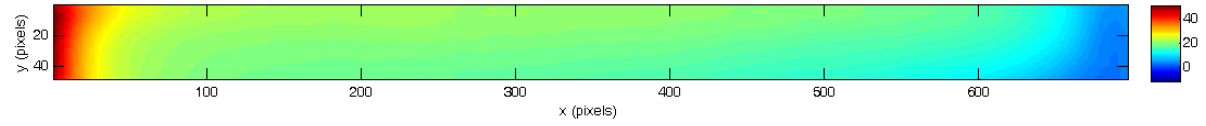

(e)

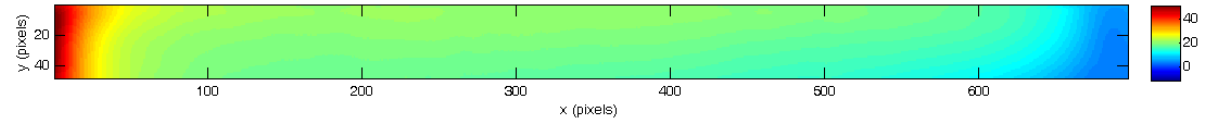

(f)

Figure 3.16. TSP temperature fields at (a) B_{max} = 0, (b) B_{max} = 100G, (c) B_{max} = 300G, (d) B_{max} = 500G, (e) B_{max} = 700G, and (f) B_{max} = 900G in parallel configuration in a magnetic fluid.

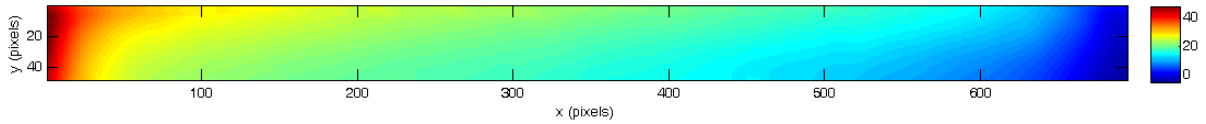

(a)

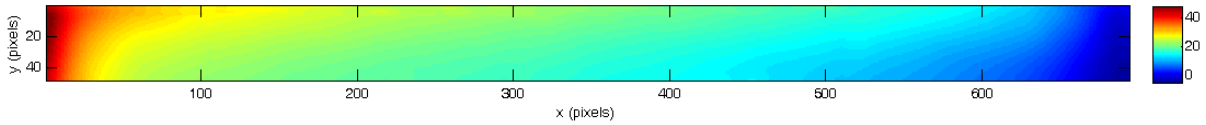

(b)

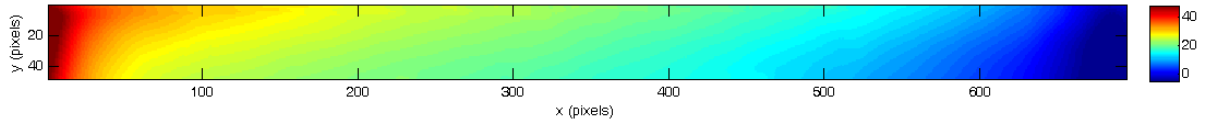

(c)

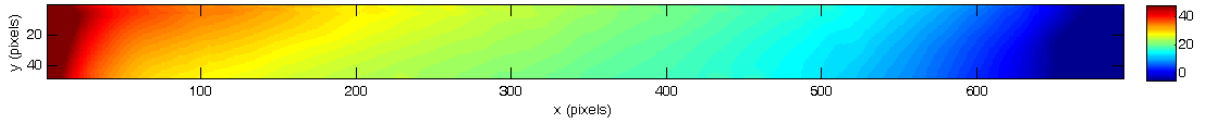

(d)

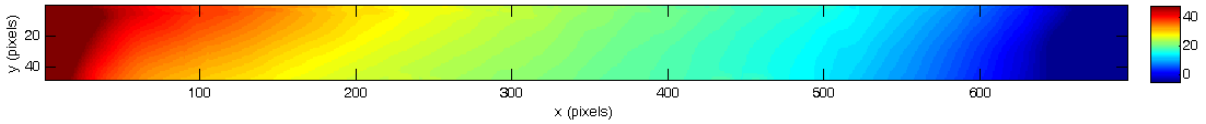

(e)

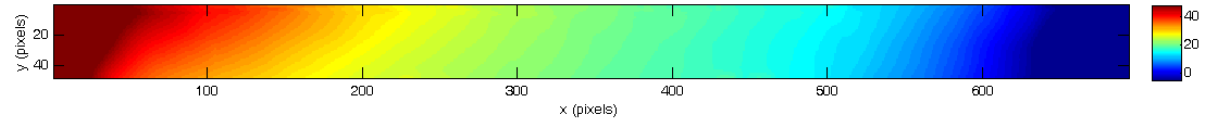

(f)

Figure 3.17. TSP temperature fields at (a) B_{max} = 0, (b) B_{max} = 100G, (c) B_{max} = 300G, (d) B_{max} = 500G, (e) B_{max} = 700G, and (f) B_{max} = 900G in anti-parallel configuration in a magnetic fluid.

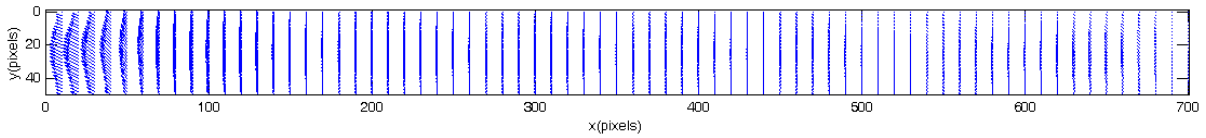

(a)

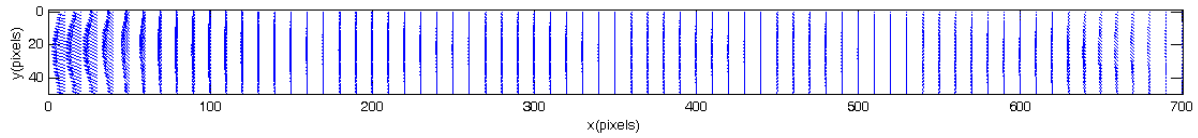

(b)

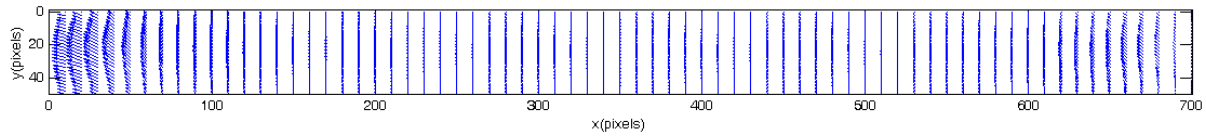

(c)

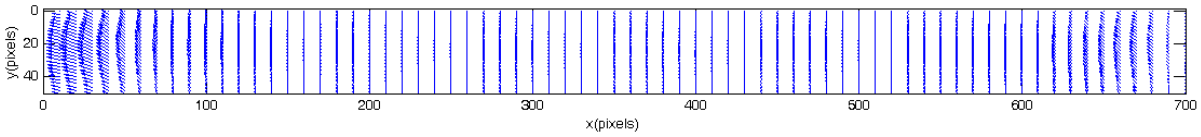

(d)

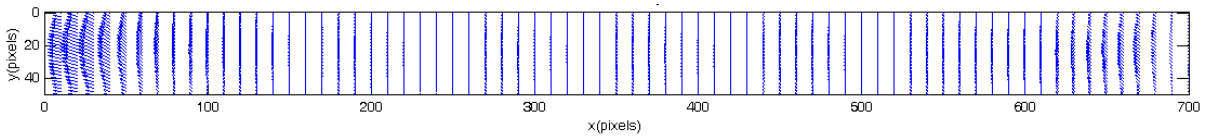

(e)

Figure 3.18. Perturbation velocity fields at (a) B_{max} = 100G, (b) B_{max} = 300G, (c) B_{max} = 500G, (d) B_{max} = 700G, and (e) B_{max} = 900G in parallel configuration in a magnetic fluid.

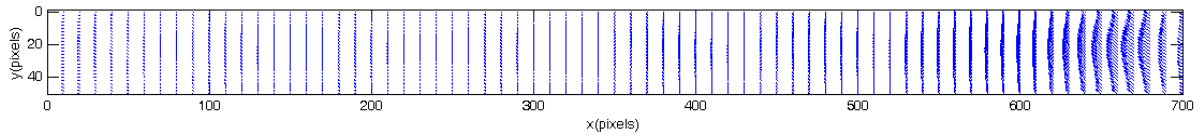

(a)

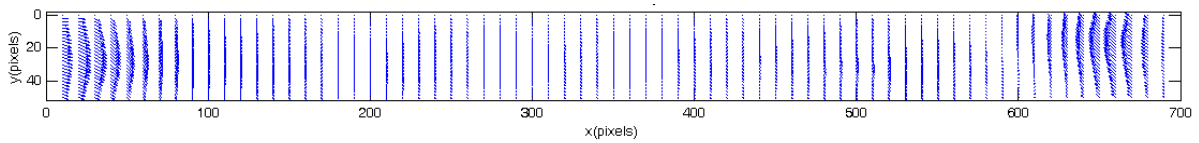

(b)

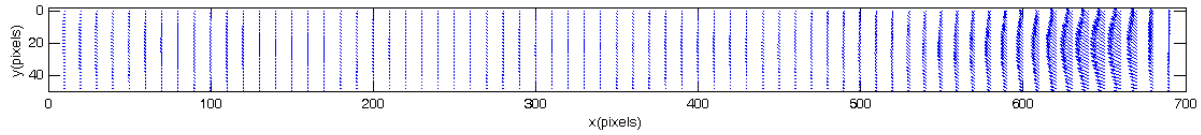

(c)

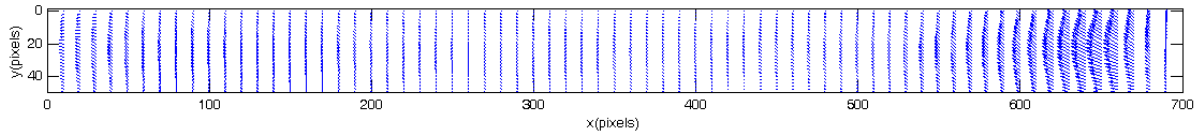

(d)

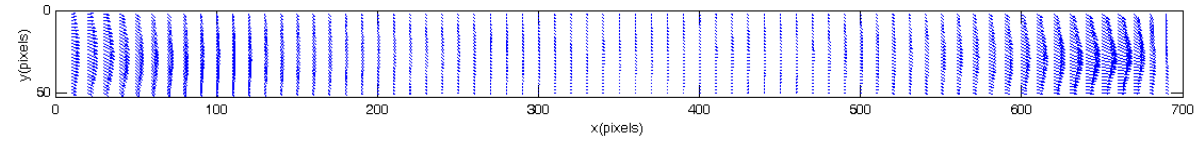

(e)

Figure 3.19. Perturbation velocity fields at (a) B_{max} = 100G, (b) B_{max} = 300G, (c) B_{max} = 500G, (d) B_{max} = 700G, and (e) B_{max} = 900G in anti-parallel configuration in a magnetic fluid.

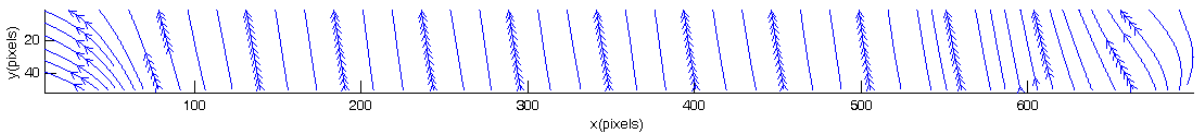

(a)

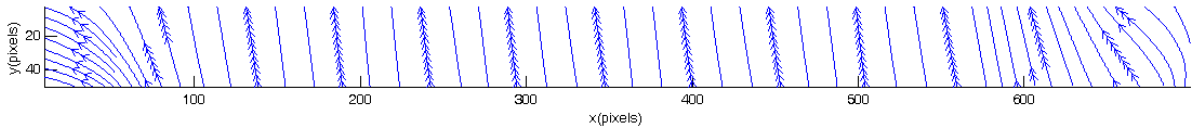

(b)

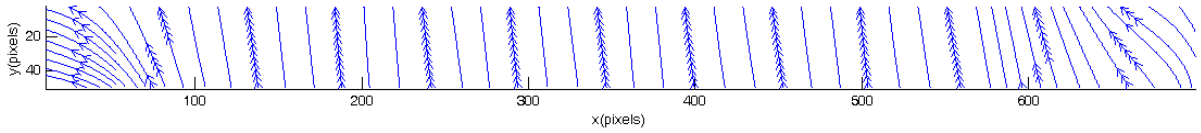

(c)

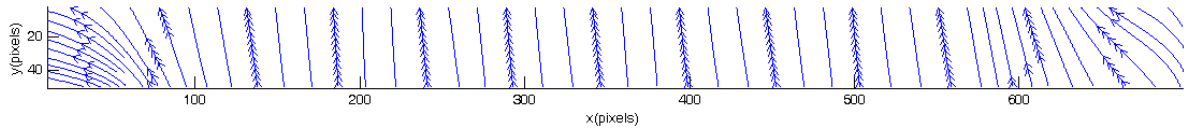

(d)

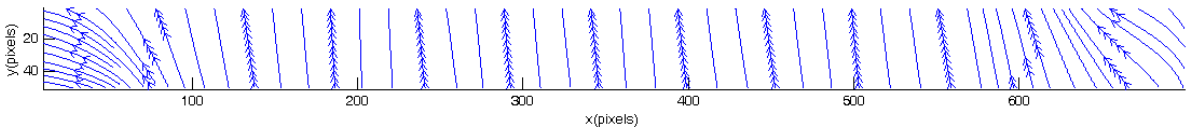

(e)

Figure 3.20. Perturbation streamlines at (a) B_{max} = 100G, (b) B_{max} = 300G, (c) B_{max} = 500G, (d) B_{max} = 700G, and (e) B_{max} = 900G in parallel configuration in a magnetic fluid.

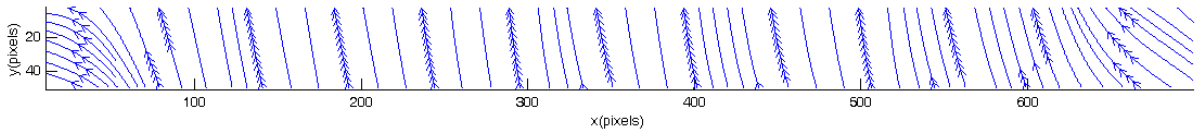

(a)

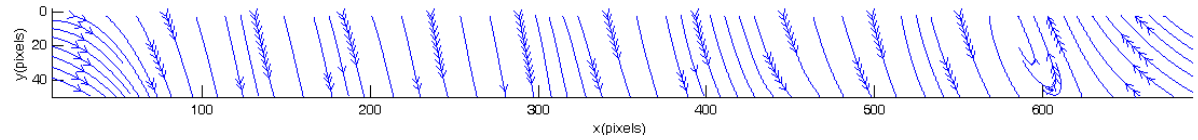

(b)

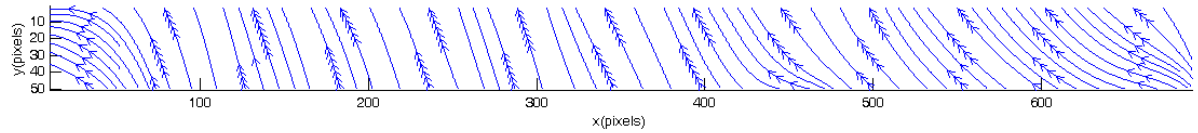

(c)

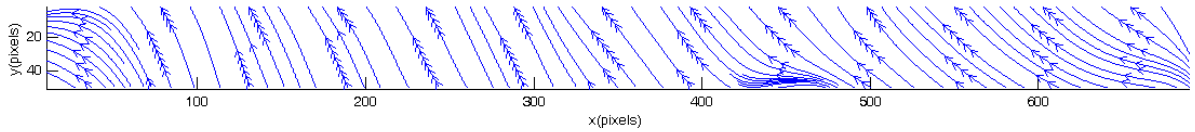

(d)

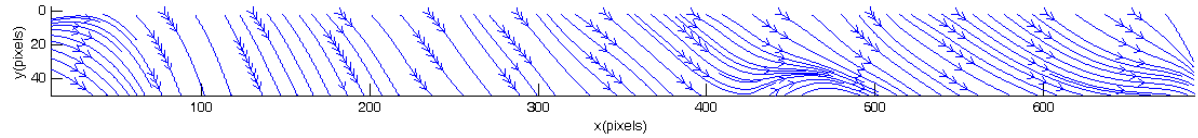

(e)

Figure 3.21. Perturbation streamlines at (a) B_{max} = 100G, (b) B_{max} = 300G, (c) B_{max} = 500G, (d) B_{max} = 700G, and (e) B_{max} = 900G in anti-parallel configuration in a magnetic fluid.

3.8 Velocity and streamline results in a magnetic fluid

The velocity field $\boldsymbol{u}$ in field is the superposition of base velocity field in zero field and perturbation velocity in corresponding field as it is showed in Eq. (3.3). Figure 3.22 and 3.23 show the velocity field at B_{max} = 0, 100G, 300G, 500G, 700G and 900G at 5s after the magnetic field is applied in two configurations. Figure 3.24 and 3.25 show the streamlines from these velocities. The velocity fields show the same change as perturbation velocity fields. The main horizontal direction of velocity is on up half cell (left to right) and low half cell (right to left). And the main vertical direction is at hot side (up) and cold side (down). The magnitude of perturbation velocities is small compared to the base velocities, so the flow pattern change in velocity fields is not very obvious in these plots. The streamlines show flow patterns in applied fields. We will discuss more pattern change with velocity magnitude and perturbation Q field in chapter 4. When the temperature gradient is anti-parallel to the field gradient, it shows the flow patterns are non-localized in low fields (B_{max} =100G); in high fields (B_{max} =300G to 900G), the convective motion seems to crossover from two-dimensional to three-dimensional flow, enhancing the thermal transfer across the sample. The crossover effect is stronger in higher field. For anti-parallel configuration, the streamlines indicate formation of local flow structures that could explain the slowing down of the heat transfer.

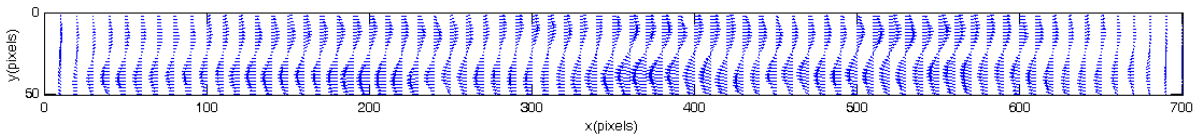

(a)

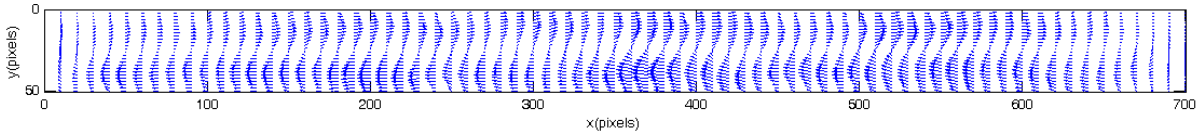

(b)

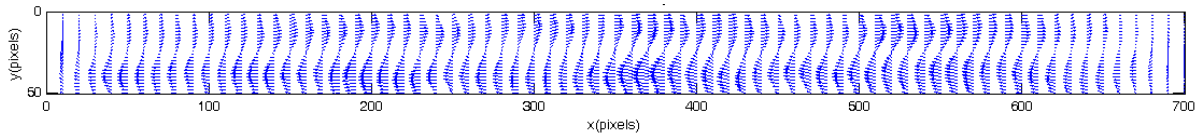

(c)

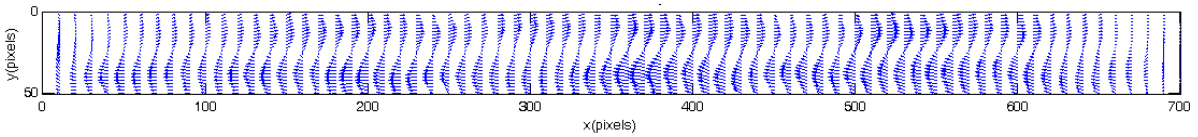

(d)

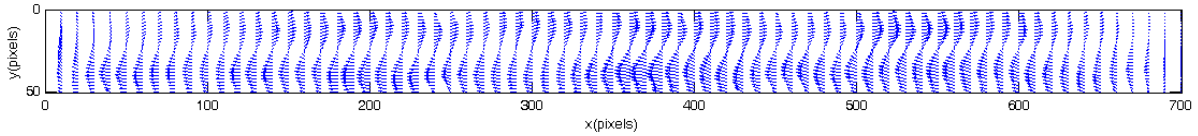

(e)

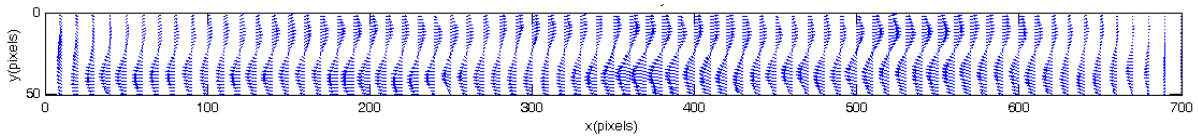

(f)

Figure 3.22. Velocity fields at (a) $B_{max} = 0$, (b) $B_{max} = 100G$, (c) $B_{max} = 300G$, (d) $B_{max} = 500G$, (e) $B_{max} = 700G$, and (f) $B_{max} = 900G$ in parallel configuration in a magnetic fluid.

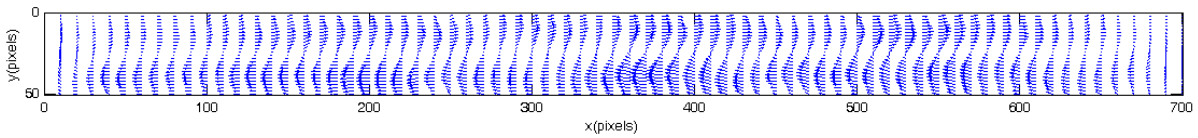

(a)

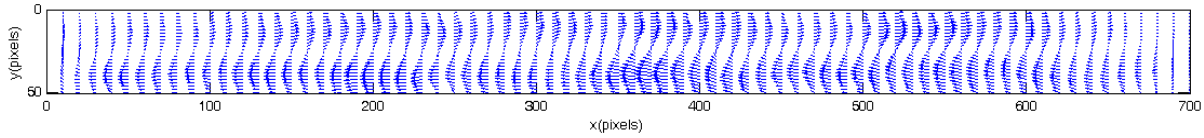

(b)

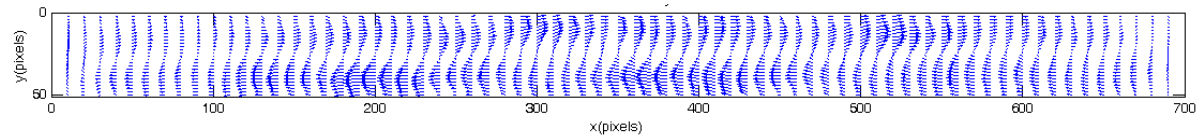

(c)

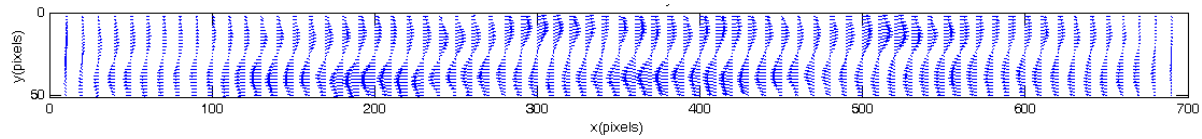

(d)

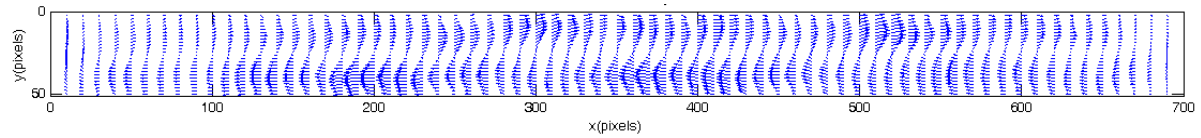

(e)

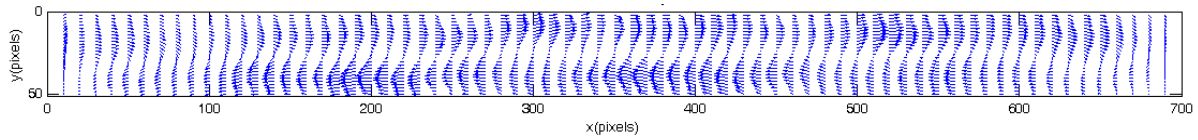

(f)

Figure 3.23. Velocity fields at (a) $B_{max} = 0$, (b) $B_{max} = 100G$, (c) $B_{max} = 300G$, (d) $B_{max} = 500G$, (e) $B_{max} = 700G$, and (f) $B_{max} = 900G$ in anti-parallel configuration in a magnetic fluid.

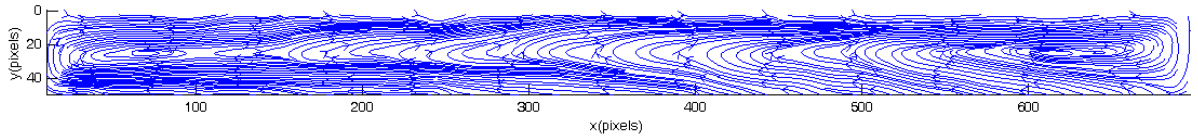

(a)

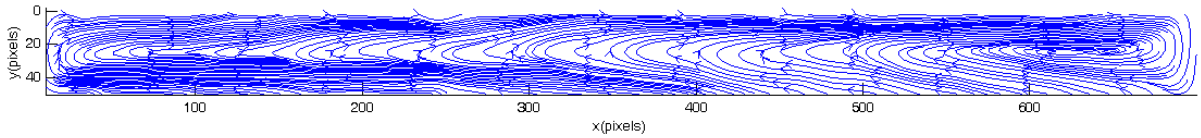

(b)

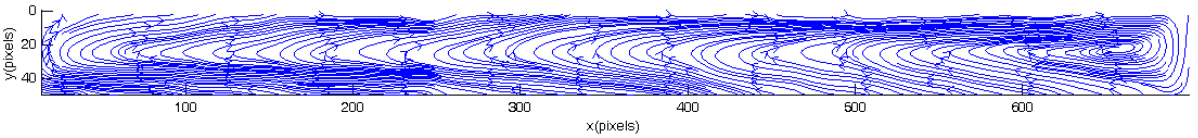

(c)

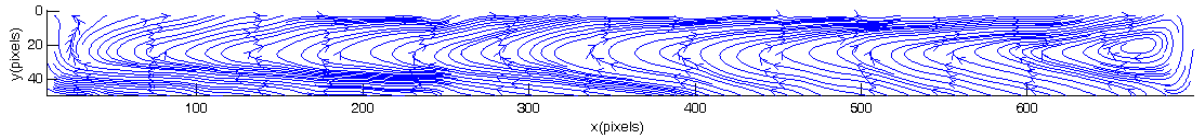

(d)

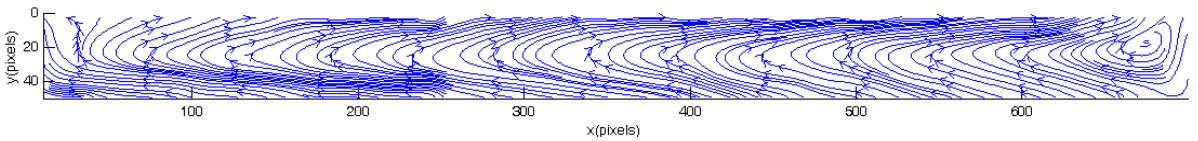

(e)

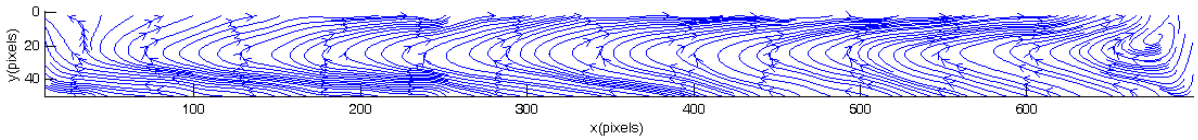

(f)

Figure 3.24. Streamlines at (a) $B_{max} = 0$, (b) $B_{max} = 100G$, (c) $B_{max} = 300G$, (d) $B_{max} = 500G$, (e) $B_{max} = 700G$, and (f) $B_{max} = 900G$ in parallel configuration in a magnetic fluid.

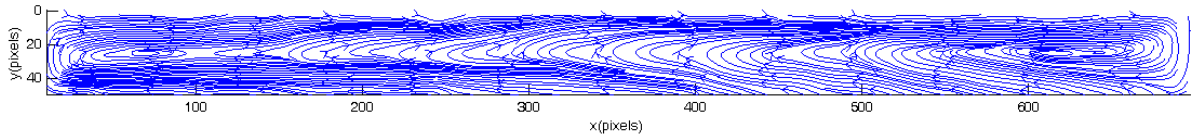

(a)

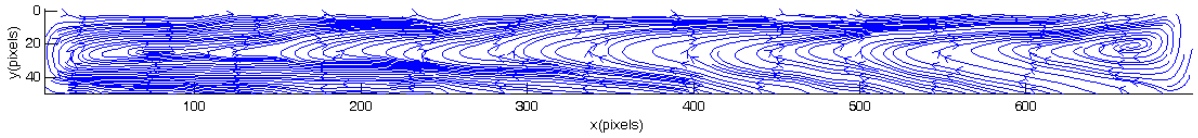

(b)

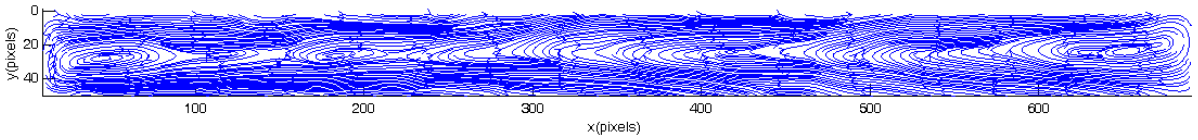

(c)

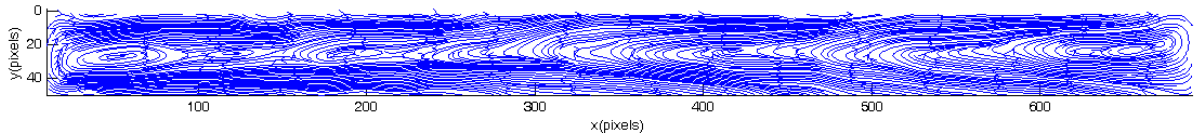

(d)

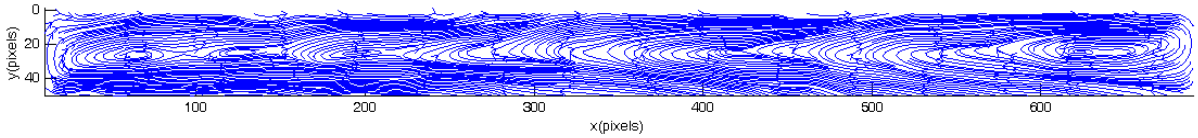

(e)

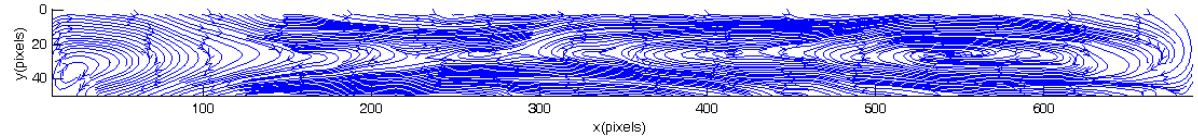

(f)

Figure 3.25. Streamlines at (a) $B_{max} = 0$, (b) $B_{max} = 100G$, (c) $B_{max} = 300G$, (d) $B_{max} = 500G$, (e) $B_{max} = 700G$, and (f) $B_{max} = 900G$ in anti-parallel configuration in a magnetic fluid.

CHAPTER 4: ANALYSES AND DISCUSSIONS

4.1 Determine the main heat transfer mechanism in a magnetic fluid

There are three heat transfer mechanisms in complex fluids in general: 1) thermal convection, 2) thermal conduction and 3) thermal diffusion. The convection flow patterns in fields have been shown in chapter 3.8. To determine the main heat transfer mechanism in our observations we would like to know how important the thermal conduction and thermal diffusion compare with thermal convection.

For thermal conduction, the differential thermal conduction equation is

$$\dot{q} = -k\nabla T \tag{4.1}$$

where $\dot{q}$ is the local heat flux(1996 W m^{-2}), k is the thermal conductivity (in unit W m^{-1} K^{-1}), and ∇T is the temperature gradient (in unit K m^{-1}). The heat flux input into our sample is from a plane heating source. In a short time after heating is applied, the temperatures change at thermocouples locations, for example LLB as shown in figure 4.1, is mainly due to conduction before convection well developed.

The hot plate technique can be used to measure the thermal conductivity to obtain the rate of thermal conduction [51 and 53]. The hot plate technique is applied in a transient state with a constant heat flux as a boundary condition as the case in our experiment. The temperature change at one position due to a sudden impact of a constant heat flux from a plate surface from thermal conduction is given by equation 4.2 [52 and 53]

$$\Delta T(x,t) = \frac{2\dot{q}\sqrt{t}}{\sqrt{k\rho c_p}}\left[\frac{1}{\sqrt{\pi}}e^{-\sigma^2} - \sigma\mathrm{erfc}(\sigma)\right] \quad (4.2)$$

$$\sigma = x\sqrt{\frac{\rho c_p}{4kt}} \quad (4.3)$$

$$\mathrm{erfc}(\sigma) = \frac{2}{\sqrt{\pi}}\int_{\sigma}^{\infty} e^{-t^2}dt \quad (4.4)$$

where ΔT is the temperature change at measuring location in short time t =10s [53], x is the distance between temperature detector and heating surface, $\dot{q}$ is the heat flux, ρ is density of the fluid, C_p is heat capacity, k is thermal conductivity. The equation 4.2 has to be solved iteratively. Figure 4.2 shows the relative thermal conductivity vs. fields. It is found that the thermal conductivity increase with fields.

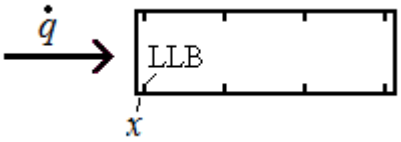

Figure 4.1. Hot plate technique in our sample cell

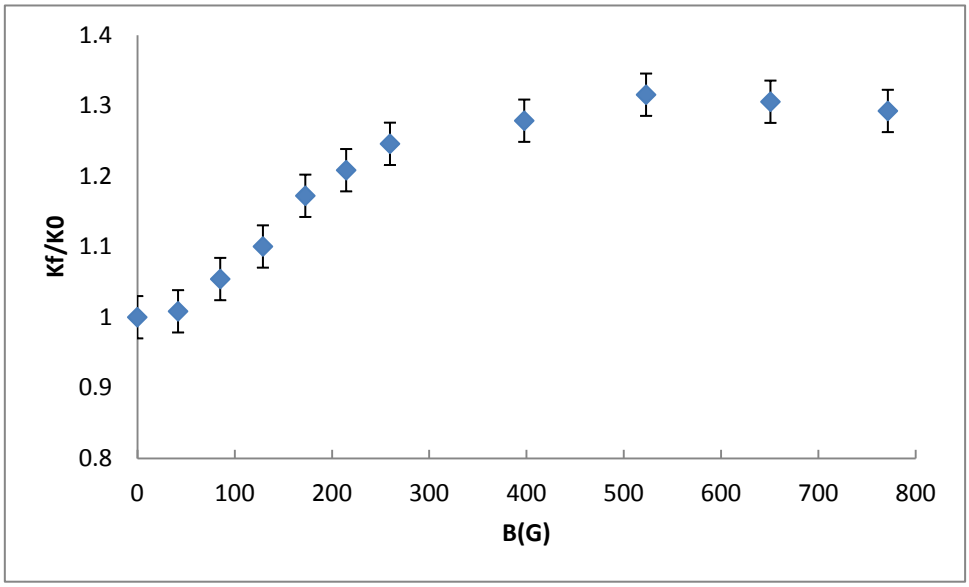

Figure 4.2. Relative thermal conductivity *vs.* local field in a magnetic fluid.

From the calculation of thermal conductivity, we know the conduction increases in magnetic fields. To identify the heat transfer ratio between thermal convection and conduction, the Nusselt number is calculated. Nusselt number is defined as the ratio of convective heat transfer to conductive heat transfer under the same conditions: [2]

$$Nu = \frac{hL}{k} \tag{4.5}$$

Where *h* is the convective heat transfer coefficient of the flow, *L* is the characteristic length, *k* is the thermal conductivity of the fluid. Nu is a dimensionless number. If a Nusselt number is close to one, it means that convection and conduction have similar magnitude. A large Nusselt number is corresponding to a more dynamic convection. The convective heat transfer coefficient is present in following equation:[2]

$$h = \frac{\dot{q}}{\Delta T} \tag{4.6}$$

Where $\dot{q}$ is heat flux, ΔT is the temperature difference between wall and fluid. We used the temperature difference measured by TSP in our experiment. From equation 4.2-4.6, the Nusselt numbers in step fields are shown in table 4.1 and figure 4.3.

From table 4.1, the range of Nusselt number is from 4.8-9.1, so the heat transfer through convection is larger than that of conduction. In parallel configuration, the convective heat transfer coefficients increase, the Nusselt number increases corresponding to the increased convection ratio, the higher the field the larger the Nusselt number. The convective heat transfer coefficients and Nusselt number are decreased with the fields in anti-parallel configuration, which means heat transfer through conduction increases, but the

convection is still primary heat transfer from the Nusselt number in anti- configuration. The applied field increases the convection heat transfer in parallel configuration and reduces it in anti-parallel configuration.

Table 4.1. Nusselt numbers in a magnetic fluid in step fields.

Nu Parallel configuration	Heat transfer coefficient Parallel W/(m^2.K)	Field (G)	Heat transfer coefficient Anti-parallel W/(m^2.K)	Nu Anti-parallel configuration
6.6	131.3	0	132.1	6.6
6.6	132.1	100	128.7	6.4
6.7	134.8	200	121.7	6.0
6.8	136.7	300	116.7	5.8
6.9	139.5	400	113.4	5.6
7.3	147.8	500	110.8	5.5
7.6	152.3	600	107.8	5.3
8.0	160.9	700	106.7	5.3
8.6	172.0	800	105.0	5.2
9.0	181.4	900	100.3	5.0
9.1	183.1	1000	96.4	4.8

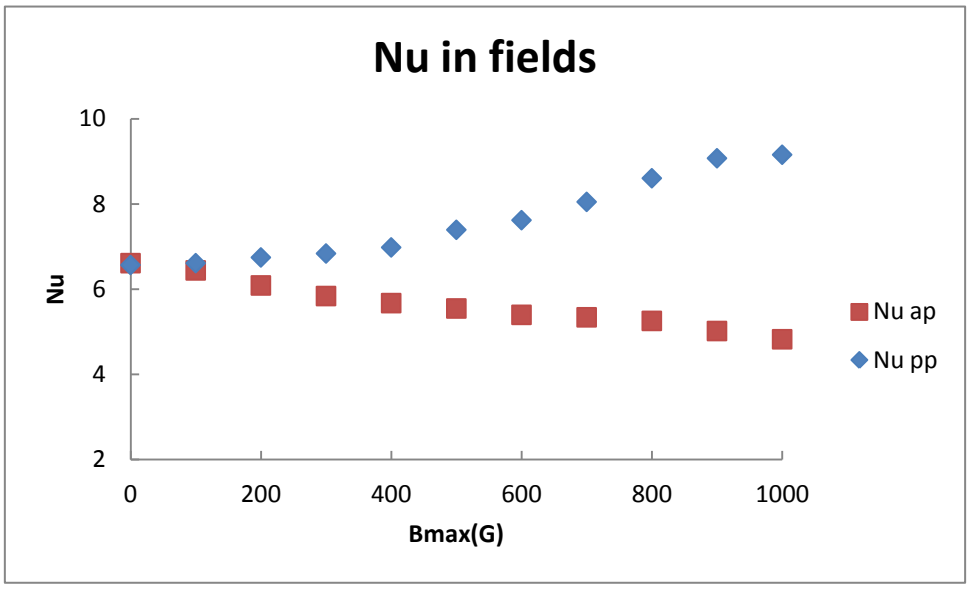

Figure 4.3. Nusselt number in applied fields in two configurations

Thermodiffusion is also called Soret effect. It is a phenomenon observed in a complex fluid where a mass flow is induced by a temperature gradient. The fluid is at least binary [54-56]. Thermodiffuison can be positive or negative. If the particles move from a hot region to a cold region, it is positive, and it is negative when reversal particle movement happens.

To compare the effect of thermal diffusion on heat transfer to that of convection, the time scale based approach leads to an effective criterion. The different heat transfer process is characterized by its own time scale.

The convective time scale τ_c can be obtained as:[57]

$$\tau_c = \frac{L}{v} \tag{4.7}$$

Here, τ_c is the time to travel through the distance L with the convective velocity v.

The time scale for diffusion can be got from [57]

$$\frac{\partial \emptyset}{\partial t} = D \frac{\partial^2 \emptyset}{\partial x^2} \tag{4.8}$$

where D is the diffusion coefficient for mass diffusion or the thermal diffusivity for thermal diffusion. In a scale sense, if $\Delta t \sim \tau_d$ and $\Delta x \sim L$, the diffusive time scale τ_d can be found as [57-59]

$$\tau_d = \frac{L^2}{D} \tag{4.9}$$

The meaning of τ_d is the time need to travel diffusively through the distance L across the temperature gradient.

In our experiment, L is $9*10^{-2}$ m, v is $5*10^{-4}$ m/s at steady state, mass diffusion coefficient D_m is $1*10^{-11}$ m^2/s in zero field [60 and 61], and thermal diffusivity D_t is $3.7*10^{-8}$

m^2/s in zero field [58]. So τ_c is $1.8*10^2$ s, τ_{dm} is $8.1*10^8$ s and τ_{dt} is $2.2*10^5$ s. When a field applied, the maximum change of velocity and thermal diffusivity [62] is 20% of its zero-field values, so the convective time scale and thermal diffusion time scale are same order of magnitude as its zero-field values. The mass diffusion time scale and thermal diffusion time scale are much larger than convective time scale both in zero field and applied fields.

From the calculation of Nusselt number and diffusion time scale, we can say even three heat transfer mechanisms exist in our experiment, thermal convection is the primary thermal transfer method in our experimental time scale.

4.2 Convective flow front velocity vs. fields in a magnetic fluid

Now we know the convection is primary heat transfer process in our experiments. To analysis how the convection change with field, convective flow front velocity change in applied field is calculated. The convective flow front is the front of the flow when the convections start. We define the average convective flow front velocity

$$v = \Delta L / \Delta t \tag{4.10}$$

Where v is the average velocity of convective flow front and ΔL is the distance traveled by convective flow front from one thermocouple to the neighboring one, for example, from LLT to LM1T or LRB to LM2B. Δt is the time needed to travel in the distance ΔL. ΔL and Δt are indicated in Figure 4.3. When the flow front reaches the thermocouple, the temperature at this thermocouple will change rapidly, the time difference of temperature change between LLT and LM1T (LRB and LM2B) is Δt as shown in figure 4.4.

By this way, 4 different average convective flow front velocities are calculated in two sample cells. In each cell we choose two flow front velocities to compare with, one is on the hot side, and the other is on the cold side. Each convective flow front is labeled in figure 4.5. For example, LHV means left sample cell hot side flow front, etc.

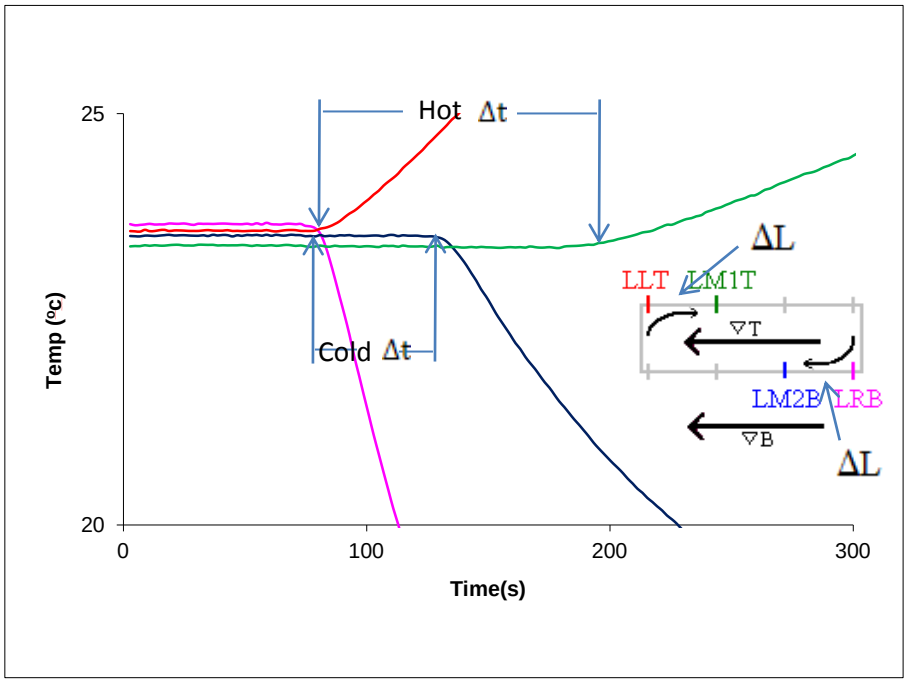

Figure 4.4. ΔL and Δt in flow front velocity definition.

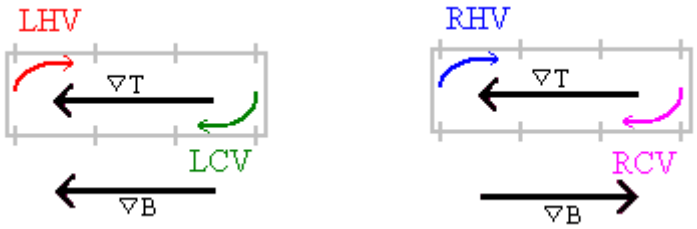

Figure 4.5. Average convective flow fronts in sample cells.

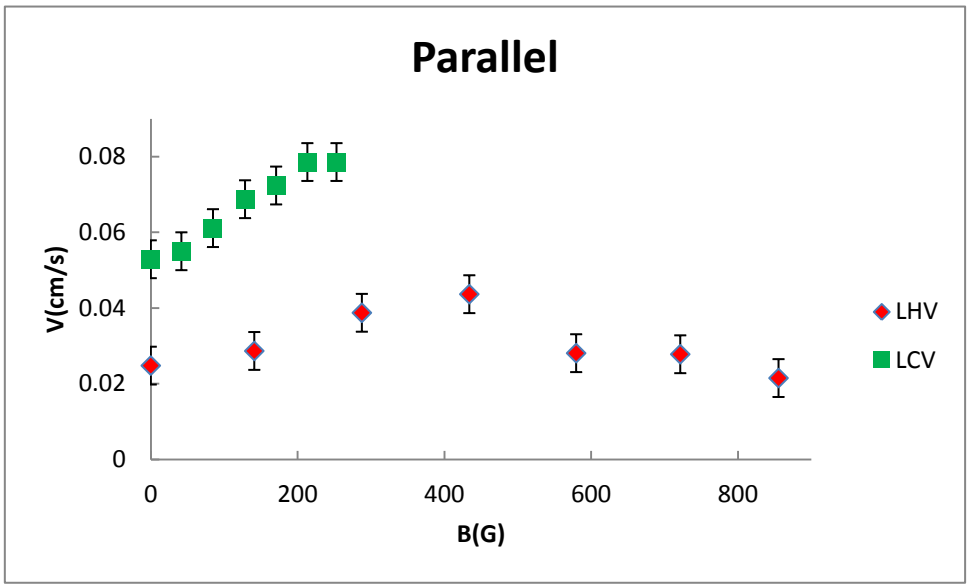

(a)

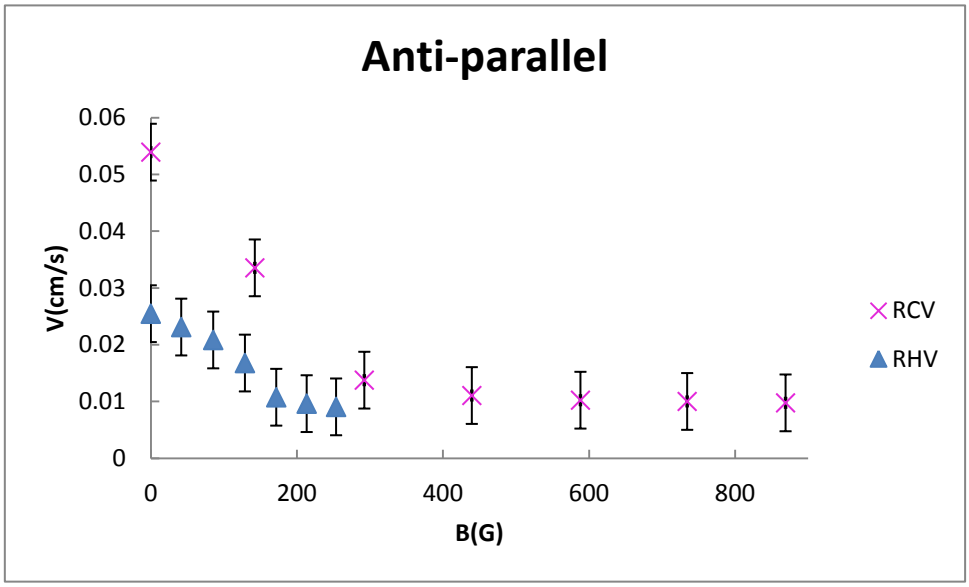

(b)

Figure 4.6. Average velocities of convective flow fronts in different magnetic fields in (a) parallel, and (b) anti-parallel configuration in a magnetic fluid.

Figure 4.6a shows average flow front velocities in different fields in magnetic fluid in parallel configuration and Figure 4.6b shows velocities in anti-parallel configurations in local fields. In parallel configuration, when we increase the magnetic field, the average convective flow front velocities LCV (green square) and LHV (red diamond) are increased; then LHV decreases after $B \geq 400G$. The reason is that the fields have changed the fluid structure as shown in chapter 3.8 that the convective flow crossover from 2D to 3D in parallel configuration.

For anti-parallel configuration, when we increase magnetic field, the average convective flow front velocities RCV (pink cross) and RHV (blue triangle) decrease with the applied field, and RCV saturate after $B \geq 400G$.

From flow front velocity change in applied field, the magnetic fields increase the convective velocity to speed up the convective heat transfer in parallel configuration; and inhabit it by decreasing the velocity in anti-parallel configuration.

4.3 Velocity magnitude in a magnetic fluid

The velocity magnitude fields show the field effect in velocity magnitude, which are give complete velocity change in applied fields in our sample cells. Figure 4.7 and figure 4.8 show horizontal component, vertical component and total velocity magnitude fields at B_{max} = 0, 100G, 300G, 500G, 700G and 900G at 5s after the magnetic field is applied in two configurations. The horizontal velocity component is mainly at upper and lower half of cell, the average horizontal velocity at upper and lower half of cell is $2.5*10^{-4}$ m/s. The vertical velocity component is mainly non zero at two ends, the average vertical velocity is $2.0*10^{-4}$ m/s. The total average velocity along the convection roll is $2.6*10^{-4}$ m/s. In parallel configuration (figure 4.7), both horizontal and vertical velocities increase in fields, especially at left side close to the magnet pole. While in anti-parallel configuration (figure 4.8), most part of velocity fields is same in applied fields. But in some locations, both horizontal and vertical components of velocity increase in the field, especially close to cold side where the field and field gradient is high. For example, at B_{max}=900G, the average velocities at one layer increase more than $1.0*10^{-4}$ m/s at x=8.3cm (650 pixel) from left side in figure 4.6c. The local velocity changes between 7.1 cm (550 pixel) and 8.3 cm (650 pixel) are corresponding to the flow pattern change as the streamlines shows in figure 3.25f. The velocities at different applied fields are increased in parallel configuration indicates that the convective heat transfer increase. In anti-parallel configuration, while the change of velocity fields in specific location is consistent with the flow pattern change in streamlines (chapter

3.8) and perturbation Q field (chapter 4.4), so the change of flow pattern can reduce the convective heat transfer.

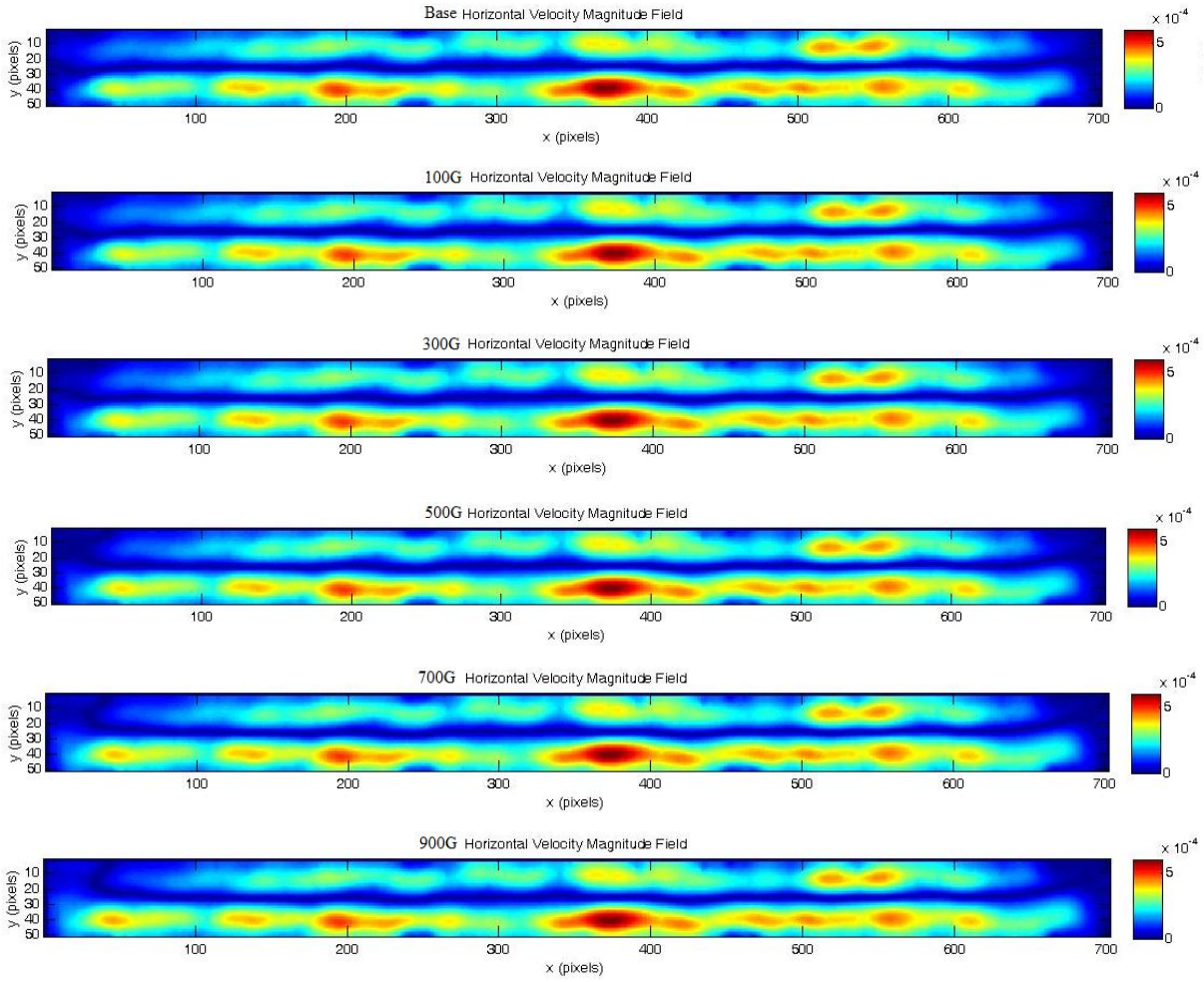
Base Horizontal Velocity Magnitude Field
100G Horizontal Velocity Magnitude Field
300G Horizontal Velocity Magnitude Field
500G Horizontal Velocity Magnitude Field
700G Horizontal Velocity Magnitude Field
900G Horizontal Velocity Magnitude Field
y (pixels)
x (pixels)
x 10^-4

(a)

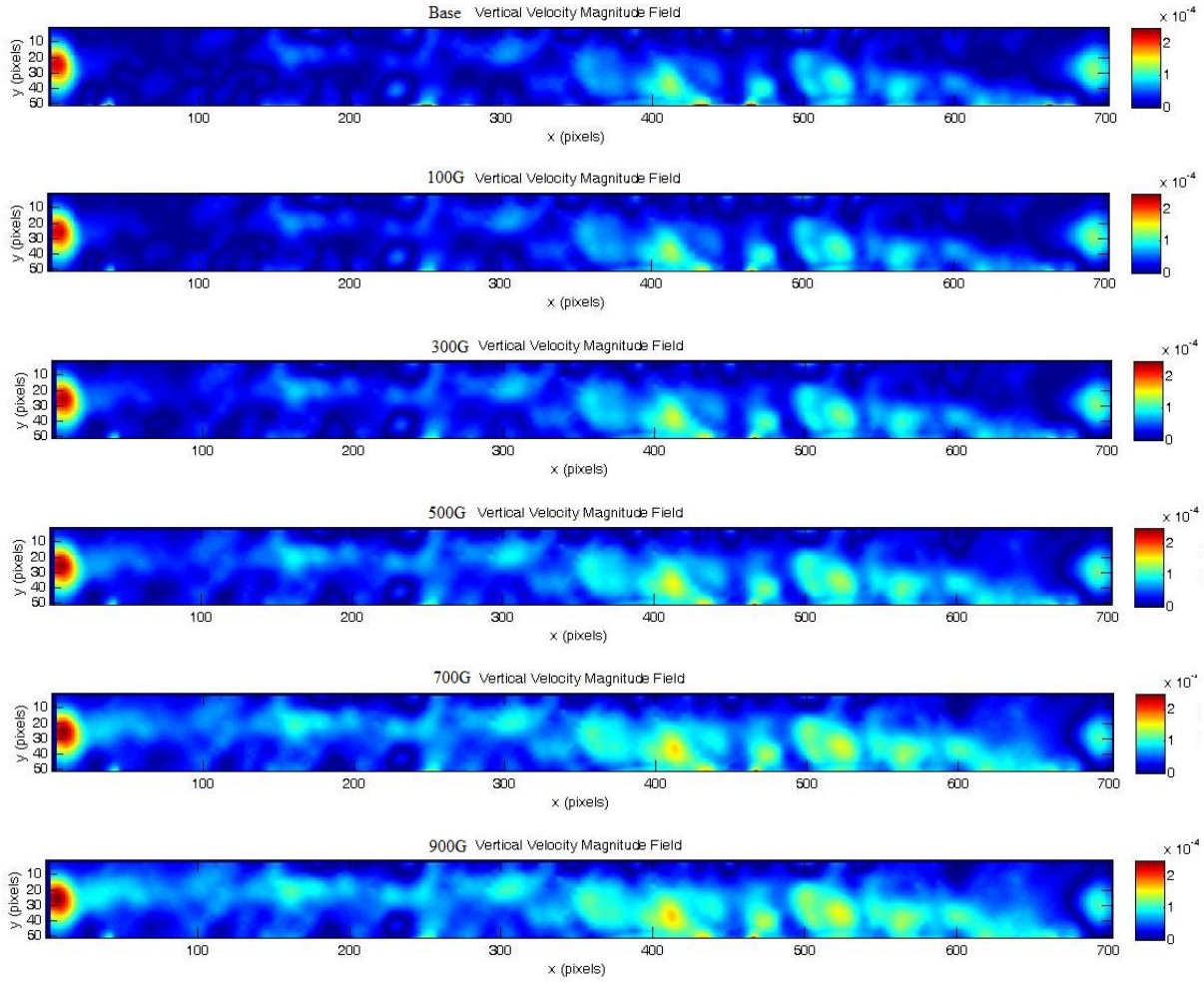
Base Vertical Velocity Magnitude Field
100G Vertical Velocity Magnitude Field
300G Vertical Velocity Magnitude Field
500G Vertical Velocity Magnitude Field
700G Vertical Velocity Magnitude Field
900G Vertical Velocity Magnitude Field
y (pixels)
x (pixels)
x 10^-4

(b)

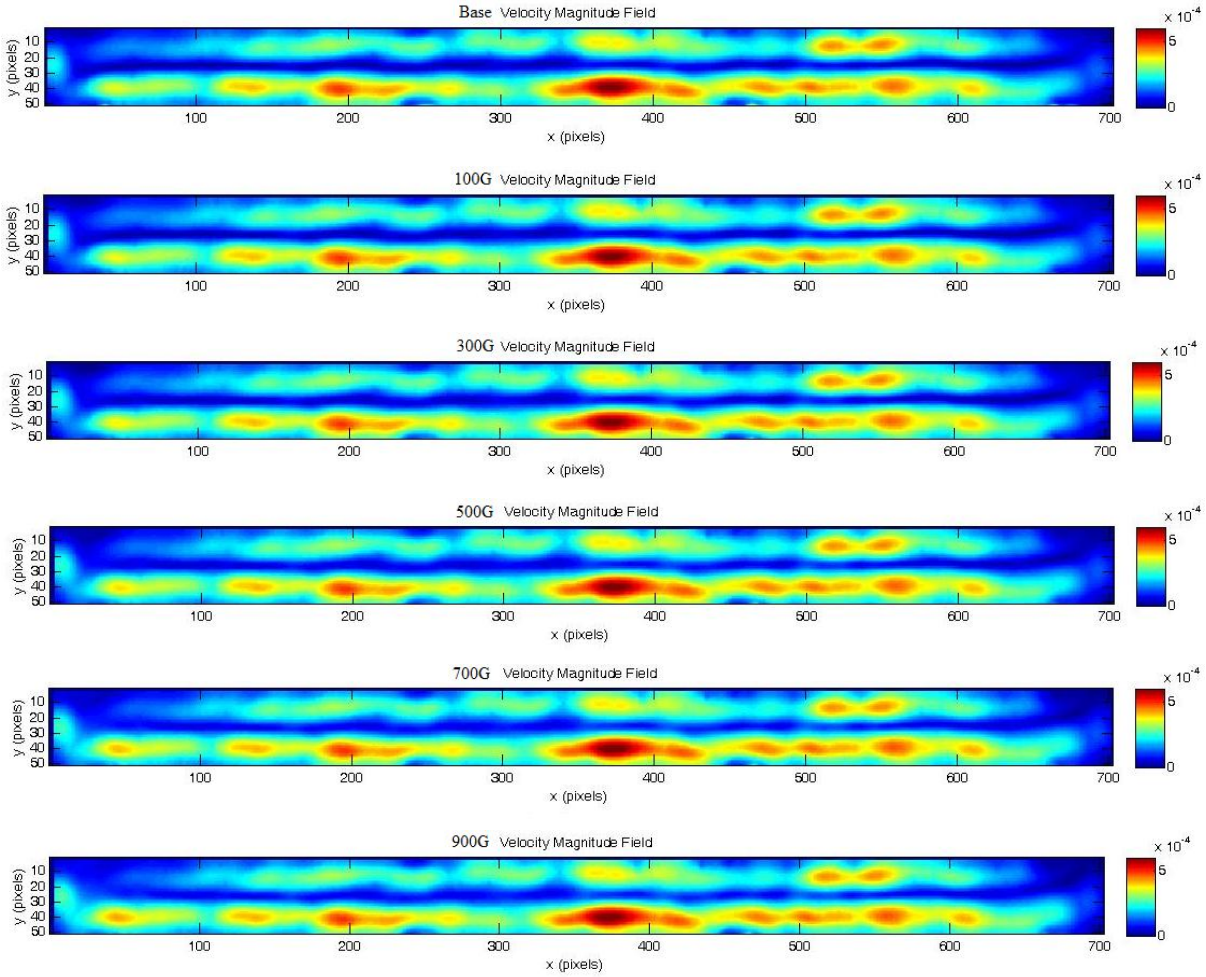

(c)

Figure 4.7. (a) Horizontal velocity magnitude fields (b) vertical velocity magnitude fields, and (c) total velocity fields in parallel configuration in a magnetic fluid.

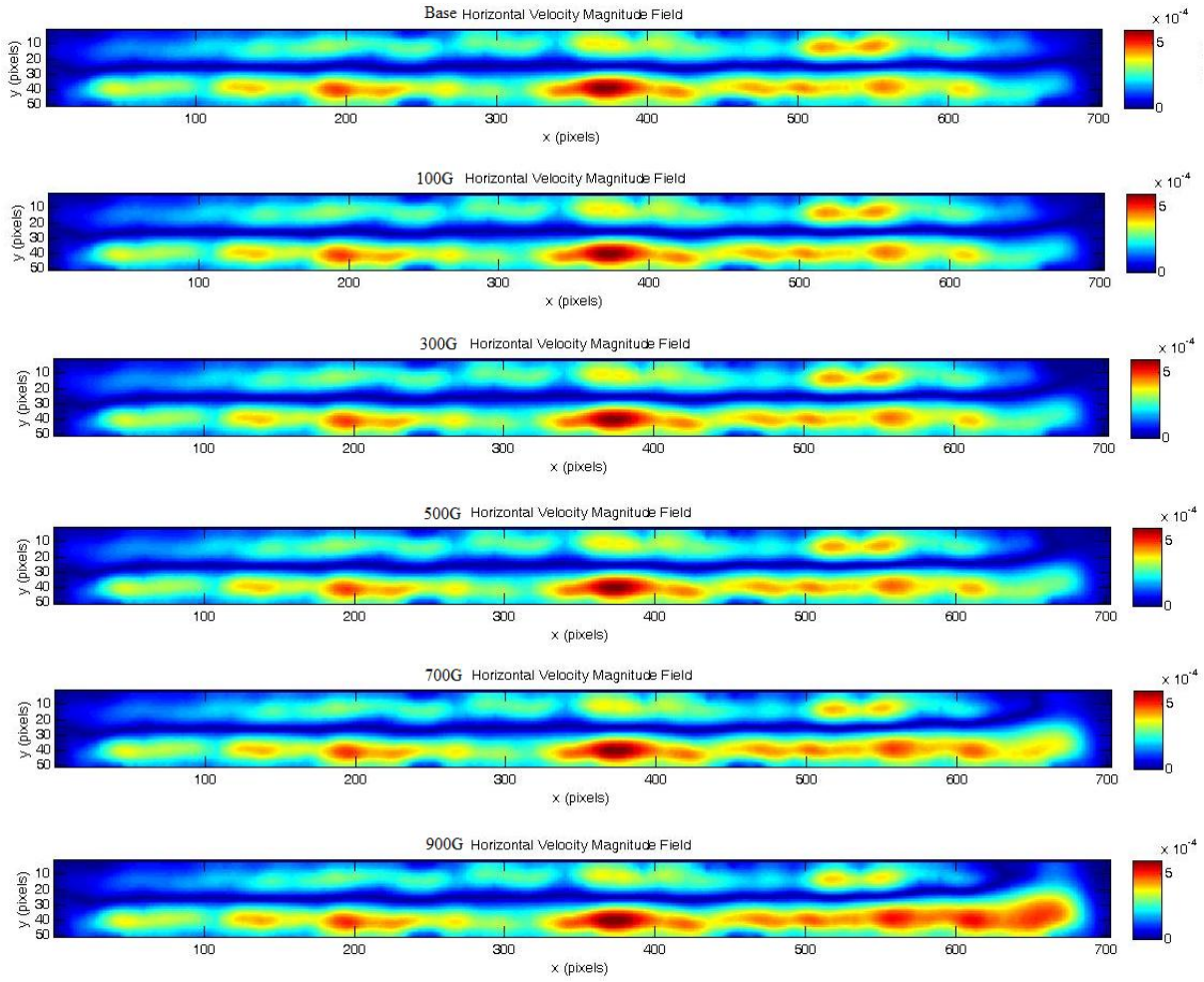
Base Horizontal Velocity Magnitude Field
100G Horizontal Velocity Magnitude Field
300G Horizontal Velocity Magnitude Field
500G Horizontal Velocity Magnitude Field
700G Horizontal Velocity Magnitude Field
900G Horizontal Velocity Magnitude Field
y (pixels)
x (pixels)
x 10^-4

(a)

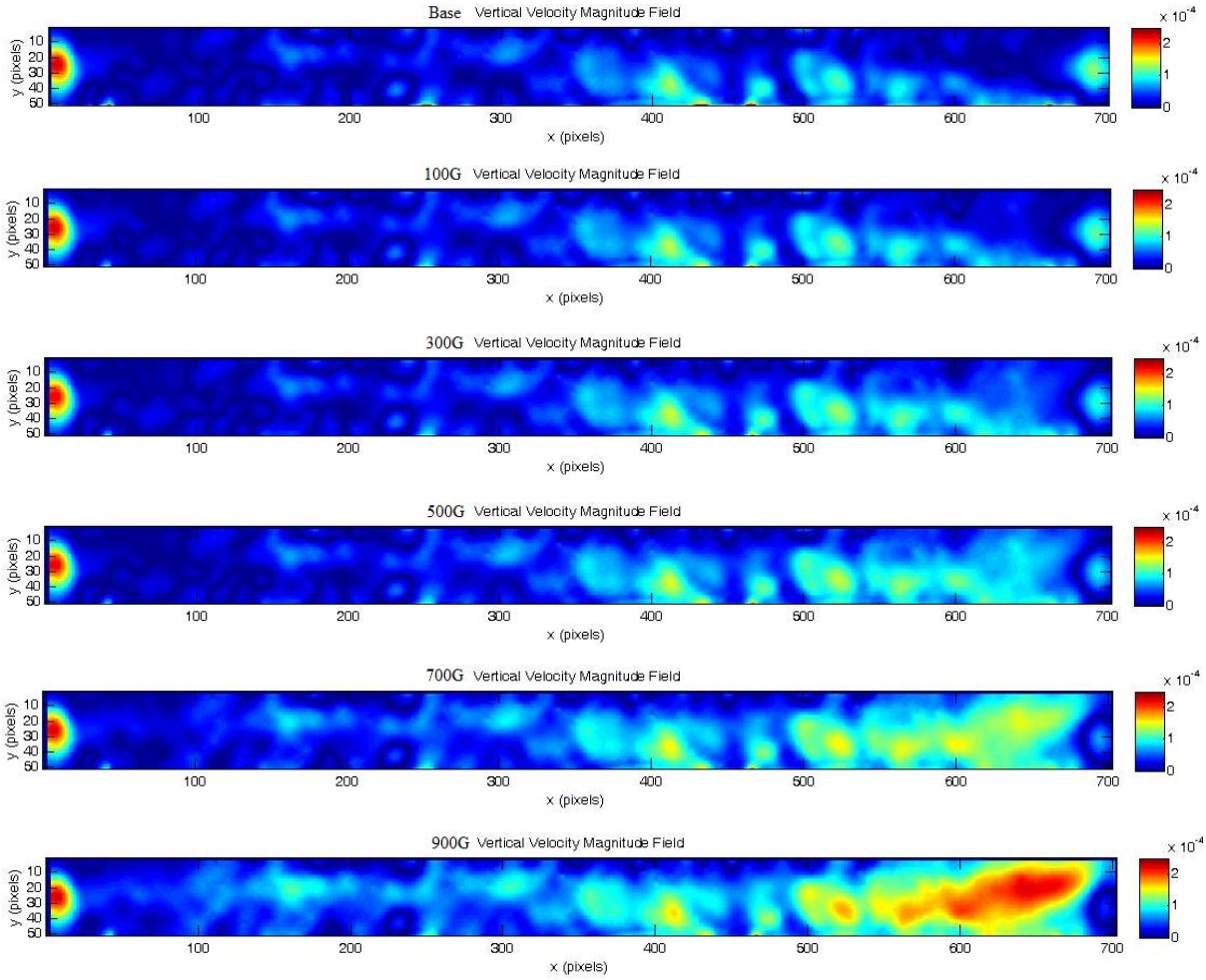
Base Vertical Velocity Magnitude Field
100G Vertical Velocity Magnitude Field
300G Vertical Velocity Magnitude Field
500G Vertical Velocity Magnitude Field
700G Vertical Velocity Magnitude Field
900G Vertical Velocity Magnitude Field
y (pixels)
x (pixels)
x 10^-4

(b)

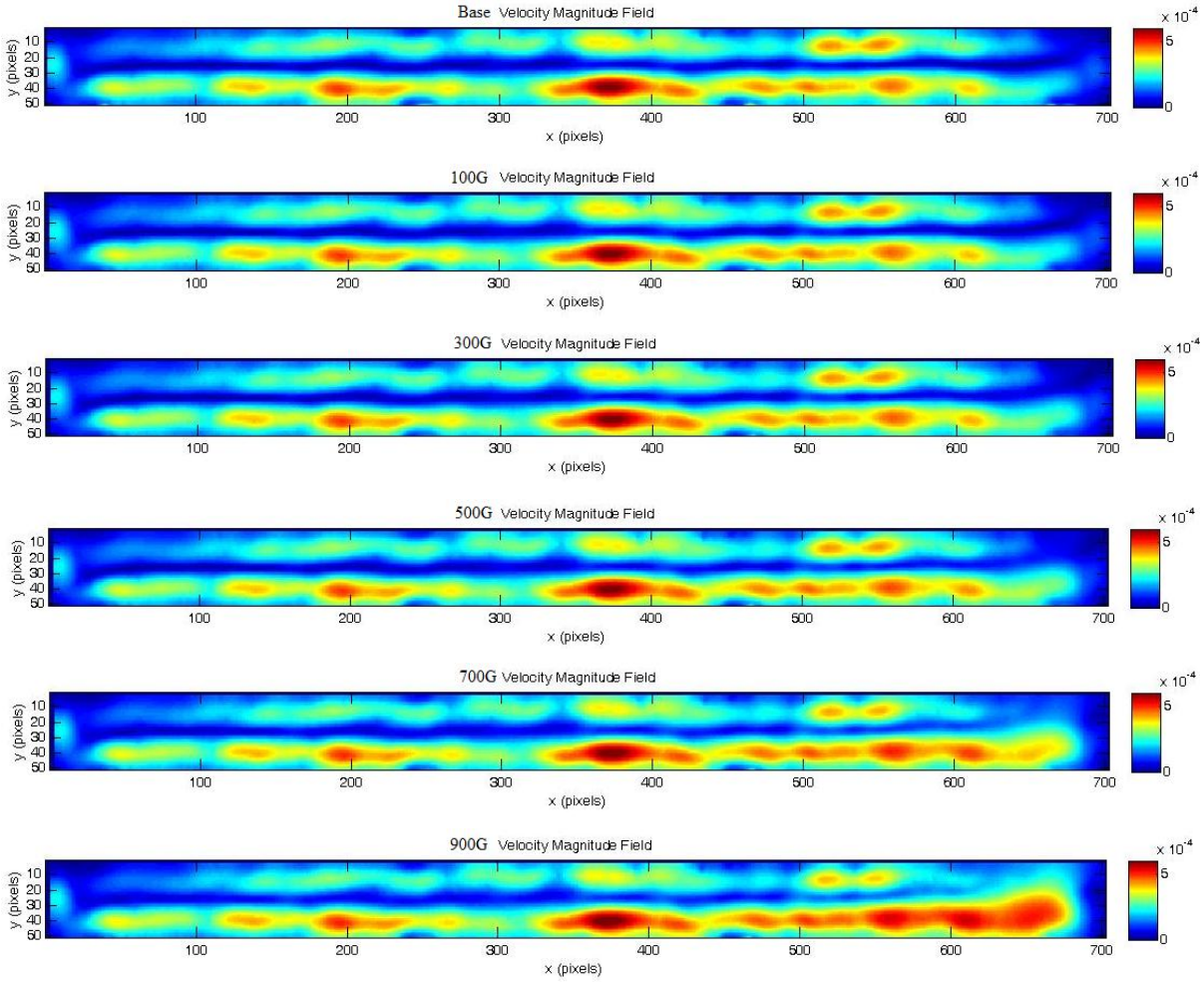

(c)

Figure 4.8. (a) Horizontal velocity magnitude fields (b) vertical velocity magnitude fields, and (c) total velocity fields in anti-parallel configuration in a magnetic fluid.

4.4 Vorticity and Q field in a magnetic fluid

Streamline and velocity field show the main flow pattern in figure 3.22-3.25. Vorticity and Q field can indicate the convection roll and vortex in the fluid. The vorticity ω is defined as the curl (rotational) of the flow velocity vector. In our sample cell geometry

$$\omega = \partial v / \partial x - \partial u / \partial y \tag{4.11}$$

where (x, y) are, respectively, the coordinates in a local 2D Cartesian coordinate and (u, v) are the corresponding velocity components.

The second invariant Q of the velocity gradient tensor $\nabla \boldsymbol{u} = \partial u_i / \partial x_j$ is defined as

$$Q = \left(\|\boldsymbol{\Omega}\|^2 - \|\boldsymbol{S}\|^2 \right) / 2 \tag{4.12}$$

where $\|\boldsymbol{S}\|^2 = tr\left(\boldsymbol{S}\,\boldsymbol{S}^T\right)$ and $\|\boldsymbol{\Omega}\|^2 = tr\left(\boldsymbol{\Omega}\,\boldsymbol{\Omega}^T\right)$, $\boldsymbol{S}$ and $\boldsymbol{\Omega}$ are the symmetric and anti-symmetric components of $\nabla \boldsymbol{u}$, i.e., $S_{ij} = \left(\partial u_i / \partial x_j + \partial u_j / \partial x_i\right) / 2$ and $\Omega_{ij} = \left(\partial u_i / \partial x_j - \partial u_j / \partial x_i\right) / 2$. $\boldsymbol{S}^T$ and $\boldsymbol{\Omega}^T$ are corresponding transpose. $\boldsymbol{S}$ is the rate-of-strain tensor, $\boldsymbol{\Omega}$ is the vorticity tensor. Hunt, Wray & Moin [63] defined a 'vortex' as a region with the positive second invariant Q.

Figure 4.9 shows the vorticity fields in zero field and in 900G for both configuration. Because of the shear layer in the middle of cells as we see in the velocity field and streamline in chapter 3.8, base on the definition of vorticity, the vorticity has large magnitude at where there is large velocity gradient. Also the perturbation velocity is small compared to base velocity, so with the large vorticity at shear layer in total velocity field, it is difficult to identify the vorticity due to vortex in vorticity field as it is in figure 4.9. The average vorticity

at shear layer is 0.1 s^{-1}. Figure 4.10 and 4.11 show the perturbation vorticity fields in applied fields in two configurations. The perturbation vorticity is the vorticity change after apply magnetic fields, for example, $\Delta\omega_{B=500G} = \omega_{B=500G} - \omega_{B=400G}$. We found the main vorticity change at two ends, the higher the field, the bigger the change. Figure 4.12 shows Q field in zero applied field and in 900G for both configuration. It is also difficult to find vortex change due to relative small perturbation velocity. Figure 4.13 and 4.14 show the perturbation Q fields in applied fields in two configurations. The perturbation Q (ΔQ) is the change of Q after the field is applied, for example, $\Delta Q_{B=500G} = Q_{B=500G} - Q_{B=400G}$. First, ΔQ is higher at high field at two ends in both configurations. In parallel configuration (figure 4.13), the perturbation Q field mainly is a single roll which corresponding to the flow pattern in chapter 3.8. That means change of vortex is consistent with the single overall convection roll in the zero field, so the main flow pattern is same. In anti-parallel configuration (figure 4.14), the main perturbation Q field changes only happen at two sides separately, which indicates local vortex formation, which are corresponding to the pattern changes in the streamline and velocity as shown in figure 3.25. The higher field the higher Q field change.

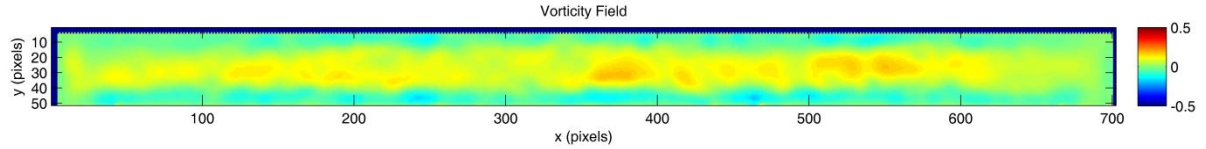

(a)

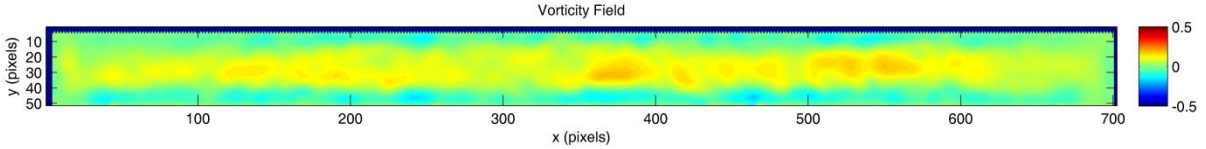

(b)

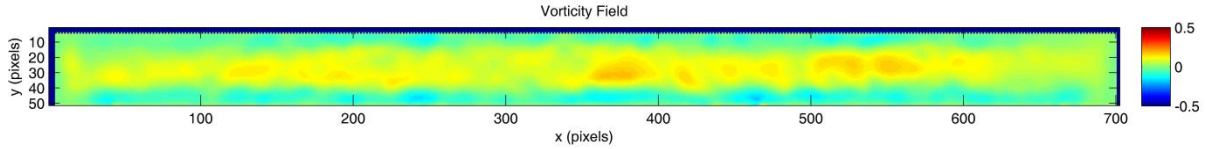

(c)

Figure 4.9. Vorticity at (a) B_{max}= 0 , (b) B_{max}= 900 in parall configuration, and (c) at B_{max}=900G in anti-parallel configuration in a magnetic fluid.

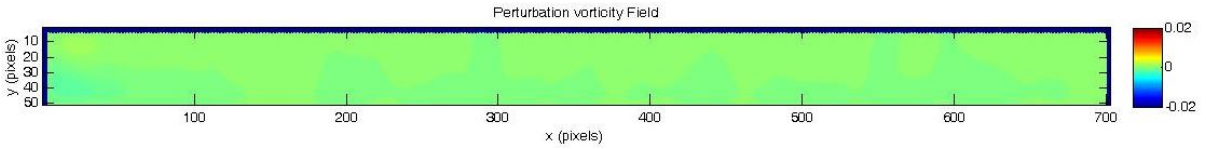

(a)

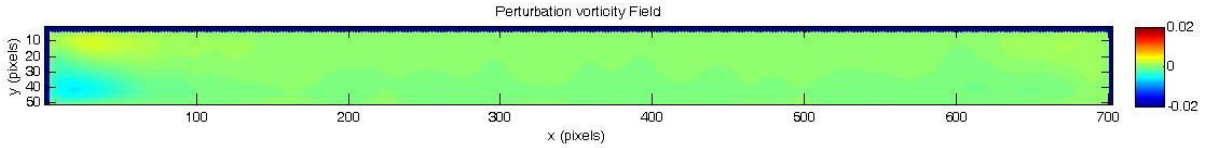

(b)

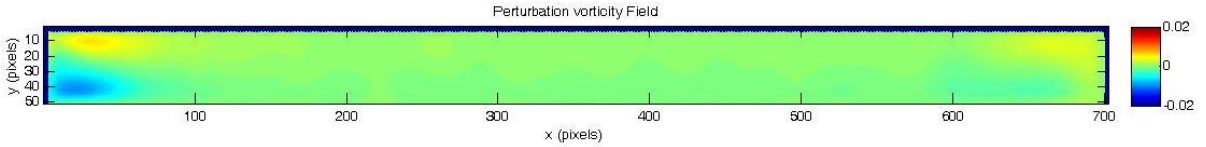

(c)

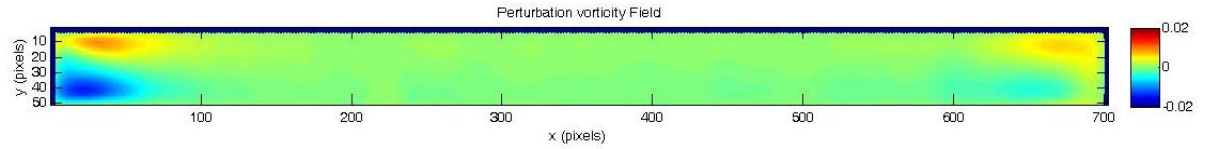

(d)

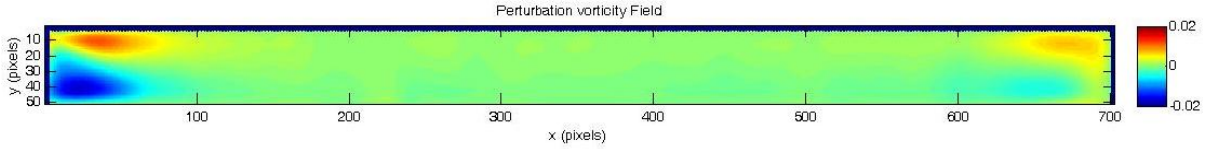

(e)

Figure 4.10 Perturbation vorticity at B_{max}= (a) 100G , (b) 300G (c) 500G (d) 700G, and (e) 900G in parallel configuration in a magnetic fluid.

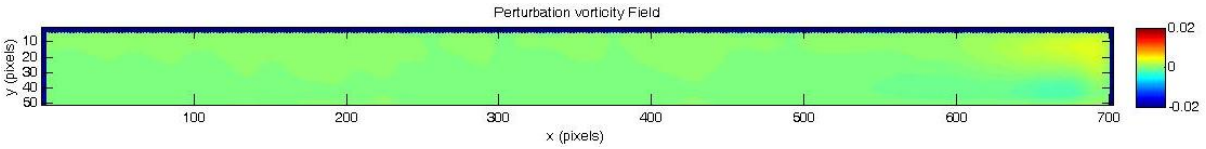

(a)

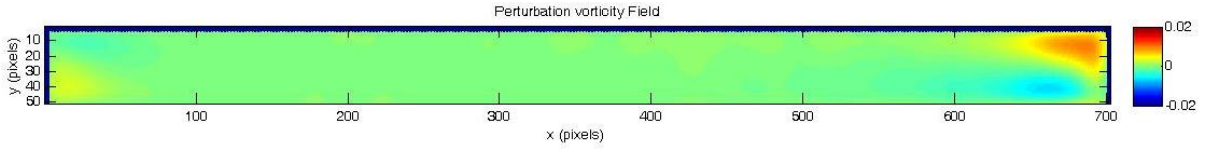

(b)

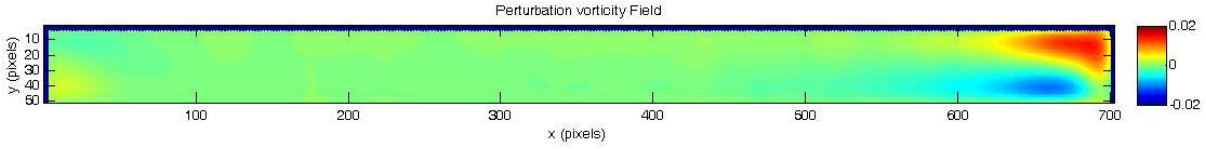

(c)

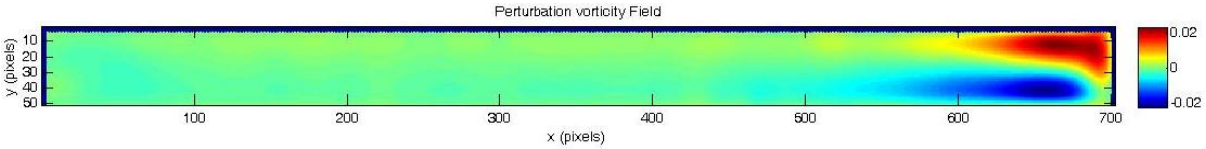

(d)

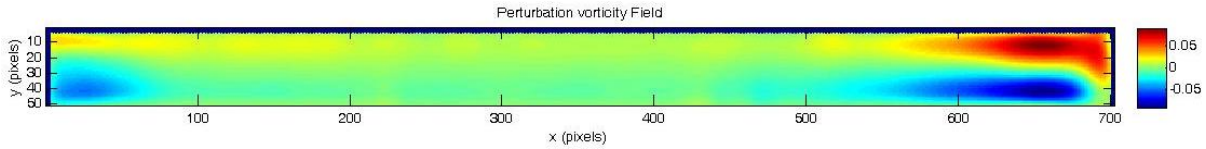

(e)

Figure 4.11. Perturbation vorticity at B_{max}= (a) 100G , (b) 300G (c) 500G (d) 700G, and (e) 900G in anti-parallel configuration in a magnetic fluid.

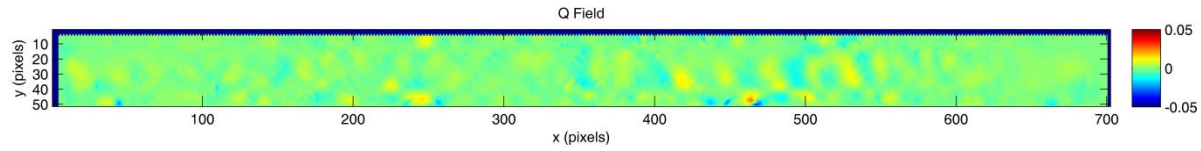

(a)

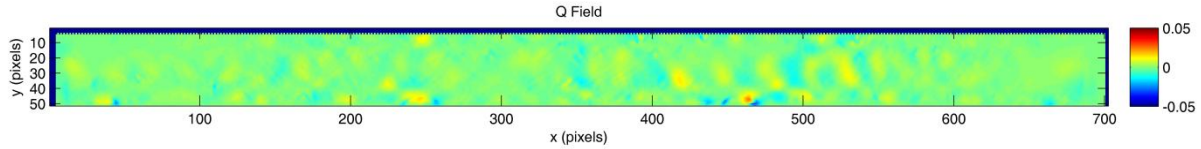

(b)

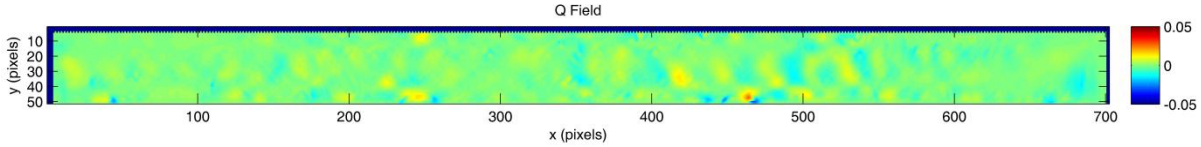

(c)

Figure 4.12. Q field at (a) B_{max}= 0 , (b) B_{max}= 900 in parall configuration, and (c) at B_{max}=900G in anti-parallel configuration in a magnetic fluid.

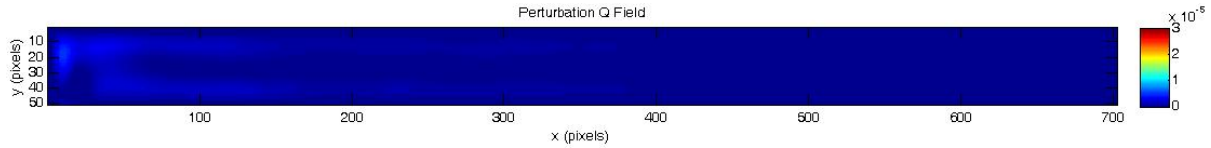

(a)

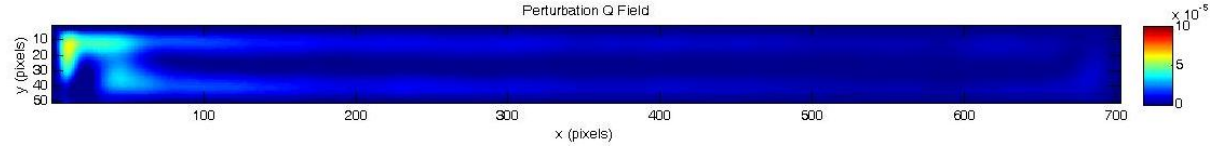

(b)

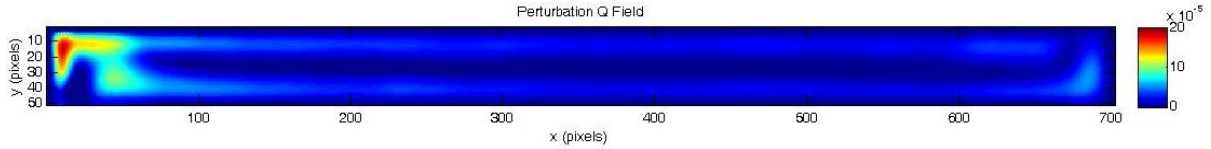

(c)

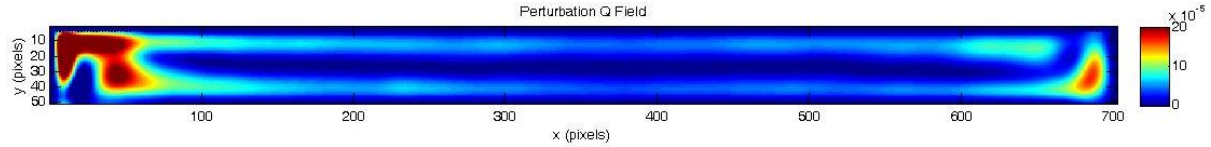

(d)

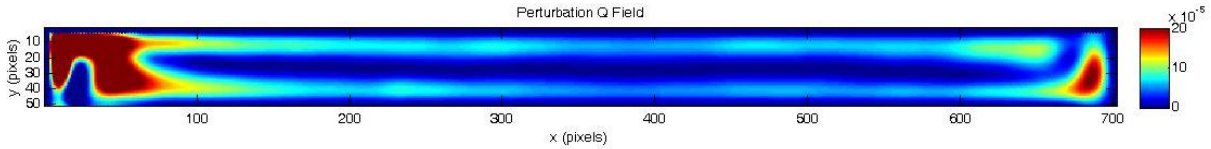

(e)

Figure 4.13. Perturbation Q field at B_{max}= (a) 100G , (b) 300G (c) 500G (d) 700G, and (e) 900G in parallel configuration in a magnetic fluid.

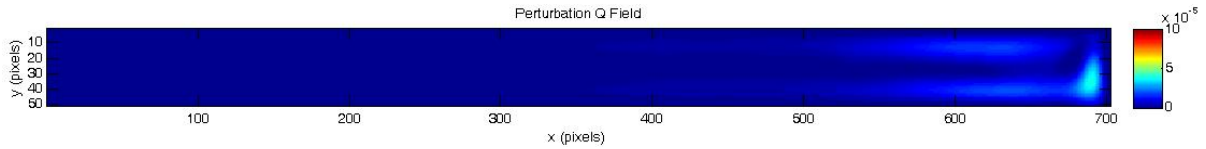

(a)

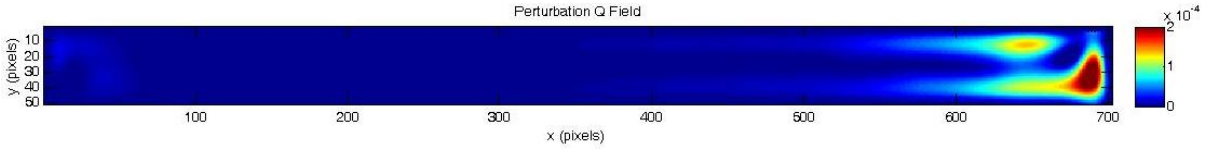

(b)

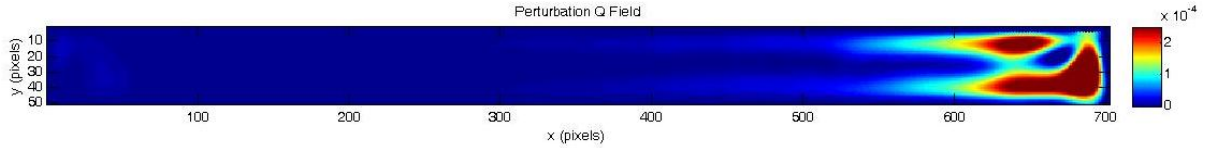

(c)

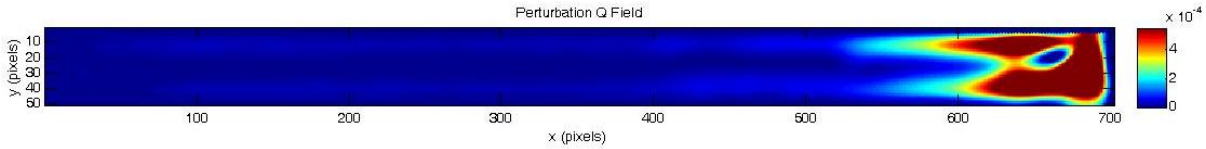

(d)

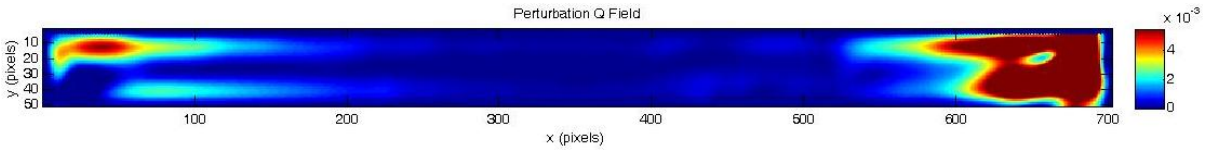

(e)

Figure 4.14. Perturbation Q field at B_{max}= (a) 100G , (b) 300G (c) 500G (d) 700G, and (e) 900G in anti-parallel configuration in a magnetic fluid.

4.5 Rayleigh number, Grashof number and Prandtl number in a magnetic fluid

Rayleigh number (Ra) is a dimensionless number in natural convection. When Ra is below a critical value for that fluid, thermal conduction is the main heat transfer mechanism; when Ra exceeds the critical value, heat transfer is primarily in the form of thermal convection. It is represented by equation [3]

$$Ra = \frac{C_p \rho^2 g \beta \Delta T l^3}{\eta k} \tag{4.13}$$

where C_p is heat capacity (1.84×10^3 J/kg K), ρ is density of the fluid (0.87×10^3 kg/m^3), g is standard gravity (9.8 m/s^2), β is thermal expansion coefficient (0.85×10^{-3} K^{-1}), ΔT is the temperature difference across the sample cell, l is the length of the cell, and η is dynamic viscosity (8.5×10^{-3} kg/m s), and k is thermal conductivity (0.15 W/m.K).

Magnetic Rayleigh number (Ra_m) is a dimensionless number in thermomagnetic convection, it is defined as [3]

$$Ra_m = \frac{C_p \rho \mu_o K \Delta T \Delta H l^2}{\eta k} \tag{4.14}$$

where μ_o is vacuum permeability ($4\pi \times 10^{-7}$ N/A^2), K is Pyromagnetic coefficient (50 A/m K). The viscosity in diluted magnetic fluid is increased in applied field with shear flow. In our experiment, the field and vorticity are perpendicular. The viscosity change as a function of field can be presented by [3 and 64].

$$\Delta\eta = \frac{3}{2}\eta_o \phi \frac{\alpha - \tanh\alpha}{\alpha + \tanh\alpha} \tag{4.15}$$

Where η_o is the viscosity of carrier fluid, ϕ is volume fraction of the magnetic fluid. α=mB/kT is the ratio of the magnetic energy to thermal energy, with m the magnetic moment

of the particle and B the internal field, and T the local temperature. The volume fraction in our magnetic fluid is 1%, so the ratio of viscosity change $\Delta\eta\ /\eta o$ is less than 1.5%, which is not important in our system. The thermal and magnetic Rayleigh numbers in our experiment are show in table 4.2 and figure 4.15.

Table 4.2. Thermal and magnetic Rayleigh numbers in a magnetic fluid in magnetic fields in two configurations.

$Ra_m(10^7)$ Parallel configuration	$Ra(10^7)$ Parallel configuration	Field(G)	$Ra(10^7)$ Anti-parallel configuration	$Ra_m(10^7)$ Anti-parallel configuration
0	16.1	0	16.1	0
4.3	15.0	100	17.5	5.0
8.2	14.2	200	18.9	10.9
11.5	13.4	300	20.1	17.2
14.7	12.8	400	20.9	24.0
17.8	12.4	500	21.6	30.9
20.5	12.0	600	22.2	38.2
23.7	11.9	700	22.8	45.8
26.9	11.7	800	23.2	53.5
29.5	11.4	900	23.6	61.3
32.7	11.4	1000	24.0	69.2

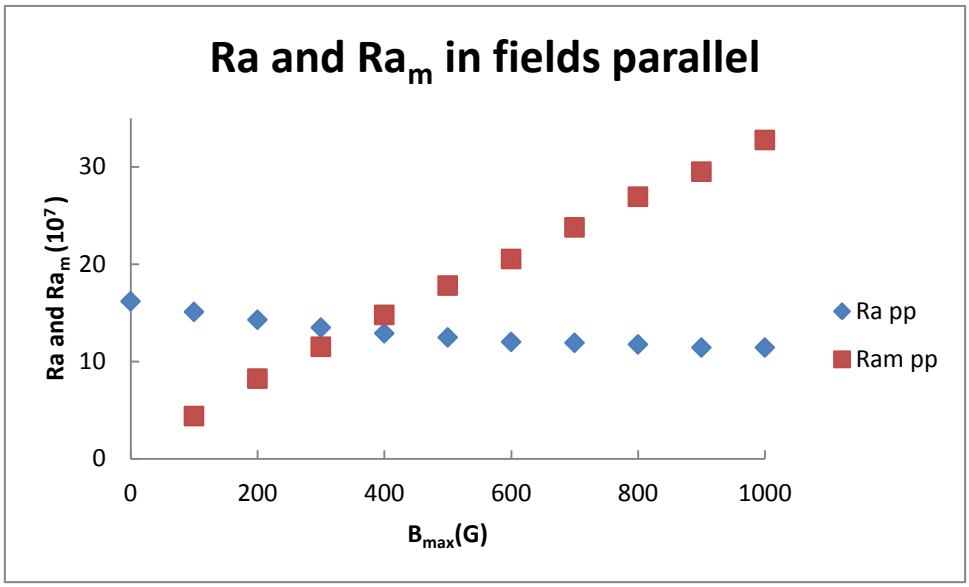

(a)

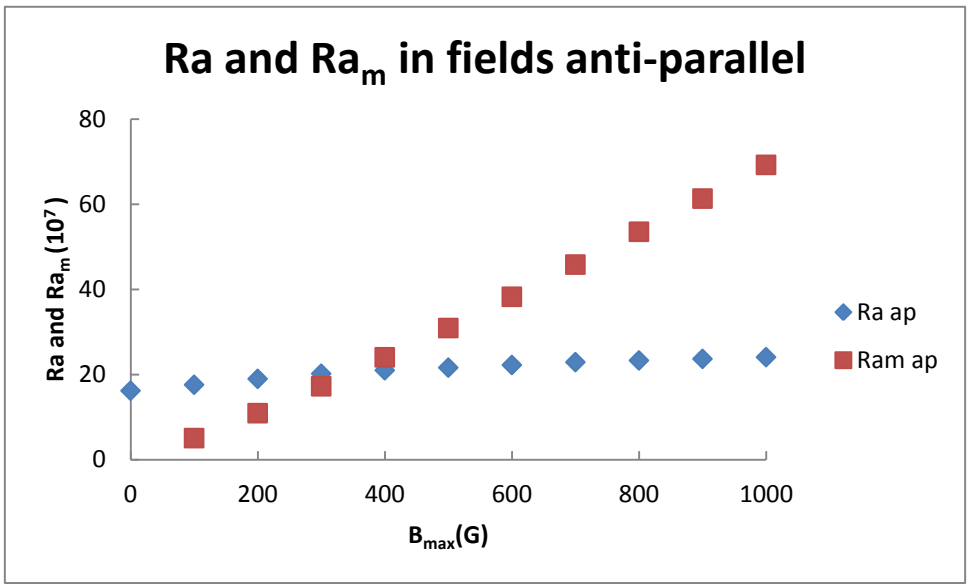

(b)

Figure 4.15 Ra and Ra_m in field in (a) parallel, (b) anti-parallel configuration

From table 4.2 and figure 4.15, first, the Ra is much larger than critical Ra number (1700), so the convection is primary heat transfer mechanism as we discussed in chapter 4.1. Ra decreases in parallel configuration and increases in anti-parallel configuration due to temperature difference change. When applied magnetic fields $B_{max} \leq 300G$, Ra is larger than Ra_m, thermal convection is still main mechanism. When $B_{max} \geq 400G$, Ra_m is larger than Ra, that means the thermomagnetic convection dominates in these applied fields. Ra_m increases with increased fields in both configuration, but it is larger in anti-parallel configuration which means the magnetic body force is larger in anti-parallel configuration, that is consistent with the calculation of the body force in chapter 4.6.

Prandtl number (Pr) is a dimensionless number to define the ratio of kinematic diffusivity to thermal diffusivity. Prandtl number is given as:

$$Pr = \frac{\eta}{\rho D} \tag{4.16}$$

where thermal diffusivity D is $3.7*10^{-8}$ m^2/s. Pr = 264.1 in our experiment.

The Grashof number (Gr=Ra/Pr) is a dimensionless number in fluid mechanics. Gr is defined as the ratio between buoyancy forces and viscous forces. Magnetic Grashof number ($Gr_m=Ra_m/Pr$) is the ration between the magnetic force and viscous force. The thermal and magnetic Grashof numbers is our system are showed in table 4.3 and figure 4.16.

The result from Grashof numbers is basically the same with Rayleigh number.

Table 4.3. Thermal and magnetic Grashof numbers in a magnetic fluid in magnetic fields in two configurations.

$Gr_m(10^5)$ Parallel configuration	$Gr(10^5)$ Parallel configuration	Field(G)	$Gr(10^5)$ Anti-parallel configuration	$Gr_m(10^5)$ Anti-parallel configuration
0	6.1	0	6.1	0
1.6	5.7	100	6.6	1.9
3.1	5.4	200	7.1	4.1
4.3	5.1	300	7.6	6.5
5.5	4.8	400	7.9	9.1
6.7	4.7	500	8.1	11.7
7.7	4.5	600	8.4	14.4
9.0	4.5	700	8.6	17.3
10.1	4.4	800	8.8	20.2
11.1	4.3	900	8.9	23.2
12.4	4.3	1000	9.1	26.2

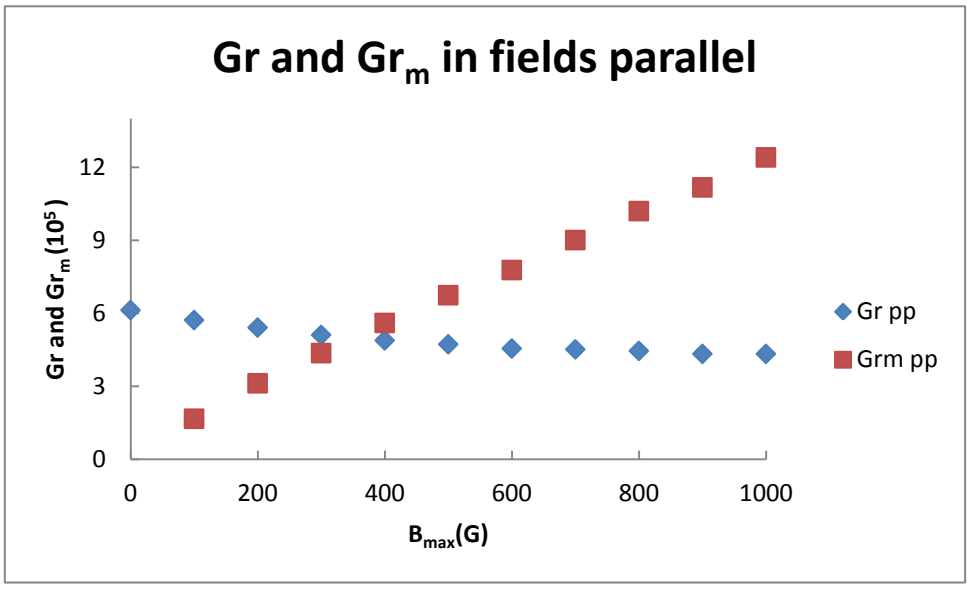

(a)

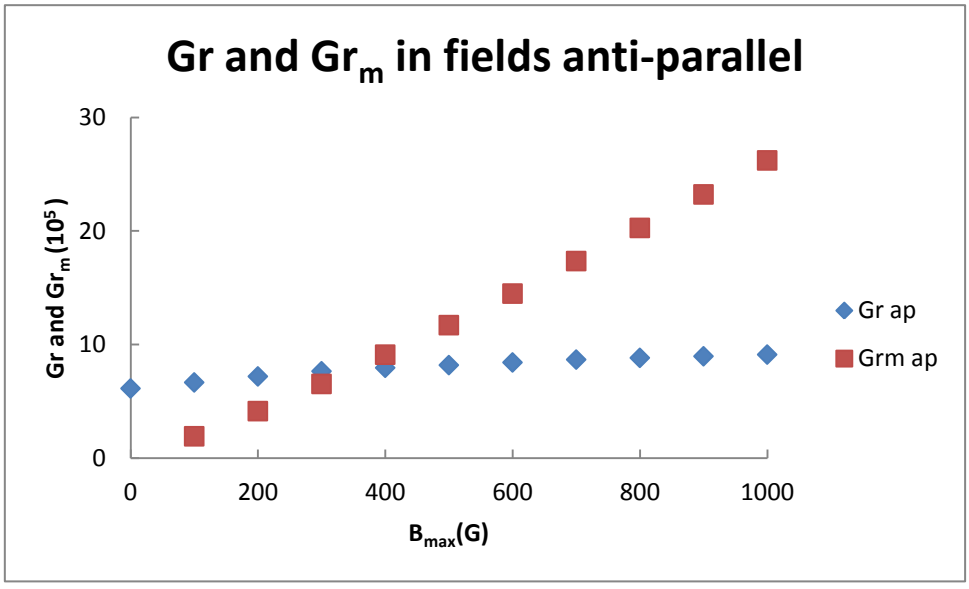

(b)

Figure 4.16. Gr and Gr_m in field in (a) parallel, (b) anti-parallel configuration

4.6 Calculation of magnetic susceptibility and body force in a magnetic fluid

The magnetic fluid experiences a magnetic body force in the magnetic field. The body force will affect the thermal transfer in the magnetic fluid [13 and 64]. The magnetic body force is calculated in our samples to see how the magnetic body force changes with different fields and field gradients, and how the force affects the convection in fluids.

The magnetic particles in the magnetic fluid are ferromagnetic which are magnetized in relatively small magnetic fields. When there is no field, the direction of the magnetic moments of particles is not ordered. The elementary magnetic moments align with applied external magnetic field. First, we calculate the magnetic energy and thermal energy ratio to see how the particles align in fields. Magnetic energy is E_m = mB, and thermal energy is kT, where m is magnetic moment of each magnetic particle, m = 2.1×10^4 μ_B = 1.95×10^{-19} J/T, B is local magnetic field. k is Boltzmann constant, k = 1.38×10^{-23} J/K and T is the absolute temperature. Figure 4.17 shows the magnetic energy and thermal energy ratio in field in two sample cells. From this plot, the magnetic energy is larger than thermal energy, so the magnetic fluid in fields is ferromagnetic, the Langevin equation is applied to calculate magnetization in our system.

Then the thermal energy and magnetic dipole interaction energy is calculated to check cluster formation in the magnetic fluid in fields. The magnetic dipole interaction energy is presented as:

$$E_i = -\frac{\mu_0}{4\pi r^3}(3(\boldsymbol{m_1}\cdot\hat{\boldsymbol{r}})(\boldsymbol{m_2}\cdot\hat{\boldsymbol{r}}) - \boldsymbol{m_1}\cdot\boldsymbol{m_2} \quad (4.17)$$

Where μ_o is vacuum permeability ($4\pi \times 10^{-7}$ N/A^2), r is the distance between the centers of two particles, $\hat{\boldsymbol{r}}$ is a unit vector that join the center of two particles. Here we consider the magnetic interaction energy when two particles in contact and align in the same direction, equation 4.17 become $E_i = -\frac{\mu_0}{4\pi d^3} 2m^2 = 7.6 \times 10^{-21}$ J. d is the diameter of the particles. The thermal energy kT is 4.04×10^{-21} J at room temperature (293 K). The interaction parameter λ =0.94 is the ratio between $E_i$and $2kT$ [65]. If the surfactant layer thickness δ is taken into account, a modification of the interaction parameter $\lambda^* = \lambda d^3/(d+2\delta)^3 = 0.34$. An effective chain formation occurs if $\lambda^* \gg 1$ [65], so in our system, there is no effective chain formation.

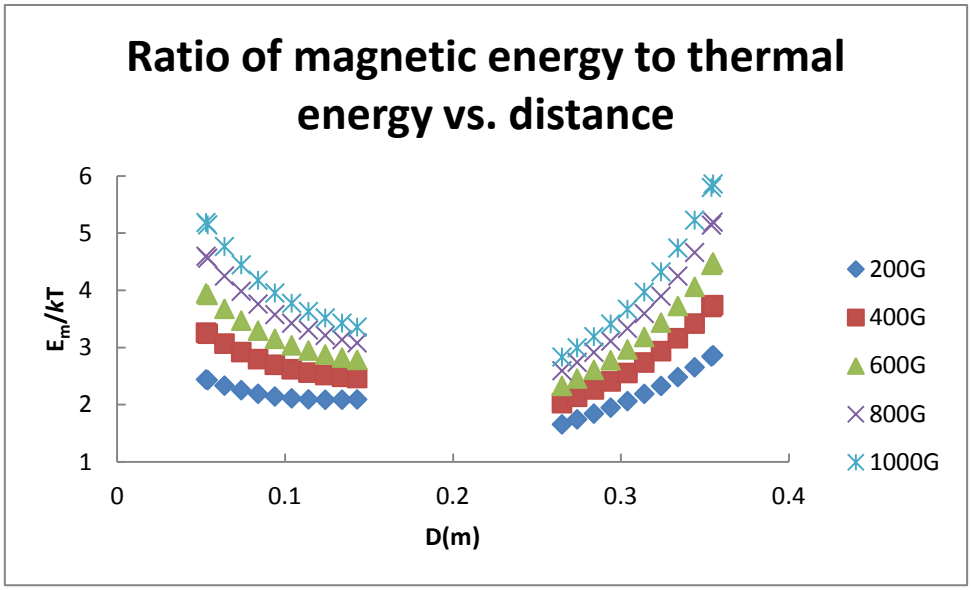

Figure 4.17. Ratio of magnetic energy to thermal energy in fields in our magnetic fluid.

To calculate the body force, the magnetization of the magnetic fluid need to be find first. The magnetizationin fields is described by the Langevin function (Langevin, 1905).

$$M = M_s\, L(\alpha) \tag{4.18}$$

$M_s = \phi M_o$ is saturation magnetization of the fluid. It is determined by the spontaneous magnetization M_o and the volume fraction ϕ of the magnetic particles. The real magnetization curve of a magnetic fluid may differ from Langevin curve [24]. The difference is due to the polydispersity of particles in the real fluid and local field effect of particles in concentrated fluids. The non-spherical particles may also have an effect on it.

The magnetic fluid has a Curie point. Curie temperature T_c is the critical point where the ferromagnetic turns into a paramagnetic. Above Curie temperature, it is paramagnetic, and ferromagnetic below T_c. The magnetic susceptibility changes with temperature from Curie-Weiss law $\chi = C/(T-T_c)$, C is the curie constant of the magnetite. The Curie temperature for the different magnetic materials varies within a wide range [24]. In our experiment, the magnetic particle is Fe_3O_4, the curie temperature Fe_3O_4 of is 850K [66], which is much higher than our experimental temperature (265-320K).

The magnetic body force per unit volume is

$$f_m = \mu_o(\boldsymbol{M} \cdot \nabla)\boldsymbol{H} \tag{4.19}$$

From previous study [67], in the experiment, the body force can be written

$$f_m(x) = \mu_o\ M(T(x))\frac{\partial H}{\partial x} \tag{4.20}$$

The external magnetic field only changes along the x axis in our sample cells. Since

the cells are quasi-one dimensional and the magnetic field H is continuous along the y axis. The intern field H is equal to the external field H_o as shown in figure 4.18.

From Langevin classical theory of paramagnetism [3, 64], the magnetization

$$L(\alpha) = \coth \alpha - 1/\alpha = \frac{e^{\alpha} + e^{-\alpha}}{e^{\alpha} - e^{-\alpha}} - \frac{1}{\alpha} \quad (4.21)$$

$$\alpha = m\ \mu_{o(}\ H+M)\ /kT \quad (4.22)$$

where m is magnetic moment of each magnetic particle , $m = 2.1 \times 10^4\ \mu_B = 1.95 \times 10^{-19}$ J/T, k is Boltzmann constant, $k = 1.38 \times 10^{-23}$ J/K and T is the absolute temperature. The magnetic susceptibility χ is defined as:

$$\chi = \frac{dM}{dH} \quad (4.23)$$

$$H_o = B_o / \mu_o \quad (4.24)$$

For the magnetic fluid with 1% concentration, saturated magnetization M_s = 55G = 4.38×10^3 A/m (1 A/m = $4\pi \times 10^{-3}$ G)

If we want to calculate the body force, local field H, local temperature T and local susceptibility χ are needed, which all depends on distance x to the pole. We can find the function of H(x) and T(x) by using polynomial fitting of the experimental data at a steady state. We plot the magnetization distribution, susceptibility and body force along the sample cells in different fields in figure 4.19.

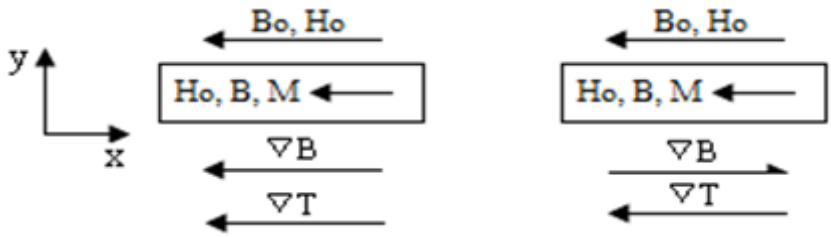

Figure 4.18. Internal fields in sample cell.

Here we only plot the magnetic body force in B_{max} = 200,400,600,800 and 1000 G. The graphs in other fields are similar with these figures. Also the temperature distributions on the top of sample cells are used in calculation. If we use the temperature distributions in the middle or on the bottom of sample cells, we get basically the same results.

From figures 4.19, the body forces have the opposite directions in two sample cells which depend on the relative directions of field gradient. The magnitude of the body force is determined by local magnetization, field gradient and temperature. Larger magnetization and field gradient cause larger body force. And the body force is bigger at low temperature. The force is increased with increasing field. In parallel configuration, the direction of the force is same with the temperature gradient. Therefore, the body force increases the convective thermal transfer in the magnetic fluids. While the body force direction is opposite from the temperature gradient in anti-parallel configuration, the body force suppress the convective thermal transfer by changing the flow pattern. The body force calculation confirms the previous prediction. [68]

The analysis of flow patterns for non-step field procedure is ongoing, and it is not included in this dissertation.

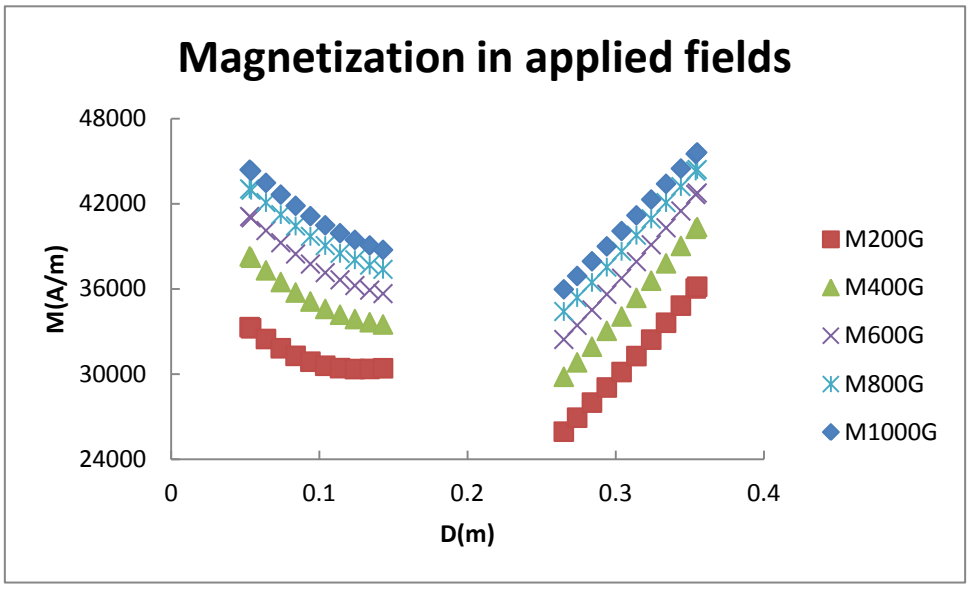
Magnetization in applied fields
48000
42000
36000
30000
24000
M(A/m)
0
0.1
0.2
0.3
0.4
D(m)
M200G
M400G
M600G
M800G
M1000G

(a)

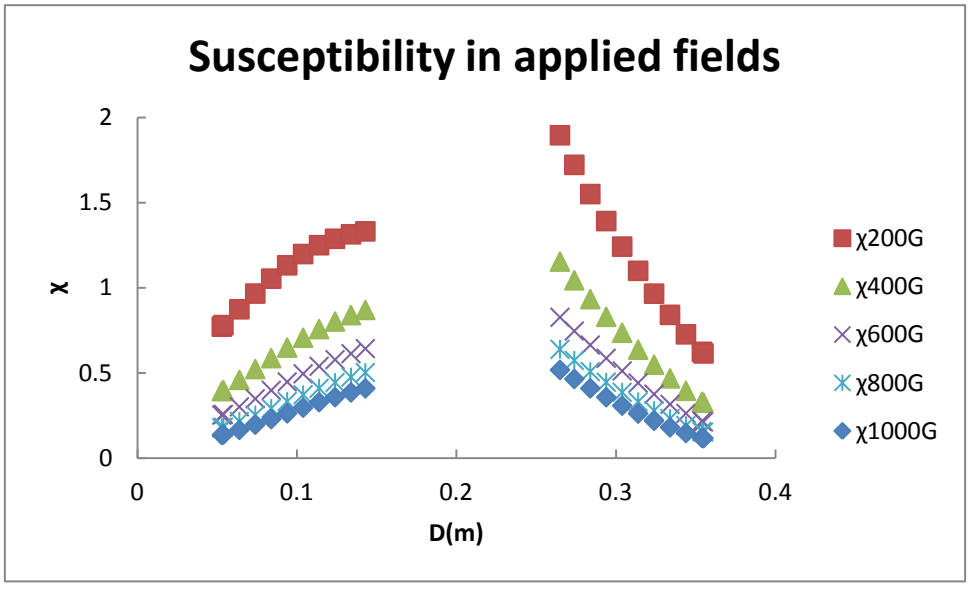
Susceptibility in applied fields
2
1.5
1
0.5
0
χ
0
0.1
0.2
0.3
0.4
D(m)
χ200G
χ400G
χ600G
χ800G
χ1000G

(b)

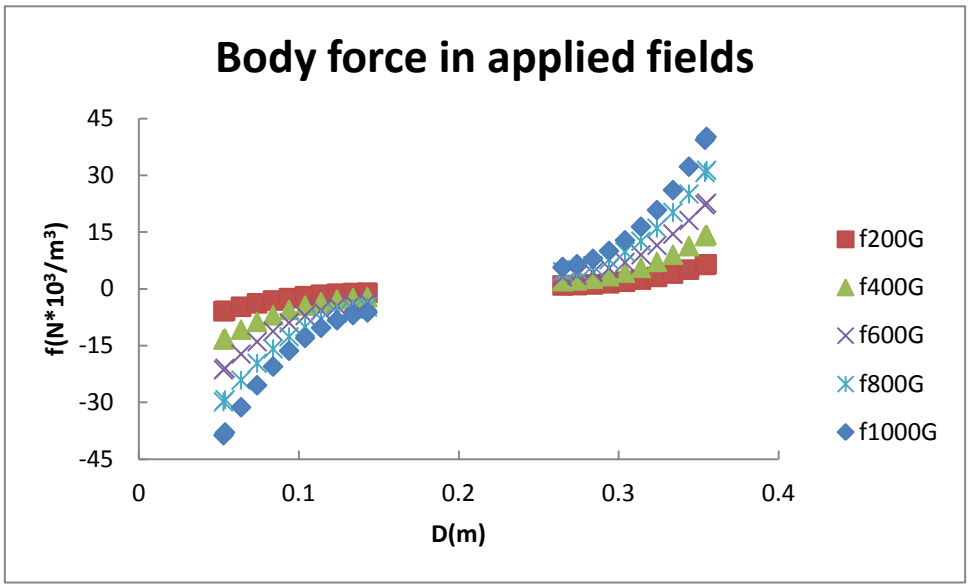

(c)

Figure 4.19. (a) magnetization, (b) susceptibility, and (c) magnetic body force in a magnetic fluid in applied fields.

CHAPTER 5: CONCLUSIONS

Convective heat transfer driven by the buoyancy force and the magnetic body force in a magnetic fluid with horizontal temperature and field gradients was studied experimentally. From our analyses, it was found that convection is the primary heat transfer mechanism in our system. When the magnetic fields are applied, there are two regimes for convection: 1) ordinary thermal convection which is driven by buoyancy force and 2) thermomagnetic convection that is driven by magnetic body force. We found when the fields less than a certain value ($B_{max} \leq 300G$ where B_{max} is field at the magnet pole), Rayleigh number (Grashof number) is larger than magnetic Rayleigh number (magnetic Grashof number), the thermal convection is main convection mechanism; while in high field regime ($B_{max} \geq 400G$), magnetic Rayleigh number (magnetic Grashof number) becomes larger than Rayleigh number (Grashof number) indicating thermomagentic convection is dominated.

By using three different methods, we imaged the convective flow velocity fields and streamlines to show flow patterns. The flow pattern changes when thermal convection changes to thermomagentic convection. In parallel configuration, the streamlines indicate the convective motion may crossover from two-dimensional to three-dimensional flow, the crossover effect is stronger in higher field. For anti-parallel configuration, the local flow structures formation happens, the convection likely changes from one convection roll to multiple rolls.

The magnetic body force enhances or inhibits the convective thermal transfer in the

magnetic fluids which depends on the relative directions of temperature gradient and field gradient. We will do more study on Q field and multiple dipoles interaction in the future.

The results obtained in this dissertation work confirm previous application proposed from our group. It also suggests that the magnetic fluid can be used as non-intrusive field control device to increase or decrease heat transfer.

LIST OF REFERENCES

[1] G.K. Batchelor, An introduction to fluid dynamics, Cambridge University Press, 1967.

[2] Adrian Bejan, Heat transfer, by John Wiley & Sons, Inc. 1993

[3] R.E.ROSENSWEIG, Ferrohydrodynamics, Cambridge University Press, 1985

[4] V.E.Fertman, Magnetic Fluids guidebook: properties and applications, Hemisphere Publishing Corporation, 1990

[5] H. Yamaguchi, I. Kobori, Y. Uehata, K. Shimada, J. Magn. Magn. Mater. 201 (1999) 264.

[6] H. Yamaguchi, I. Kobori, Y. Uehata, J. Thermophys. Heat Transfer 13 (1999) 501.

[7] C.Y.Wen, W.-P. Shu, J. Magn. Magn. Mater. 252C (2002) 206.

[8] C.Y.Wen, W.-P. Shu, J. Magn. Magn. Mater. 289 (2005) 299.

[9] M.S.Krakov, I.V. Nikiforov, J. Magn. Magn. Mater. 252 (2002) 209.

[10] M.S.Krakov, I.V. Nikiforov, A.G. Reks, J. Magn. Magn. Mater. 289 (2005) 272.

[11] H. Yamaguchia, X. Niua, X. Zhang and K. Yoshikawaa, J. Magn. Magn. Mater. 321(2009) 3665-3670

[12] L. Schwab, U. Hildebrandt, and K. Stierstadt, J. Magn. Magn. Mater. 39,113 1983.

[13] B.A. Finlayson, J. Fluid Mech. 40 (1970) 753

[14] V. G. Bashtovoi, Thermomechanics of Magnetic Fluid: Theory and Application, ed. B. Berkovsky, Hemisphere, 1978

[15] V. G. Bashtovoy, B. M. Berkovsky and A. N. Vislovich, Introduction to Thermomechanics of Magnetic Fluids, Hemisphere, 1988

[16] E. Blums, Yu. A. Mikhailov, R. Ozols. Heat and Mass Transfer in MHD Flows, World Scientific, Singapore, 1987, 512 p.

[17] Berkovsky B and Bashtovoy V, 1996 Magnetic Fluids and Applications Handbook , New York: Begell House

[18] F. Khaldi, J. Noudem, and P. Gillon, Int. J. Heat Mass Transfer, Volume 48, Issue 7, Pages 1350–1360, 2005

[19] S. A. Suslov, A. A. Bozhko, A. S. Sidorov, and G. F. Putin, Phys. Rev. E, Vol. 86, 2012;

[20] A. A. Bozhko, G. F. Putin, E. N. Beresneva, and P. V. Bulychev, Z.Phys. Chem. Vol. 220, PP 251, 2006;

[21] S. Wakitani, J. Fluid Mech. Vol. 314, Pp 299, 1996

[22] D. Braithwaite, E. Beaugnon & R. Tournier, Nature 354, 134 – 136, Nov. 1991

[23] Stefan Odenbach, magnetoviscous effects in Ferrofluids, springer, 2002

[24] B. M. Berkovsky, V. F. Medvedev, M.S Krakov. Magnetic Fluids Engineering Applications, Oxford University Press, 1993

[25] R Kaiser, Method of separating materials of different density, US Patent 3483968, 1969

[26] Ch. Alexiou, R. Schmid, R. Jurgons, Ch. Bergemann, W. Arnold and F.G. Parak, Ferrofluids: Magnetically Controllable Fluids and Their Applications. Edited by S. Odenbach, p.233-251, Spring, 2002

[27] M.I. Papisov, A. Bogdanov Jr., B. Schaffer, N. Nossif, T. Shen, R. Weissleder and T.J. Brady J. Magn. Magn. Mater. 122 (1993), pp. 383–386.

[28] T. Kuwahara, F. De Vuyst, and H. Yamaguchi, Phys. Fluids 21, 097101 (2009)

[29] T. Kuwahara and H. Yamaguchi, J. Thermophysics and Heat Transfer, Vol. 21, No. 1, PP. 173-180. 2007

[30] Z. Ming, L. Zhongliang, M. Guoyuan, C. Shuiyuan, Exp. Therm. Fluid Sci., 33 (7) (2009), pp. 1100–1105

[31] B. Jeyadevan, H. Koganezawa, K. Nakatsuka, J. Magn. Magn. Mater., 289 (2005), pp. 253–256

[32] B. M. Berkovskii, V. G. Bashtovoi , Unesco, Magnetic Fluids and Applications Handbook, Begell House Publishers, 1996

[33] J. A. Barclay, J. Appl. Phys. 53, No. 4, 2887-2894, 1982

[34 R. Hunt and G. Wilks, Numerical Heat Transf. Volume 4, Issue 3, pp. 303-316 1981

[35] R. Touihri, H.B. Hadid and D. Henry, Phys. Fluids 11, 2078 (1999)

[36] K. Raj and R. Moskowitz, Ferrofluid-cooled electromagnetic device and improved cooling method, US Patent number: 5462685, 1995.

[37] S. Odenbach, J. Magn. Magn. Mater. 149, 155 (1995);

[38] A. Mukhopadhyay, R. Ganguly, S. Sen, and I. K. Puri, Int. J. Heat Mass Transfer 48, 3485 (2005) ;

[39] A. A. Bozhko and G. F. Putin, Microgravity Sci. Technol. 21, 89 (2007).

[40] S. Odenbach, Adv. Space Res. Vol.13, No.7 PP105-107,1993

[41] Omega K type thermocouples, http://www.omega.com/Temperature/pdf/IRCO-BW.pdf

[42] Keithly 2701, http://www.keithley.com/products/data/datalogger/?mn=2701

[43] Minco heater HK5572, http://www.minco.com/ uploadedFiles/Product s/Thermofoil_Heaters/Kapton_Heaters/hs202b-hk.pdf

[44] Polyscience digital controller 9102, http://www.polyscience.com/lab/9100.html

[45] T. Liu and J.P. Sullivan, Pressure and Temperature Sensitive Paints, Spring 2005

[46] Figliola, R.S. and D.E. Beasley, Theory and design for mechanical measurements. 5th edition ed. 2011.

[47] Antonio Galbis and Manuel Maestre, Vector Analysis Versus Vector Calculus. Springer. 2012

[48] P. Kundu, I.Cohen, and D. Dowling, Fluid mechanics, 5th edition, 2012

[49] T. Liu and L Shen, J. Fluid Mech. (2008), vol. 614, pp. 253-291

[50] Private communication with Dr. Tianshu Liu

[51] M. Krichler and S.Odenbach, Journal of Magnetism and Magnetic Materials 326 (2013) 85–90

[52] H.D.Baehr, K.Stephan, Heat and mass transfer, Springer, Heidelberg, 2010.

[53] T. Voelkera and S. Odenbach, PHYSICS OF FLUIDS, Vol. **17**, 037104 (2005)

[54] Ludwig C 1856 *S-B. Akad. Wiss. Wien* **20** 539

[55] Soret C 1879 *Arch. Sci. Phys. Nat. Gen`eve* [3] **2** 48

[56] de Groot S R 1945 *L'effet Soret* (Amsterdam: NV Noord-Hollandsche Uitgevers Maatschappij)

[57] V.A.F. Costa, A time scale-based analysis of the laminar convective phenomena, International Journal of Thermal Sciences 41 (2002) 1131–1140

[58] M.I. Shliomis, M. Souhar, Self-oscillatory convection caused by the Soret effect, Europhys. Lett., 49 (2000), p. 55

[59] Yuchou Hu, Robert E. Ecke, and Guenter Ahlers, Time and Length Scales in Rotating Rayleigh-Bénard Convection, Phys. Rev. Lett. **74**, 5040 (1995)

[60] J.C. Bacri, A. Cebers, A. Bourdon, G. Demouchy, B. M. Heegaard, and R. Perzynski, Forced Rayleigh Experiment in a Magnetic Fluid, Phys. Rev. Lett. **74**, 5032 ~1995.

[61] T. Du and W. Luo, Nonlinear optical effects in ferrofluids induced by temperature and concentration cross coupling, Appl. Phys. Lett. **72**, 272 (1998)

[62] E Blums, S Odenbach, A Mezulis, M Maiorov, Physics of Fluids, Volume 10, Issue 9, pp. 2155-2163 (1998)

[63] J.C.R. Hunt, A.A. Wray, and P. Moin, Center for Turbulence Research, Proceedings of the Summer Program 1988

[64] M I Shliomis 1974 Sov. Phys. Usp. 17 153

[65] S Odenbach, J. Phys. Condens. Matter 16 (2004)

[66] B. Lee, "Magnetite (Fe3O4): Properties, Synthesis, and Applications" (2007).Vol.15, 2007. Paper 5.

[67] W. Luo, T. Du, and J. Huang, Phys. Rev. Lett. 82, 4134-4137 (1999)

[68] W. Luo, Apparatus and methods of transferring heat with a differential magneto-thermal

force, US8082740 B2, 2006